Experimental and Numerical Determination of Thermohydraulic Properties of Regenerators Subjected to Oscillating Flow

by

Sandro Schopfer
Dipl.Ing. FH, Zurich University of Applied Sciences, 2007

A Dissertation Submitted in Partial Fulfillment of the
Requirements for the Degree of

MASTER OF APPLIED SCIENCE

in the Department of Mechanical Engineering

Experimental and Numerical Determination of Thermohydraulic Properties of Regenerators Subjected to Oscillating Flow

by

Sandro Schopfer
Dipl.Ing. FH, Zurich University of Applied Sciences, 2007

Supervisory Committee

Dr. A. Rowe, Supervisor
(Department of Mechanical Engineering)

Dr. H. Struchtrup, Departmental Member
(Department of Mechanical Engineering)

Dr. P. Oshkai, Departmental Member
(Department of Mechanical Engineering)

Supervisory Committee

Dr. A. Rowe, Supervisor
(Department of Mechanical Engineering)

Dr. H. Struchtrup, Departmental Member
(Department of Mechanical Engineering)

Dr. P. Oshkai, Departmental Member
(Department of Mechanical Engineering)

ABSTRACT

Regenerators are key components in many thermal devices such as Stirling cryocoolers, magnetic refrigeration devices etc. They act as temporal thermal energy storage and therewith separate two thermal reservoirs. Regenerators are typically made up of porous structures referred to as the packing material that can lead to complex flow pathways of the heat transfer fluid through the regenerator. The nonisothermal and periodically reversing flow type allows for thermal energy exchange with the packing material of the regenerator. The performance of such devices depends greatly on the geometry of the porous structure, its material properties, length scales involved as well as operating conditions.

This thesis is a study of thermohydraulic properties of thermal regenerators under oscillating flow conditions. In the first part of this thesis, thermodynamic models are developed for the extraction of the friction factor and Nusselt number from an experiment based on a harmonic approximation technique. These models are verified using a two dimensional pore scale model that allows to calculate friction factor and Nusselt number on a theoretical basis independent from an experiment. The second part of this thesis is devoted to the application of the models presented in part one to an experiment. A test apparatus that allows to measure temperature

and pressure drop for various types of regenerators is presented. The measurements for a microchannel and packed bed of spheres regenerator are characterized using spectral analysis. Friction factor and Nusselt numbers are evaluated and parametrized using the models derived in the first part of this thesis.

The methodology presented in this thesis reveals insights in the dynamic effects of oscillating flow type heat transfer. The theoretical findings are applied to experimentally obtained data for a correct interpretation of friction factor and Nusselt number.

Contents

List of Tables

List of Figures

ACKNOWLEDGEMENTS

During my time in Victoria I had the chance to become friends with many interesting people. I would like to thank everybody that supported me and introduced me to many beautiful activities the west coast has to offer. I will never forget the time we shared in the water, on boats and hiking mountains on the west coast.

My supervisor Andrew Rowe deserves special acknowledgement. He had always an open ear for my sometimes exotic ideas and gave me the intellectual space to develop them. His patience and immense knowledge of experimental and theoretical principles helped me to focus on the essentials.
This work would have never been possible without the help of the infamous Cryofuels Laboratory. Armando Tura's engineering expertise is the foundation of the experimental part of this work. I would like to thank him for his help, friendship and for keeping the euro-spirit alive. Also Danny Arnold's experimental help has saved me immense amount of hours which has been credited in form of coffee breaks and discussions with him and the rest of the Cryo-Gang.

Finally I would like to thank my family for their support and love at any time.

Chapter 1

Introduction

1.1 Thermal Regenerators

A regenerator is often viewed as a regenerative heat exchanger. In an ordinary heat exchanger, the two fluids exchanging energy are separated by a solid surface. In a regenerator, the same space is occupied alternately by the hot fluid and the cold fluid while the energy to be transferred is stored and released from the regenerator packing material (matrix). The hot and cold fluid only differ in temperature and pass in periodical operation through the regenerator matrix. As the hot fluid passes through the permeable regenerator matrix thermal energy is stored in the solid material. This sequence of operation is referred to as the *hot blow* or *hot period*. During the *cold blow* or *cold period* the flow is reversed and the stored energy is recovered by the cold fluid (entering from a cold reservoir) and rejected to the hot space [1].

An example of a regenerator can be found in the human body: We use our nose and throat as a regenerative heat exchanger when we breathe. The cooler air coming in is warmed, so that it reaches the lungs as warm air. On the way back out, this warmed air deposits much of its heat back onto the sides of the nasal passages, so that these passages are then ready to warm the next batch of air coming in. The first technical application that made use of regenerators might be the Stirling engine. In a two cylinder type Stirling engine the two cylinders are connected using a regenerator. The regenerator periodically stores the energy that is displaced from either the hot or the cold cylinder. Without the regenerator the stored amount of

thermal energy would be irreversibly rejected to the environment and thus lowering the efficiency of the device significantly. In this sense the regenerator acts to maintain the temperature span between the two cylinders.

The active magnetic regenerative refrigerator (AMRR) is another device that makes use of the standard principle of a regenerator such as in the Stirling engine. In AMRR the regenerator is made of active magnetic material (predominately rare earth elements, alloys and compounds) which exploits the magnetocaloric effect (MCE). The MCE, as it is used in this context, is the property exhibited by this material of reversibly changing its temperature when the material is adiabatically exposed to a magnetic field change. By using such a material in a regenerator as the thermal energy storage medium and as the means of work input (change in magnetic field), one creates an active magnetic regenerator (AMR). Upon alternating fluid flow and magnetic field a temperature gradient is established throughout the regenerator that separates hot and cold end of the regenerator. A thermal load can be applied on the cold end that represents the cooling power to refrigerate a cold space.

The research and results that are presented in this work are mainly used for the design of new potential regenerator geometries to be used in AMRR prototypes [2]. However, because of the broad application range of regenerators in thermal devices, the methodology and results can be adapted to similar devices with similar operating conditions.

1.2 Thermohydraulic Optimization of Regenerators

Multiple transport processes take place in an AMR. Among the most basic ones is the transport of momentum and thermal energy. Thus the thermohydraulic optimization of an AMR can be done in a passive environment (i.e. in the absence of any magnetic field). The properties of a well designed passive regenerator are [3]

1. High heat transfer (product of interfacial heat transfer coefficient times interfacial area). Favourable geometries are packed beds, parallel channels, rectangular channels or perforated plates. The mean flow direction is referred to as axial direction while the radial ordinate represents the direction perpendicular to the flow as shown in figure (1.1).

2. Large thermal mass of the regenerator material compared to the heat transfer

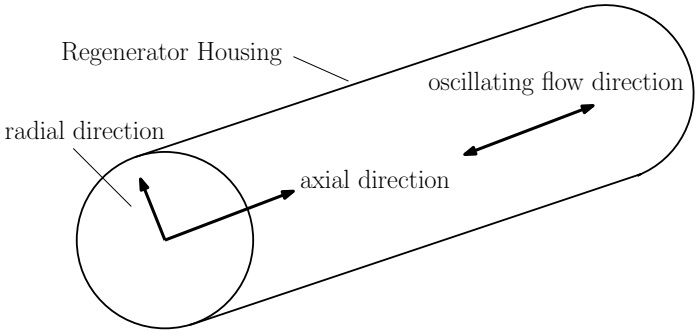

Figure 1.1: Visualization of axial and radial direction

fluid.

3. small axial thermal conduction in both regenerator and heat transfer fluid. In contrast, the radial conductivity should be high to maintain internal equilibrium. These two properties can only be guaranteed by a choice of a proper geometry (i.e. the geometry should introduce more thermal resistance in the axial than in the radial direction).

4. Low pressure drop to minimize irreversible pumping losses.

5. Low dead volume associated with the porous structure of the regenerator. Actual void to total volume ratio ranges between 0.3 and 0.7. In an AMR, the fluid in the void spaces acts as a parasitic load, decreasing the useful magnetocaloric effect.

Many of these characteristics are typically opposing each other, for example large heat transfer area, and small dead volume result in high pressure drops across the regenerator. Thus this optimization problem is not trivial and has been a challenge to many thermal engineers in the past. For this reason, passive regenerator testing and modelling is a research topic with a long history. One of the primary goals in this field is to determine friction factor and interfacial heat transfer coefficient of the regenerator matrix.

So far, it has proven difficult to generalize results. The actual performance depends on a large parameter space resulting in large scattering in the heat transfer coefficient. As a result, it becomes essential to characterize a regenerator geometry within the aspect ratios and operating conditions needed for a particular device.

For this reason a passive regenerator test apparatus (PRTA) has been developed to gain further understanding of the thermal and hydraulic properties of a

certain regenerator geometry. The outcome of an experiment using this apparatus is typically a correlation for the heat transfer coefficient (or Nusselt number) and the friction factor as a function of operating condition and regenerator design. The Nusselt number describes the ratio between convective and conductive heat transfer that occurs under stagnant conditions. The friction factor represents the non-dimensional pressure drop through the regenerator.

The use of these correlations is twofold. The correlations are used to determine the amount of energy dissipation that a certain regenerator geometry involves. Based on this criteria (and other non thermohydraulic properties), a regenerator can be used in a prototype that shows optimal heat transfer to pressure drop ratio. In addition, the correlations can be used for high level models that predict gross power output and temperature span in an actual device. The Nusselt number is of particular interest as the performance of many regenerative devices is very sensitive to this parameter. As result, model predictions are greatly improved by having accurate information regarding the heat transfer of a given regenerator matrix.

1.3 Passive Regenerator Testing

Passive testing involves characterization of regenerator geometries in absence of a magnetic field. As a result, the regenerators for passive testing can be made of a metal that has much better availability at lower prices but has similar properties (i.e. density, heat capacity, thermal conductivity) compared to an active magnetic material.

Passive regenerator testing can involve multiple steps as shown in figure (1.2). At first there is an initial idea of a potential geometry. This originates from either experience or initial model predictions. Once test data has been collected, the data is analyzed and useful information like Nusselt number is extracted. The plausibility of the results is validated with independent simulations. After some iterations the geometry can be compared to previously tested structures. In this way, preferred geometries can be fabricated using active magnetic materials and thus allows for testing in AMRR prototypes. However, it must be pointed out that a well performing passive geometry might be infeasible for active magnetic use, because it enhances magnetic losses, like strong demagnetizing effects or eddy current dissipation.

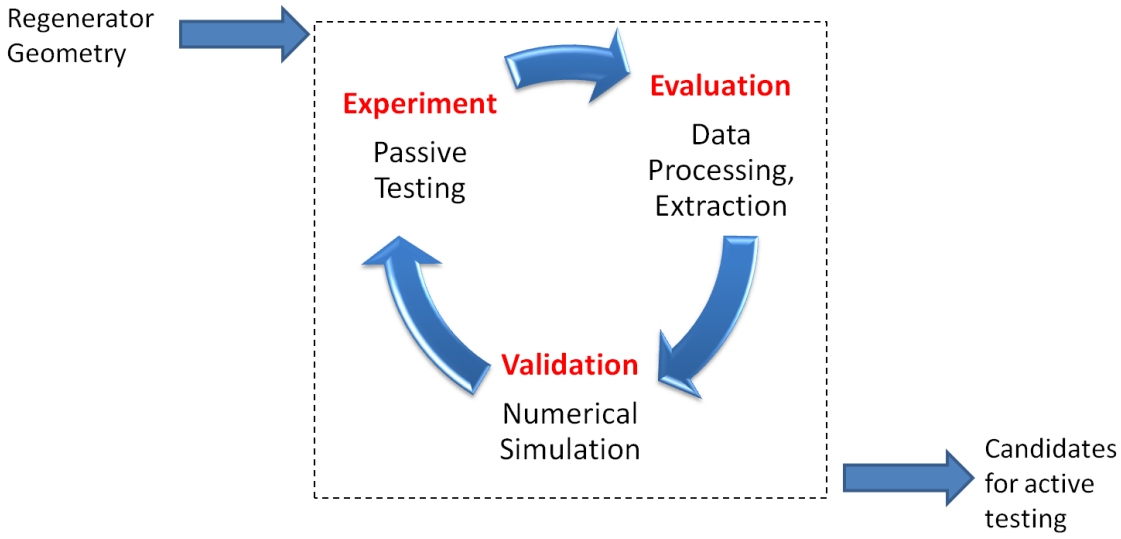

Figure 1.2: Schematic of testing process

1.4 Thesis Objective

A vast amount of literature exist that deals with the optimization of passive regenerators used in gas compression devices. Very few, however, deal with heat transfer under oscillating flow conditions using water as a heat transfer fluid as in the present work. Often the packing geometry to be characterized is randomly distributed (such as in particle or crushed particle beds) making direct simulation for extraction of heat transfer data difficult.

This work aims to establish a clear experimental and theoretical methodology to extract effective hydraulic and thermal transport properties. This objective requires the following activities:

1. Experimentation. This involves minor apparatus modifications, machine care for smooth operation, data acquisition handling. Data collection by varying operating parameters as frequency, stroke, heater and cooling load using a microchannel and spheres regenerator.

2. Creation of object oriented environment for automated signal processing and data manipulation.

3. Parameter extraction (Nusselt number and friction factor) of experimental data using simplified macroscopic thermodynamic models.

4. Validation of experimentally found parameters using microscopic thermodynamic models (pore level) on a repetitive element of the microchannel regenerator.

The thesis will begin with an overview of previous work and a literature review. The first part of this thesis deals with development, application and validation of macroscopic and microscopic models. In the second part, an experimental set up is presented that allows for testing of various regenerator geometries. In the first two chapters of the first part (3) and (4), macroscopic transport equations are introduced and analyzed regarding their application to experimental data for the extraction of friction factor and Nusselt number. Chapter (5) offers a theoretical option to calculate friction factor and Nusselt number. The results of this chapter are theoretically validated against the findings of chapter (4).

The second part starts with a description of how the theory presented in part 1 can be applied to an experiment (chapter (7)) followed by an introduction of the experimental set up with presentation of raw experimental data in chapter (8). Experimental results and evaluation of friction factor and Nusselt numbers are given in chapter (10).

Finally, conclusions and recommendations for future work are given at the end of each part of this thesis.

Chapter 2

Previous Work and Literature Review

Regenerators are key components of many different thermal devices, and thus have been studied for many years. Many excellent references are available, e.g. Schmidt and Wilmott [1], [4], [5]. Research on regenerators has many different facets; much of the experimental work falls into the cryogenic regime, where the regenerator is used in Stirling cryocoolers. Typically these devices utilize a gas as working fluid which is very different from the present experimental conditions. Hence, these references are only of conceptional use for the present work. Most of the hydraulic and thermal characteristics of regenerators are studied within the more general concept of porous media. There is a large number of publications that concerns thermal energy and momentum transport through porous media. Many studies are limited to porous media in form of packed particle beds because of their high interfacial area. Wakao and Kaguei [6] presented a comprehensive review on techniques for the extraction of the heat transfer coefficient. They found significant scattering of the resulting correlations for the Nusselt number especially at low Reynolds number flows. Achenbach [7] points out in his review, that the large parameter space for the Nusselt number is responsible for large experimental scattering. Hence, the various experimental conditions can not be generalized to represent the Nusselt number in an infinitely packed porous bed. Achenbach [7] points out that the ratio of hydraulic diameter to regenerator diameter and the non uniform void distribution in the radial direction (channelling) are often not considered in the experimental determination of the Nusselt number.

Another point that must be considered is what thermal transport phenomena have been taken into account for the determination of the Nusselt number. Hsu [8] gives an excellent review for the use of macroscopic transport equations de-

rived from volume averaging techniques. The closure of these equations requires additional terms in the energy balance: interfacial heat transfer (constituted by the Nusselt number), thermal dispersion and thermal tortuosity. In addition, effective thermal conductivities appear in the balance equations from volume averaging. In theory, all these ”new” macroscopic transport processes described by constitutive relations must be determined experimentally. A simultaneous determination of the closure coefficients is unlikely. Hence, single experiments must be carried out to determine the coefficient in question. For particle beds, the correlation presented by Wakao and Kaguei [6] evolved as a benchmark and is often used for modeling and simulation of particle beds. In their work they included thermal dispersion in the energy balance to extract the Nusselt number. Often thermal turtuousity is not considered at all. Another approach is chosen by Hausen [9], he neglected conductive transport completely (and therewith thermal dispersion) and came up with a bulk heat transfer coefficient that embodies interfacial heat transfer and resistance to heat transfer within the regenerator packing and the the fluid. Thus, it is not surprising that the different models used to extract heat transfer data will amplify the scattering in Nusselt number predictions.

Recently, Engelbrecht [10] came up with a new Nusselt number correlation for packed bed of spheres with diameter 4mm. He investigated the heat transfer using water and water-glycol mixtures as heat transfer medium. The regenerator dimensions are very similar to the present work. He found that his new correlation significantly under predicts the Wakao correlation (derived for gaseous heat transfer fluids). He also found a large experimental uncertainty of the Nusselt number which is amplified by the temperature dependence of Reynolds and Prandtl number. His correlation turned out to be close to the one presented by Macias-Machin et al [11] who investigated Nusselt number for liquid heat transfer fluids only.

It must be pointed out that all the work reviewed to this point corresponds to the so called “single-blow“ technique. In this technique the regenerator is fluidized at a constant flow rate. At the beginning of the experiment the regenerator is subjected to a quasi step change in temperature. Simultaneously, the temperature is recorded downstream of the regenerator. The temperature residual of model and experiment downstream of the regenerator is minimized by an appropriate choice of the heat transfer coefficient determined by a least square estimator. This method only approximates the heat transfer in regenerators since the flow in thermal regenerator operation is oscillating.

Recently, Sarlah and Poredos [12] approximated the regenerator operation by separated single blows to simulate two complete cycles by two cold and two hot single blows. They came up with Nusselt number correlations for packed bed regenerators and triangular channels (isosceles). Their correlations are remarkably close to to ones presented in Kays and London [13].

None of the previously reviewed papers discusses the effects of an oscillating flow which represents a typical operating condition of many thermal devices using a regenerator. Many studies deal with the analysis of heat transfer under oscillating flow conditions in channels and pipes without porous media.

Lee et al [14] presented an experimental study of oscillating flow in wire mesh regenerators. Their study compares regenerators with different wire mesh numbers but the same porosity. Their experimental set up is very similar to the one presented in this thesis. However, the fact that they used a gaseous heat transfer fluid does not allow for a direct comparison to experimental situations with incompressible flow as investigated in this thesis. They measured temperatures and pressure losses between frequencies of 1-10 Hz at a fixed stroke. They placed three thermocouples inside the regenerator and two outside. They measured negligible temperature oscillations inside the regenerator and attributed this finding to the low stroke, the compressibility of the gas and the regeneration effect. They also showed that a regenerator made up of a combination of wired mesh using different mesh numbers can increase the effectiveness of the regenerator. However, they do not show a correlation for the Nusselt number.

Daney [15] compared ineffectiveness of parallel plates, screens and spheres regenerators in oscillating flow to a square-wave mass flow form. He modified effectiveness values [13] for constant mass flow rates to oscillating flow situations. For all regenerator geometries, he found an increase of ineffectiveness when sinusoidal flow is used. However, it is difficult to draw strong conclusions from this because of the simplified model he used. In fact, he assumed infinite thermal mass of the regenerator and in-phase evolution of the Nusselt number with respect to the mass flow.

The work of Chen et al [16] is dedicated to the analytical calculation of the Nusselt number for a gaseous flow through a parallel plate or circular tube regenerator in an oscillating flow. They assumed a periodic form for the velocity, temperature and pressure field and found closed form solutions for the complex Nusselt number. The calculation is executed on a representative element of the channel (i.e. a

single channel or tube). They also neglected temperature oscillations in the matrix (infinite thermal mass of the regenerator material). The Nusselt expression obtained is decomposed in two contributions; one due to a mean temperature gradient present, the other due to a the compressibility of the gas. In the low frequency range, they obtained Nusselt numbers for parallel plates $\mathrm{Nu} \approx 10$ and for circular tubes $\mathrm{Nu} \approx 6$.

An excellent review of oscillating flow in Stirling engines is given by Simon and Seume [17]. Their survey discusses the use of proper similarity parameters for oscillating flow as for example the kinetic Reynolds number (dimensionless frequency). The differences between steady flow and oscillating flow are illustrated for the flow in a pipe. A parabolic velocity profile is found when the flow is steady or at low oscillating frequency. As the frequency increases and annular effect is observable where the velocity peaks close to the wall. They stress that there is no clear indication for the transition from laminar to turbulent flow in porous media under oscillating flow conditions.

A study that falls in the category of oscillatory heat transfer in plain media was presented by Zhao and Cheng [18]. They experimentally and numerically investigated the heat transfer in a heated pipe subjected to oscillatory flow. A constant heat flux is applied to the pipe using an insulated flexible heater wrapped around the pipe wall. They found good agreement between the model and temperature measurements at different axial positions (center line of the pipe) as well as in the fluid pipe. They showed that the fluid temperature oscillations are smaller at the center axial positions than at the ends of the pipe. At the axial center position of the pipe wall the temperature oscillations become vanishingly small. They obtained a Nusselt number correlation that is monotonically increasing in both frequency and stroke. In the low stroke and low frequency range, they predicted a Nusselt number of 0.6 and in the high frequency (10 Hz)/high stroke range a Nusselt number of 12.5.

It can be concluded that heat transfer in regenerators is typically analyzed under steady flow conditions using a gas as heat transfer medium. Oscillating flow type heat transfer using a high density fluid (such as water) has been studied theoretically or experimentally but not combined. The experimental work reviewed is limited to the presentation of raw experimental data without presentation of meaningfull dimensionless groups such as Nusselt number and friction factor. On

the other hand, the theoretical work lacks experimental justification.

This work presents both experimental and theoretical analysis as well as the representation of pressure drop and heat transfer coefficients in terms of dimensionless numbers.

Part I

Model Development and Validation

Chapter 3

Macroscopic Balance Equations

3.1 Modeling Strategy

This chapter deals with the mathematical description of relevant transport processes in a regenerator. Models are presented that hold on the macroscopic scale. The models for the pore scale are presented in the next chapter. This differentiation of length scales offers two independent strategies for the extraction of hydraulic and thermal transport properties. The derivation, physical meaning and solution procedure and application to experimental data for the macroscopic models is discussed in this chapter.

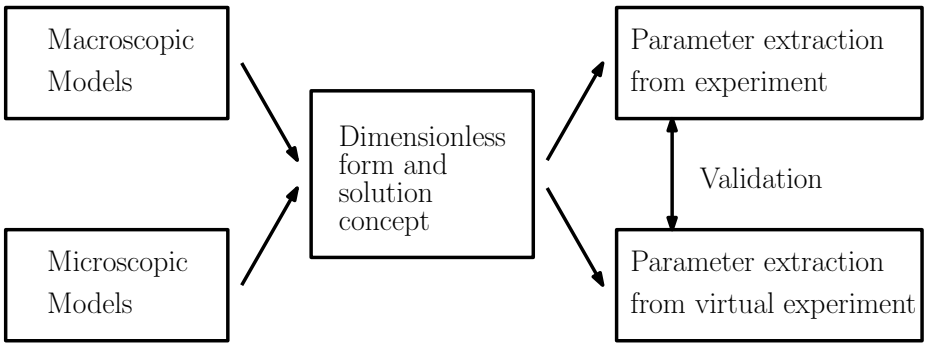

Figure 3.1: Scheme of modeling strategy

Figure (3.1) gives a schematic overview of the modeling strategy used. The non-dimensionalization and solution concept is the same for both strategies. The parameters obtained from these strategies can be validated against each other. The extraction of the Nusselt number from experiments is of particular interest.

3.2 Regenerator Disposition

The regenerator is embedded in a hydraulic circuit as shown in figure (3.2). The

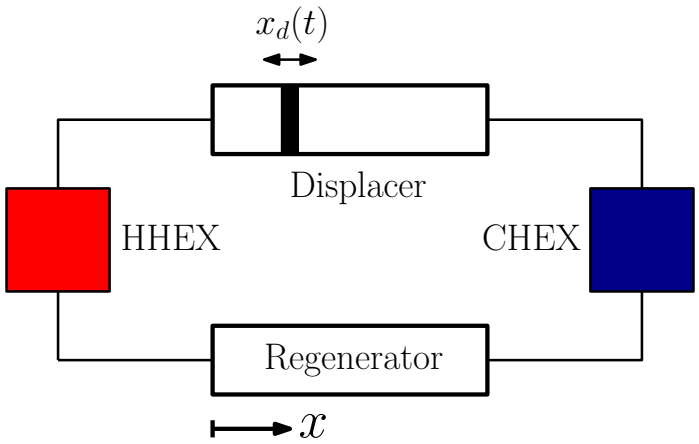

Figure 3.2: Regenerator situation in hydraulic circuit

set up depicted in figure (3.2) represents the experimental configuration covered in chapter (8). The two heat exchangers are hooked up to a heater and chiller unit respectivley and impose a temperature gradient across the regenerator. The displacer produces periodic mass flow at any point in the circuit. The following sections focus on mathematical description of the transport processes in the regenerator.

3.3 Length Scales and Volume Averages

Regenerators can be understood as porous media. The existence of at least two different length scales is characteristic for these media: the typical diameter of the pores d and the device length L as illustrated in figure (3.3) In practice, the pore characteristic dimension can be $d \approx 100\mu$m while the device length may be $L \approx 10$cm or longer. An attempt to solve the governing equations for the whole device length resolved on the pore scale is not recommendable. An immense computational effort would be needed to specify a computational grid and boundary conditions for the regenerator. The solution to this problem is the description of physically relevant fields only on a average basis. The approach presented in [19], [20] deduces effective transport equations for suitably defined volume averages of

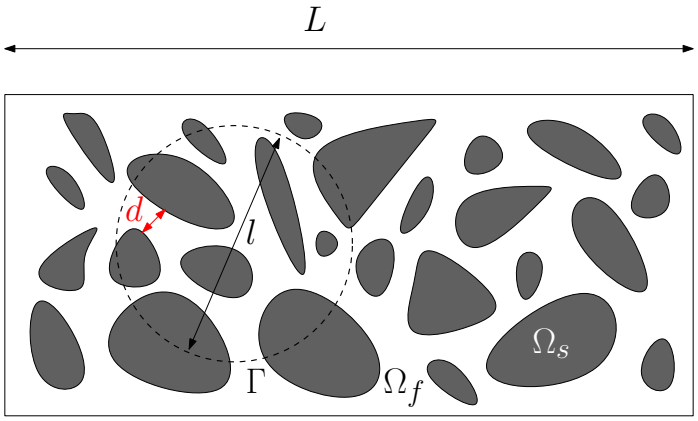

Figure 3.3: Schematic of porous media

the true physical quantities. Any physical quantity ψ (tensor of any order) can be averaged over a representative elementary volume (REV) denoted V_Γ

$$\langle \psi \rangle = \frac{1}{V_\Gamma} \int_\Gamma \psi \mathrm{d}V \tag{3.1}$$

The local REV V_Γ is chosen such that it is the smallest differential volume that results in statistically meaningful local average properties. In regenerators, the pore scale is much smaller than the device scale (the regenerator length L_r) $d \ll L_r$. Hence the variation of a physical quantity across the pore scale is negligible compared to the variation across the device length. So we are free to choose the size of a REV such that its scale is larger than the pore scale, but smaller than the device scale.

$$d \ll l \ll L_r \tag{3.2}$$

An example to locally averaged quantity is the superficial (or Darcian) velocity

$$\langle \boldsymbol{v} \rangle \equiv \boldsymbol{v}_s = \frac{1}{V_\Gamma} \int_\Gamma \boldsymbol{v}(\boldsymbol{x}) \mathrm{d}V \tag{3.3}$$

Another example is the porosity. The porosity can be calculated by introducing a void distribution function [20]

$$a(\boldsymbol{x}) = \begin{cases} 1 & \boldsymbol{x} \in \Omega_f \\ 0 & \boldsymbol{x} \in \Omega_s \end{cases} \tag{3.4}$$

Where Ω_f and Ω_s denote the fluid and solid domain as indicated in figure (3.3).

These two domains build the whole regenerator domain $\Omega_r = \Omega_f \cup \Omega_s$. The local average porosity is the average of the void distribution function

$$\epsilon(\boldsymbol{x}) = \frac{1}{V_\Gamma} \int_\Gamma a(\boldsymbol{x}) \mathrm{d}V \tag{3.5}$$

Hence, the bulk porosity is obtained by setting the REV equal to the regenerator volume $V_\Gamma = V_r$. Then equation (3.5) becomes

$$\epsilon = \frac{1}{V_r} \int_{\Omega_r} a(\boldsymbol{x}) \mathrm{d}V = \frac{1}{V_r} \int_{\Omega_f} \mathrm{d}V = \frac{V_f}{V_r} \tag{3.6}$$

With the definition of the porosity we can also average any physical quantity over the fluid or solid phase only, a so called intrinsic average

$$\langle \psi \rangle^f = \frac{1}{V_{\Gamma_f}} \int_{\Gamma_f} \psi \mathrm{d}V = \frac{\langle \psi \rangle}{\epsilon} \tag{3.7}$$

where the volume occupied by the fluid within Γ is denoted by $V_{\Gamma f} = \int_\Gamma a(\boldsymbol{x}) \mathrm{d}V$. As an example we consider the pore velocity as an intrinsic average

$$\langle \boldsymbol{v} \rangle^f \equiv \boldsymbol{v}_p = \frac{1}{V_{\Gamma_f}} \int_{\Gamma_f} \boldsymbol{v}(\boldsymbol{x}) \mathrm{d}V = \frac{\boldsymbol{v}_s}{\epsilon} \tag{3.8}$$

3.4 Macroscopic Balance Equations

The macroscopic balance equations are obtained by volume averaging the microscopic transport equations (A.2) and (A.3). The set of equations that is obtained by rigorously applying volume averaging is detailed in Appendix (A). The general set for momentum (A.5) and energy (A.7), (A.8) are too complex to apply to experimental data. We constrain the analysis by reducing the equations for one dimensional flow and heat transfer in axial direction x.

3.4.1 Macroscopic Momentum Balance

For axial superficial flow, equation (A.5) simplifies to an extended form of Darcy's law,i.e.

$$-\frac{\mathrm{d}p}{\mathrm{d}x}+\frac{\rho}{\epsilon}\frac{\mathrm{d}v_s}{\mathrm{d}t} = \frac{b_{sf}}{\epsilon} \tag{3.9}$$

$$= -\frac{\mu v_s}{K}-F\rho\frac{|v_s|v_s}{\sqrt{K}} \tag{3.10}$$

where p is the volume averaged pore pressure, i.e. $p = \langle p\rangle^f$. The term b_{sf} is the interfacial force that is specified by K, the hydraulic permeability and F, the Forchheimer factor. The latter two must be determined experimentally. Ergun [21] argued that the Forchheimer coefficient is given by $F = b/\sqrt{a\epsilon^3}$. For $F = \mathrm{d}v_s/\mathrm{d}t = 0$ equation (3.10) reduces to the well known Darcy's law. Darcy's law holds only in the low frequency limit where the rate of change of velocity is sufficiently small such that inertial effects can be ignored (quasi-steady regime). Under real oscillating flow conditions, the total pressure drop consists also of an inertial component that is proportional to the rate of change in velocity. This is analogous to an

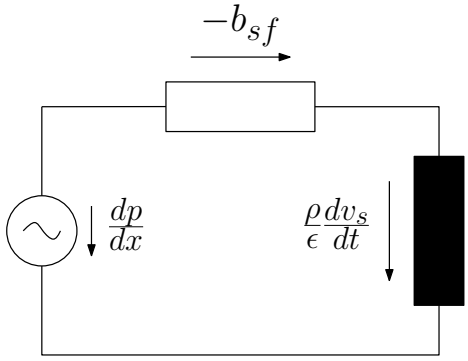

Figure 3.4: Analogy of hydraulic and electrical circuit for oscillating flow

electrical RL circuit such as in a electromagnetic coil where electromotive forces are induced that oppose the current [22]. In terms of a hydraulic circuit the resistive component is given by $-b_{sf}$ and inductive component by $-\rho/\epsilon\mathrm{d}v_s/\mathrm{d}t$. The AC-voltage battery represents then the total pressure gradient in the circuit as illustrated in figure (3.4). In general, dissipative, capacitive and inductive effects are combined in a system. In the present system the capacitive component can be excluded because of the incompressible flow assumption (A.1).

Table 3.1: Unknown coefficients in thermal energy balance

G	A_D	h_{sf}
Thermal turtuosity coefficient	dispersion coefficient	interfacial heat transfer coefficient

3.4.2 Macroscopic Thermal Energy Balance

In general the macroscopic thermal energy balances (A.7), (A.8) are too complex to apply to actual experimental data because they contain three unknowns.

These unknown coefficients are listed in table (3.1). There are many heat transfer coefficient based models appearing in literature which are essentially simplified versions of (A.5) and (A.7). These are generally for the one dimensional Darcean flow and heat transfer in axial direction. Thus, the thermal conductivity in radial direction is assumed to be infinite resulting in a homogeneous temperature distribution in the radial direction. Two such models are shown here to discuss their complexity [20].

1. Schumann model
   This is the simplest and least resolved of all models. Axial thermal conduction is neglected in both phases and no viscous dissipation is taken into account. The effect of thermal turtuosity is neglected completely. The Schumann model is given by the two thermal balance equations

$$\frac{\partial T_f}{\partial t} = -v_p \frac{\partial T_f}{\partial x} + \frac{h a_{sf}}{\epsilon(\rho c)_f}(T_s - T_f) \tag{3.11}$$

$$\frac{\partial T_s}{\partial t} = -\frac{h a_{sf}}{(1-\epsilon)(\rho c)_s}(T_s - T_f) \tag{3.12}$$

   For a simplified notation $\langle T \rangle^f = T_f$, $\langle T \rangle^s = T_s$ is used. The advantage of this model is, that h is the only unknown which must be determined experimentally. It is assumed that h also includes thermal dispersion, turtuosity and other effects which are not captured by the model.

2. Continuous solid model
   In this model the axial conduction, in both phases, is included through the use of effective thermal conductivities κ_f^{eff}, κ_s^{eff}. The effective thermal diffusivity for phase k is $\alpha_k^{\text{eff}} = \kappa_k^{\text{eff}}/(\rho c)_k$

$$\frac{\partial T_f}{\partial t} = -v_p \frac{\partial T_f}{\partial x} + \alpha_f^{\text{eff}} \frac{\partial^2 T_f}{\partial x^2} + \frac{h a_{sf}}{\epsilon(\rho c)_f} (T_s - T_f) \tag{3.13}$$

$$\frac{\partial T_s}{\partial t} = \alpha_s^{\text{eff}} \frac{\partial^2 T_s}{\partial x^2} - \frac{h a_{sf}}{(1-\epsilon)(\rho c)_s} (T_s - T_f) \tag{3.14}$$

In general, the thermal conductivities are unknown and depend on the geometrical configuration and the material used. They can be obtained from correlations available in literature or from detailed simulations. Wakao and Kaguei [6], [20] also include dispersion in κ_f^{eff}. The incorporation of dispersion will result in a velocity dependency of κ_f^{eff}. However, the model comprises additional unknowns $\kappa_f^{\text{eff}}, \kappa_s^{\text{eff}}$, which must be either determined experimentally or taken from correlations available in literature. Viscous dissipation and ambient heat loss are also neglected in this model.

Out of the two models, equations equation (3.13) and equation (3.14) represent a more general form to describe non equilibrium between the two phases and is used as a basis to extract the heat transfer coefficient. The extraction of all three unknowns from a single experiment is unlikely. The dispersion and thermal turtuosity term are neglected in what follows, the effective thermal conductivities $\kappa_f^{\text{eff}}, \kappa_s^{\text{eff}}$ are treated as constants.

3.5 Solution through Harmonic Approximation

3.5.1 Strategy

The extraction of friction factor and the heat transfer coefficient using measured pressure and temperature requires the solution of equations (3.10) (3.13) and (3.14). A special method can be applied to solve the thermal energy balances referred to as harmonic approximation. This method is widely used in electrodynamics and ensures fast solution of the unknown temperature and velocity fields. Instead of solving a dynamical system directly including all transients, one solves only for the complex amplitudes and factors out all the harmonics, which yields solutions of the balance equations in cyclic steady state only. Swift et. al. [23] and deWaele et. al. [24] applied the same procedure to a similar set of equations to analyze thermoacoustic interactions.

Assuming periodic fluid mass flow due to a sinusoidal piston displacement, $x_d(t)$, allows the motion of the displacer (see figure (3.2)) to be written in terms of a single harmonic

$$x_d(t) = \frac{L_s}{2} \sin(\omega t + \varphi_x) \tag{3.15}$$

where L_s is the stroke length, ω the angular frequency, φ_x the phase. Since the flow is assumed to be incompressible, we can assume plug flow through the regenerator with magnitude

$$v_s(t) = \frac{A_{\text{disp}}}{A_r} \frac{\mathrm{d}x_d}{\mathrm{d}t} = \frac{L_s}{2} \frac{A_{\text{disp}}}{A_r} \omega \cos(\omega t + \varphi_x) \tag{3.16}$$

where A_{disp} is the effective cross sectional area of the displacer and A_r the inner diameter of the regenerator housing. For a simplified analysis we make use of complex notation

$$v_s(t) = \mathrm{Re}\left[v_{s1} \exp(i\omega t)\right] = v_{s1} \mathrm{Re}\left[\exp(i\omega t)\right] \tag{3.17}$$

where the imaginary unit $i = \sqrt{-1}$ and $v_{s1} = L_s/2A_{\text{disp}}/A_r\omega$. Note that the superficial velocity is defined to have no phase offset, i.e. $\varphi_x = 0$.

It is assumed that any variable can be expressed as a Fourier series that will describe the physical field ψ in cyclic steady state

$$\psi(x,t) = \sum_{k=-n}^{n} \psi_k(x) \exp(i\omega_k t) \tag{3.18}$$

where the Fourier coefficients are given by

$$\psi_m = \frac{1}{\tau} \int_{-\tau/2}^{\tau/2} \psi(x,t) \exp(-i\omega_m t) \mathrm{d}t \tag{3.19}$$

where $\tau = 2\pi/\omega$ is the signal period. In the remainder it is assumed that higher order harmonics can be neglected. The ansatz (3.18) reduces to

$$\psi = \psi_0 + \mathrm{Re}\left[\psi_1 \exp(i\omega t)\right] \tag{3.20}$$

Where the index 0 indicates time averaged value of ψ which has only a spatial dependency, $\psi_0 = \psi_0(x) \in \mathbb{R}$. The index 1 refers to the first harmonic (i.e. the

amplitude of the signal). Note, $\psi_1 = \psi_1(x) \in \mathbb{C}$ indicating an absolute value with corresponding phase relative to the velocity signal.

The benefit of this approach is the reduction of any partial differential equation to an ordinary differential equation with respect to the spatial variable by splitting the problem into a steady part (time averaged part ψ_0) and a transient part ψ_1.

3.5.2 Harmonic Expansion of Momentum Balance

According to (3.20), pressure gradient and interfacial force can be written as

$$\frac{\mathrm{d}p}{\mathrm{d}x} = \mathrm{Re}\left[\left(\frac{\mathrm{d}p}{\mathrm{d}x}\right)_1 \exp\left(i\omega t\right)\right] \tag{3.21}$$

$$b_{sf} = \mathrm{Re}\left[b_{sf1}\exp\left(i\omega t\right)\right] \tag{3.22}$$

Note, that both pressure gradient and interfacial force have no time averaged contribution because the time averaged velocity is equal to zero, i.e. $v_{s0} = 0$. The macroscopic momentum balance (3.10) in the harmonic approximation reads

$$-\left(\frac{\mathrm{d}p}{\mathrm{d}x}\right)_1 + \frac{\rho}{\epsilon} i v_{s1} = \frac{b_{sf1}}{\epsilon} \tag{3.23}$$

3.5.3 Harmonic Expansion of Thermal Energy Balance

Casting the ansatz (3.20) into (3.13), (3.14) yields

$$\begin{aligned} i\omega T_{f1}\exp\left(i\omega t\right) = & -\frac{1}{\epsilon} v_{s1}\exp\left(i\omega t\right)\left\{\frac{\mathrm{d}T_{f0}}{\mathrm{d}x} + \frac{\mathrm{d}T_{f1}}{\mathrm{d}x}\exp\left(i\omega t\right)\right\} \\ & + \alpha_f^{\mathrm{eff}}\left\{\frac{\mathrm{d}^2 T_{f0}}{\mathrm{d}x^2} + \frac{\mathrm{d}^2 T_{f1}}{\mathrm{d}x^2}\exp\left(i\omega t\right)\right\} \\ & + \frac{h a_{sf}}{\epsilon\left(\rho c\right)_f}\left(T_{s0} + T_{s1}\exp\left(i\omega t\right) - T_{f0} - T_{f1}\exp\left(i\omega t\right)\right) \end{aligned} \tag{3.24}$$

$$\begin{aligned} i\omega T_{s1}\exp\left(i\omega t\right) = & \alpha_s^{\mathrm{eff}}\left\{\frac{\mathrm{d}^2 T_{s0}}{\mathrm{d}x^2} + \frac{\mathrm{d}^2 T_{s1}}{\mathrm{d}x^2}\exp\left(i\omega t\right)\right\} \\ & - \frac{h a_{sf}}{\left(1-\epsilon\right)\left(\rho c\right)_s}\left(T_{s0} + T_{s1}\exp\left(i\omega t\right) - T_{f0} - T_{f1}\exp\left(i\omega t\right)\right) \end{aligned} \tag{3.25}$$

In the next step we select the fundamental Fourier components:

1. for the time averaged temperatures we integrate equations (3.24), (3.25) over a whole period

2. to select the first harmonic we make use of equation (3.19) by multiplying equations (3.24), (3.25) with $\exp(-i\omega t)$ and integrate over a whole period.

Hence, we arrive at a set of 4 coupled ODE's of second order for the time averaged temperatures and first order harmonics

$$0 = \alpha_f^{\text{eff}} \frac{\mathrm{d}^2 T_{f0}}{\mathrm{d}x^2} + \frac{h a_{sf}}{\epsilon(\rho c)_f}(T_{s0} - T_{f0}) \tag{3.26}$$

$$0 = \alpha_s^{\text{eff}} \frac{\mathrm{d}^2 T_{s0}}{\mathrm{d}x^2} - \frac{h a_{sf}}{(1-\epsilon)(\rho c)_s}(T_{s0} - T_{f0}) \tag{3.27}$$

$$i\omega T_{f1} = -\frac{1}{\epsilon} v_{s1} \frac{\mathrm{d}T_{f0}}{\mathrm{d}x} + \alpha_f^{\text{eff}} \frac{\mathrm{d}^2 T_{f1}}{\mathrm{d}x^2} + \frac{h a_{sf}}{\epsilon(\rho c)_f}(T_{s1} - T_{f1}) \tag{3.28}$$

$$i\omega T_{s1} = \alpha_s^{\text{eff}} \frac{\mathrm{d}^2 T_{s1}}{\mathrm{d}x^2} - \frac{h a_{sf}}{(1-\epsilon)(\rho c)_s}(T_{s1} - T_{f1}) \tag{3.29}$$

The first two equations govern the behavior for the time averaged temperatures where the third and fourth equation describe the temperature amplitudes about the time averaged temperature profile. Note that the solution to this set of equations will approximate the solution to the original coupled PDE given by equations (3.13) and (3.14). The relative magnitude of the divergence of the mean diffusion fluxes becomes clear when eliminating the time averaged temperature difference from equations (3.26) and (3.27), i.e.

$$0 = \frac{\mathrm{d}^2}{\mathrm{d}x^2}\left(T_{f0} + \frac{1-\epsilon}{\epsilon}\frac{\kappa_s^{\text{eff}}}{\kappa_f^{\text{eff}}} T_{s0}\right) \tag{3.30}$$

Many metals have an intrinsic thermal conductivity that is at least one order of magnitude larger than water (e.g. bronze, stainless steel).

$$\frac{\kappa_s}{\kappa_f} = \mathcal{O}(10^1) \tag{3.31}$$

The ratio of the effective thermal conductivities depends on the geometrical configuration of a certain regenerator. Geometries that are homogeneous in axial direction (e.g. parallel channels, plates etc.) will have effective thermal conductivities close to their intrinsic value (dispersion neglected). Inhomogeneous distribution of the solid material in form of spherical particles or metal screens will cause only sporadic contact between the isolated solid phases. Hence, the effective thermal

conductivities will be smaller than their intrinsic values.

For a channel-like regenerator with $\epsilon \leq 1/2$ we can thus conclude that the second expression in the bracket of (3.30) is much larger than T_{f0} such that this expression can be approximated as T_{s0}. Under theses circumstances equation (3.30) simlifies to

$$\frac{\mathrm{d}^2 T_{s0}}{\mathrm{d}x^2} \approx 0 \tag{3.32}$$

It must be noted that this simplification does not hold for geometries that have significantly lower thermal conductivities than their intrinsic values. For the further discussion about the extraction of the heat transfer coefficient we can drop equations (3.26) and (3.27) and make use of above simplification leading to constant time averaged temperature gradients.

$$\frac{\mathrm{d}T_{f0}}{\mathrm{d}x} = \frac{\mathrm{d}T_{s0}}{\mathrm{d}x} = \frac{\mathrm{d}T_0}{\mathrm{d}x} = \text{const.} \tag{3.33}$$

Consequently, we can assume equivalence for the time averaged temperatures.

3.6 Dimensionless Parameters

Standard thermo-hydraulic groupings are presented in this section that lead to suitable standardization of experimental data and the governing equations.

The hydraulic diameter standardizes the flow in an arbitrary duct. The hydraulic radius is proportional to the ratio of free flow cross sectional area A_f and wetted perimeter P_w. This ratio can be extended to a volumetric ratio, namely the ratio of entrained fluid volume V_f in the pores to interfacial surface area ($A_{sf} = a_{sf} V_r$) available for heat transfer.

$$d_h = 4\frac{A_f}{P_w} = 4\frac{V_f}{a_{sf} V_r} = \frac{4\epsilon}{a_{sf}} \tag{3.34}$$

Similarly, the characteristic length with respect to the packing material is defined as

$$l_c = \frac{V_s}{a_{sf} V_r} = \frac{1-\epsilon}{a_{sf}} \tag{3.35}$$

The ratio of hydraulic radius and characteristic length is a function of porosity only

$$\frac{d_h}{l_c} = 4\frac{\epsilon}{1-\epsilon} \tag{3.36}$$

The ratio of original coordinate to hydraulic diameter is chosen as dimensionless length

$$\xi = \frac{x}{d_h} \tag{3.37}$$

The dimensionless time is scaled with the angular frequency

$$\hat{t} = \omega t \tag{3.38}$$

The instantaneous velocity is scaled with the peak pore velocity

$$\hat{v} = \frac{v}{v_{p1}} \tag{3.39}$$

where $v_{p1} \in \mathbb{R}$ is the peak pore velocity. The pressure is non-dimensionalized with respect to dynamic pressure, i.e.

$$\hat{p} = \frac{p - p_0}{\rho v_{p1}^2} \tag{3.40}$$

The pressure gradient is accordingly,

$$\frac{\mathrm{d}\hat{p}}{\mathrm{d}\xi} = \frac{d_h}{\rho v_{p1}^2}\frac{\mathrm{d}p}{\mathrm{d}x} \tag{3.41}$$

The friction factor relates the pressure loss of a porous medium to the average velocity. The Darcian friction factor is given by

$$f_D = \frac{d_h}{2}\frac{\frac{\mathrm{d}p}{\mathrm{d}x}}{\rho v_{p1}^2} \tag{3.42}$$

The friction factor is twice the dimensionless pressure gradient

$$f_D = 2\frac{\mathrm{d}\hat{p}}{\mathrm{d}\xi} \tag{3.43}$$

The peak Reynolds number based on hydraulic diameter relates inertial forces and

viscous forces

$$\mathrm{Re}_{dh} = \frac{\rho_f v_{p1} d_h}{\mu_f} \tag{3.44}$$

where v_{p1} is the pore velocity to first order (i.e. the peak pore velocity). The peak velocity can reach the same value for a low frequency/ high stroke and high frequency/low stroke configuration. The kinetic Reynolds number is a dimensionless expression for the oscillating inertial forces in relation to viscous forces.

$$\mathrm{Re}_{\omega} = \frac{\rho_f \omega d_h^2}{\mu_f} \tag{3.45}$$

More commonly used for the description of oscillating flow is the Womersley number $\mathrm{Wo} = \sqrt{\mathrm{Re}_{\omega}}$. Under higher frequencies where Re_{ω} and Wo are large, viscous forces become less important resulting in plug like flow. Under small frequencies the flow might deviate from the plug profile since the flow has time to develop a flow profile within a cycle. The kinetic Reynolds number can also be considered as a non dimensional frequency. Beside frequency, the stroke of the displacer can also be controlled. The non dimensional displacement is given by the ratio of stroke L_s and hydraulic diameter.

$$A_0 = \frac{L_s^{\text{eff}}}{2\epsilon d_h} = \frac{L_s}{2\epsilon d_h}\frac{A_{\text{eff}}}{A_r} \tag{3.46}$$

Here the effective stroke takes into account the different cross sectional areas of displacer A_{disp} and the regenerator A_r. Using these definitions the peak Reynolds number, kinetic Reynolds number and non dimensional amplitude relate to

$$\mathrm{Re}_{dh} = \mathrm{Re}_{\omega} \cdot A_0 \tag{3.47}$$

The Nusslet number is the ratio of convective thermal energy transfer to conductive energy transport [1]

$$\mathrm{Nu} = \frac{h \cdot d_h}{\kappa_f} \tag{3.48}$$

Similarly, the heat transfer coefficient can be non-dimensionalized with respect to conductive energy transport in the packing material, known as Biot number

$$\mathrm{Bi} = \frac{h \cdot l_c}{\kappa_s} \tag{3.49}$$

[1] the conductive transport is understood to occur in a stagnant environment (i.e. no fluid motion)

The Prandtl number is the ratio of viscous diffusion to thermal diffusion.

$$\mathrm{Pr} = \frac{c_f \mu_f}{\kappa_f} \tag{3.50}$$

The Fourier number is conceptually the ratio of the heat conduction rate to the rate of thermal energy storage, i.e. $\mathrm{Fo} = \alpha_s t_0 / l_c^2$, where t_0 is a characteristic time scale. In oscillating flow it is reasonable to pick $t_0 = 1/\omega$. The Fourier number is

$$\mathrm{Fo} = \frac{\alpha_s}{l_c^2 \omega} \tag{3.51}$$

The ratio of the intrinsic thermal conductivities of both phases is defined as

$$\gamma_k = \frac{\kappa_f}{\kappa_s} \tag{3.52}$$

The ratio for fluid to solid thermal mass is

$$R = \frac{\epsilon}{1-\epsilon} \frac{(\rho c)_f}{(\rho c)_s} \tag{3.53}$$

The thermal mass ratio can be related to a combination of the present groupings as

$$R = \frac{\mathrm{PrRe}_\omega \mathrm{FoBi}}{4\mathrm{Nu}} \tag{3.54}$$

The ratio of Nusselt to Biot number is

$$\frac{\mathrm{Nu}}{\mathrm{Bi}} = \frac{d_h}{l_c} \frac{1}{\gamma_k} = \frac{4\epsilon}{1-\epsilon} \cdot \frac{1}{\gamma_k} \tag{3.55}$$

To non-dimensionalize the temperature oscillations to first order, the physical operating condition resulting in highest temperature oscillations must be identified. At high frequencies $\omega \to \infty$ the characteristic time for conduction/diffusion or interfacial heat transfer to occur is much higher than the cycle time. Taking the limit $\omega \to \infty$ of equation (3.28) yields

$$\begin{aligned} iT_{f1} &= -\frac{v_{p1}}{\omega} \frac{\mathrm{d}T_{f0}}{\mathrm{d}x} \\ &= -A_0 \frac{\mathrm{d}T_{f0}}{\mathrm{d}\xi} \end{aligned} \tag{3.56}$$

The physical interpretation of this limit corresponds to a oscillating flow in an isolated duct. The temperature amplitudes get higher as both the displaced volume (proportional to A_0) and the temperature difference across the duct is increased. There are no temperature oscillations if the time averaged temperature profile is isothermal. At these high frequencies, the temperature lags the velocity by $\pi/2$ indicating the first order[2] nature of thermal systems. As a consequence, the temperature oscillations can be scaled with the maximum possible temperature amplitudes by

$$\theta_{f1} = -\frac{T_{f1}}{A_0 \frac{\mathrm{d}T_{f0}}{\mathrm{d}\xi}} \tag{3.57}$$

For the solid equation, the same scaling law applies. The negative sign is used to counteract the negative time averaged temperature gradient. This assures same phase angles of θ_{f1} and T_{f1}. It must be pointed out that the sign $\mathrm{d}T_{f0}/\mathrm{d}\xi$ depends on the reference frame chosen. The reference frame is shown in figure (3.2) and points from hot to cold end indicating $\mathrm{d}T_{f0}/\mathrm{d}\xi < 0$.

3.7 Dimensionless Form of Macroscopic Governing Equations

The dimensionless macroscopic momentum balance (3.23) is

$$\left(\frac{\mathrm{d}\hat{p}}{\mathrm{d}\xi}\right)_1 = -\frac{i}{A_0} + \left(\frac{c_1}{A_0 \mathrm{Re}_\omega} + c_2\right) \tag{3.58}$$

Note that the the last term represents represents the dimensionless form of the interfacial force. The coefficients c_1 and c_2 are unknown and must be determined experimentally.

The thermal energy balances (3.28) and (3.29) using dimensionless parameters are given by

$$i\theta_{f1} = 1 + \frac{1}{\mathrm{Pr}\mathrm{Re}_\omega}\left(\frac{\kappa_f^{\mathrm{eff}}}{\kappa_f}\right)\frac{\mathrm{d}^2\theta_{f1}}{\mathrm{d}\xi^2} + 4 \cdot \frac{\mathrm{Nu}}{\mathrm{Pr}\mathrm{Re}_\omega}\left(\theta_{s1} - \theta_{f1}\right) \tag{3.59}$$

$$i\theta_{s1} = \mathrm{Fo}\left(\frac{l_c}{d_h}\right)^2\left(\frac{\kappa_s^{\mathrm{eff}}}{\kappa_s}\right)\frac{\mathrm{d}^2\theta_{s1}}{\mathrm{d}\xi^2} - \mathrm{FoBi}\left(\theta_{s1} - \theta_{f1}\right) \tag{3.60}$$

[2]The thermal energy balance contains only a first order time derivative

The ratio $\kappa_f^{\text{eff}}/\kappa_f$ and $\kappa_s^{\text{eff}}/\kappa_s$ describes the ratio of effective thermal conductivity to intrinsic thermal conductivity. Equations (3.59) and(3.60) describe the non-dimensional form of original balance equations (3.13) and(3.14) in the first order harmonic approximation. A simple experiment is schematically described in the next chapter to illustrate how the above set can be applied to extract the friction factor and the Nusselt number from this experiment.

Chapter 4

Friction Factor and Nusselt Number

This section discusses how the governing equations can be used to extract friction factor and Nusselt number from an actual experiment. The simplest experimental set up possible to extract friction factor and Nusselt number within the previously discussed model framework is presented in figure (4.1). Pressure transducers are

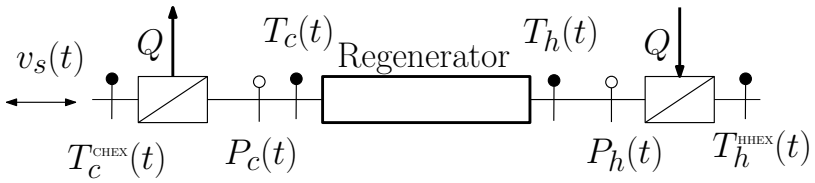

Figure 4.1: Schematic of fundamental experiment for extraction of friction factor and Nusselt number

needed on both sides of the regenerator in order to characterize the friction factor as shown in figure (4.1). In addition two thermocouples on both ends of the regenerator are needed. The additional thermocouples at the heat exchanger ends are not directly needed but are shown here for further analysis. The superficial velocity is controlled by the parameters A_0 and Re_ω. The dimensionless temperatures are obtained by decomposing the temperature readings in time averaged and first order harmonics.

In the following sections, limiting cases of the governing equations are analyzed and used to identify restrictions with respect to pressure and temperature oscillations.

4.1 Friction Factor

The friction factor can be calculated by measuring the pressure drop across the regenerator. The friction factor is given by

$$f_D = 2\left(\frac{\mathrm{d}\hat{p}}{\mathrm{d}\xi}\right)_1 \tag{4.1}$$

The measured pressure drop is normalized with respect to the phase angle of the piston velocity and will in general be a complex number. Likewise, the friction factor will also be a complex number with same phase angle as the pressure drop normalized with respect to the piston velocity.

4.2 Nusselt Number

4.2.1 Nusselt Number from direct Solution of Governing Equations

The recovery of the Nusselt number involves the solution of the coupled ordinary differential equations (3.59) and (3.60). Figure (4.1) shows that only fluid temperatures are recorded in the simplest version of an experimental set up. In general the solid temperature will be difficult to measure since the thermocouple would be partially immersed into the oscillating fluid. Rather than making an assumption for the boundary conditions on the solid domain, it is assumed that heat diffusion to first order is negligible [1]. This will result in a Nusselt number that embodies both interfacial heat transfer and effective axial thermal conductivity. Also, this simplified model for first order temperature oscillations corresponds to the Schumann model as described by equations (3.11) and (3.12). The corresponding dimensionless equations are

$$i\theta_{f1} = 1 + 4\cdot\frac{\mathrm{Nu}}{\mathrm{Pr}\ \mathrm{Re}_\omega}\left(\theta_{s1}-\theta_{f1}\right) \tag{4.2}$$

$$i\theta_{s1} = -\mathrm{BiFo}\left(\theta_{s1}-\theta_{f1}\right) \tag{4.3}$$

[1] As the frequency increases this assumption is well justified because the cycle time decreases and will be much smaller than the characteristic time for diffusion to occur

We note that both equations are now independent of position. Typically, the governing equations are solved for the unknown extensive quantity, i.e. in this case, the fluid temperature oscillations. The solid temperature oscillations can be eliminated by noticing that the temperature difference to first order can be expressed in terms of the fluid oscillations only

$$\Delta\theta_1 = \theta_{s1} - \theta_{f1} = -iR - (R+1)\,\theta_{f1} \tag{4.4}$$

where we have used the identity

$$\frac{1}{R} = \frac{4\mathrm{Nu}}{\mathrm{PrRe}_\omega \mathrm{BiFo}} \tag{4.5}$$

Using equation (4.4), the fluid temperature to first order can be written as a function of the Nusselt number

$$\theta_{f1} = \frac{4R\mathrm{Nu} + i\mathrm{PrRe}_\omega}{i4\mathrm{Nu}(R+1) - \mathrm{PrRe}_\omega} \tag{4.6}$$

The solution to the Schumann model under oscillating flow conditions is a function of the operating conditions Re_ω, material properties R, Pr and the Nusselt number Nu. The temperature oscillations can be written as

$$\theta_{f1} = \frac{4\mathrm{NuPrRe}_\omega}{\left(4\mathrm{Nu}(1+R)\right)^2 + \left(\mathrm{PrRe}_\omega\right)^2} - i\frac{\left(4\mathrm{Nu}\right)^2 R\,(1+R) + \left(\mathrm{PrRe}_\omega\right)^2}{\left(4\mathrm{Nu}(1+R)\right)^2 + \left(\mathrm{PrRe}_\omega\right)^2} \tag{4.7}$$

where the above solution results from three assumptions:

1. Simple harmonic representation of all quantities.
2. Constant time averaged temperature gradient.
3. Negligible axial conduction/diffusion in both phases (i.e. embodied in Nusselt number).

The Nusselt number can be extracted using experimentally obtained fluid temperatures θ_{f1} by solving (4.6) for the Nusselt number

$$\mathrm{Nu} = \frac{\mathrm{PrRe}_\omega}{4}\frac{\mathcal{E}}{iR\mathcal{E} - 1} \qquad \text{where} \qquad \mathcal{E} = \frac{i\theta_{f1} - 1}{\theta_{f1}} \tag{4.8}$$

It can be seen that the Nusselt number is in general a complex number. The next section discusses the meaning and application of a complex Nusselt number.

4.2.2 Complex Nusselt Number

The outcome of the previous section is an expression for the Nusselt number. In general, the Nusselt number in oscillatory flow is a complex number. The idea of a complex Nusselt number is not a novelty and is reported in a few publications, e.g. Chen et. al. [16]. Since the regeneration process is often approximated as discrete single blow waves varying between $\pm v_s$ the use of a complex Nusselt number is not obvious. However, the concept of a complex Nusselt number is often used in analysis of cryogenic regenerators and thermoacoustic devices. The existence of a non-zero imaginary part of the Nusselt number is simply attributed to an apparent phase difference between the interfacial heat flux [2]$\hat{q}$ and the bulk mean temperature difference $\Delta\theta_1$ [25]. However, this is more of a mathematical reason and justifies the use of a complex Nusselt number in order to fulfil the energy balance in the complex plane.

The phase difference between heat flux and temperature difference is zero at low frequencies because the bulk mean regenerator temperature increases almost instantaneously if it is subjected to a heat flux from fluid to solid . The regenerator operation is then quasi-steady. In this low frequency limit the imaginary part of the Nusselt number is thus vanishingly small.

As the frequency increases the bulk regenerator temperature will no longer react instantaneously because of the thermal mass and internal resistance (conduction) of the solid material. In other words, thermal inertia will cause a time delay that is understood as a phase difference between heat flux and bulk temperature difference.

The existence of this phase lag causes non zero interfacial heat fluxes $\hat{q}$ even though the bulk mean temperature is zero $\Delta\theta_1 = 0$. We recall that both $\hat{q}$ and $\Delta\theta_1$ are macroscopic properties. On the microscopic level (i.e. the pore level) the interfacial heat flux is given by

$$Q_{sf} = \int_{\partial\Omega_f} -\kappa_f \nabla T \mathrm{d}\boldsymbol{S} \tag{4.9}$$

[2]From equation (4.2) we can define $\hat{q} \doteq 4\mathrm{Nu}\Delta\theta_1 = \mathrm{PrRe}_\omega(\theta_{f1} - 1)$

Even though if $\Delta\theta_1 = 0$ the microscopic interfacial heat flux Q_{sf} can be non zero. In this sense, the imaginary part of Nu is related to the heat transfer that occurs at $\Delta\theta_1 = 0$.

It is concluded that similar to the imaginary part of a electric impedance, the imaginary part of the Nusselt number can be understood as type of thermal reactance. However, in this context a non zero imaginary part of the Nusselt number is not expected because of the initial assumption that the radial thermal conductivity is infinitely large in both phases and will not cause a phase lag between heat flux and bulk temperature difference. This becomes clear by considering the thermal penetration depth given by [26]

$$\delta_{\mathrm{th}} = 2\sqrt{\alpha_s t} \tag{4.10}$$

The above equation must be interpreted on a microscopic scale. The penetration depth indicates the distance from the fluid solid interface through which thermal energy is transported by conduction. The desired penetration depth for a regenerator is of the order of the solid characteristic length L_c. The time required to penetrate into the solid matrix depends on the thermal conductivity. The penetration time approaches zero as $\kappa_{\mathrm{s}} \to \infty$ indicating that the solid temperature will be homogeneous. In addition the solid temperature will respond without time lag if a heat flux is present at the fluid-solid interface that is driven by the temperature difference of solid and fluid phase. Under these conditions, it can be concluded that the Nusselt number must be a real number. This qualitative conclusion of a zero imaginary part is numerically confirmed in chapter (5).

4.2.3 Nusselt Number from Time Averaged Energy Flux

This chapter provides another expression for the Nusselt number that is based on real quantities only and will thus provide an expression for the real part of the Nusselt number.

The passive regenerator is situated between two heat exchangers that are hooked up to a chiller and heater unit, respectively (figure (4.1)). If the heat exchangers, piping and the regenerator are perfectly insulated the energy flux that enters the system through the hot heat exchanger must go through the regenerator and leave through the cold heat exchanger. In the regenerator the energy flux is time de-

pendent because of the oscillating mass flow in the test circuit. However, the time averaged energy flux in the regenerator must correspond to the energy flux that is emitted or absorbed by the HHEX and CHEX, respectively. The instantaneous energy flux based on the Schuman model (3.11) and (3.12) is given by

$$\begin{aligned} j_{\text{th}}(t) &= (\rho c)_f v_s(t) T_f(t) && (4.11)\\ &= (\rho c)_f \text{Re}\left[v_{s1}\exp(i\omega t)\right]\text{Re}\left[T_{f0}+T_{f1}\exp(i\omega t)\right] && (4.12)\end{aligned}$$

The corresponding balance equation over solid and fluid phase reads

$$\frac{\partial E_{th}}{\partial t} = -\frac{\partial j_{\text{th}}}{\partial x} \tag{4.13}$$

Where the accumulated thermal energy is given by (formally obtained by eliminating the temperature difference in (3.11) and (3.12)).

$$E_{th}(t) = \epsilon(\rho c)_f \text{Re}\left[T_{f0}+T_{f1}\exp(i\omega t)\right] + (1-\epsilon)(\rho c)_s \text{Re}\left[T_{s0}+T_{s1}\exp(i\omega t)\right] \tag{4.14}$$

The time averaged energy flux is given by

$$\begin{aligned} \bar{j}_{\text{th}} &= \frac{1}{\tau}\int_0^\tau j_{\text{th}}\mathrm{d}t && (4.15)\\ &= \frac{(\rho c)_f}{2} v_{s1}\text{Re}\left[T_{f1}\right] && (4.16)\\ &= \text{const.} && (4.17)\end{aligned}$$

The total energy flux must be constant in space because the net accumulated thermal energy over a cycle is zero (see equation (4.13)). The time averaged energy flux represents the portion of the flux that goes through the regenerator and is determined by the real part of the temperature oscillations only. Due to energy conservation this must also correspond to the chiller or heater power as indicated in figure (7.1). It is assumed that the regenerator and the piping are perfectly insulated such that the thermal energy Q entering on the HHEX also leaves the system on the CHEX. The time averaged energy flux through the CHEX must be equal to

the chiller cooling power.

$$Q = \frac{1}{2\pi}\int_0^{2\pi}(\rho c)_f v_s(t) A_{\text{CHEX}}\left(T_c(t) - T_c^{\text{CHEX}}(t)\right)\mathrm{d}\left(\omega t\right) \tag{4.18}$$

$$= (\rho c)_f \frac{v_{s1}}{2} A_{\text{CHEX}} \text{Re}\left[T_{c1} - T_{c1}^{\text{CHEX}}\right] \tag{4.19}$$

If both the effectiveness and the capacity rate are large enough, the temperature oscillations T_{c1}^{CHEX} will vanish and the the time average heat flux through the heat exchanger and the regenerator will be equal (note that $T_{c1} = T_{f1}$), i.e.

$$\frac{Q}{A_{\text{CHEX}}} = \bar{j}_{\text{th}} \tag{4.20}$$

This shows that the chiller or heater power must correspond to the time averaged energy flux through the regenerator.

An experimental measurement T_{f1}^{exp} is now considered. Since the instantaneous energy flux is directly proportional to the a temperature measurement, we are left to compare model predictions (equation (4.7)) against the measurement. It must be emphasised that this applies only to operating conditions where the ratio of penetration depth to solid characteristic length is larger than $1/2$

$$\delta_{th}/L_c \geq 1/2 \tag{4.21}$$

Under this condition the imaginary part of the Nusselt number becomes vanishingly small. The Nusselt number due to the time averaged energy flux is obtained by solving the real part of (4.7) for the Nusselt number, i.e.

$$\text{Nu} = \frac{\text{PrRe}_\omega \pm \text{PrRe}_\omega\sqrt{1 - 4(1+R)^2\text{Re}\left[\theta_{f1}\right]_{\text{exp}}^2}}{8(1+R)^2\text{Re}\left[\theta_{f1}\right]_{\text{exp}}} \tag{4.22}$$

Equation (4.22) comprises two solutions for the Nusselt number. Which of the two solutions is the physically reasonable is discussed in the next section. We summarize that the real part of the temperature can be related to the time averaged energy flux. In contrast to expression (4.8), the approach presented in this section only requires the real part of the temperature oscillations for the subsequent extraction of the Nusselt number.

4.3 Phase Relations and Feasible Conditions

4.3.1 Momentum Balance

A number of points must be addressed regarding the dimensionless momentum balance (3.58).

1. The dimensionless pressure gradient on the LHS is the quantity that can be measured experimentally. The second term on the RHS is equal to half of the steady state friction factor. As a result the term $-i/A_0$ must correspond to an "inertial friction factor". This means that steady state friction factors can be corrected with $-i/A_0$ to include dynamical effects. Hence we can define a total friction factor
$$\left(\frac{\mathrm{d}\hat{p}}{\mathrm{d}\xi}\right)_1 = \frac{f_D}{2} \tag{4.23}$$
where the total friction factor is given by $f_D = f^i + f^r$ with $f^i = -2i/A_0$.

2. As the dimensionless displacement amplitude increases the inertial pressure loss will become negligibly small. We can conclude that geometries with very small hydraulic diameter will show small inertial effects and can thus be treated in the quasi-steady limit, i.e. the steady state friction factor is directly applicable at any instant of time.

3. Geometries with moderate A_0 and operated at high frequency will show increased inertial effects causing a phase shift between pressure gradient and velocity. In the limit $\mathrm{Re}_\omega \to \infty$ the negative pressure gradient will lead the velocity by $\pi/2$ if the geometry is channel or pipe like ($c_2 = 0$).

4.3.2 Thermal Energy Balance

The thermal transport in regenerators is accompanied by phase relations between fluid and solid temperature oscillations, difference of temperature oscillation, velocity and interfacial heat flux. A clear understanding of these phase relations will help with interpretation of experimental data.

In this chapter the simplified thermal energy balance (4.2) and (4.3) is used. In addition the non-dimensional interfacial heat flux is defined as,

$$\hat{q}_{\mathrm{sf}} = 4\frac{\mathrm{Nu}}{\mathrm{Pr}\ \mathrm{Re}_\omega}\Delta\theta_1 = i\theta_{f1} - 1 \tag{4.24}$$

This condition arises naturally from equation (4.2). Various limits are considered to give information about the phase relation between different variables.

1. Adiabatic limit:
   In the adiabatic limit the characteristic time for heat transfer to occur is much larger than the cycle time, i.e. $\mathrm{Re}_\omega \to \infty$ and so $\hat{q}_{\mathrm{sf}} = 0$, and we are left with the condition given by

   $$i\theta_{f1} = 1 \tag{4.25}$$

   which tells us that the fluid oscillations are maximum and that convection heat transport (represented by the positive real axis with magnitude) signal is leading by $\pi/2$. Since we consider only forced convection, the velocity also leads temperature oscillations by $\pi/2$. Figure (4.2) shows the phase relation

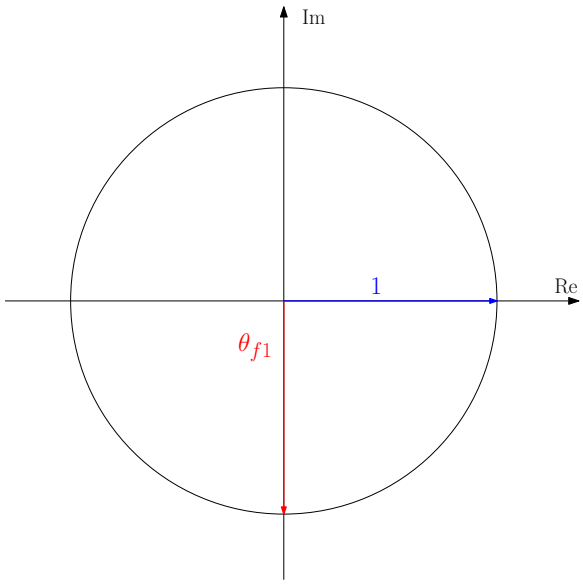

Figure 4.2: Temperature velocity phase relation in adiabatic limit

   on the complex plane. The rate of change of the thermal energy of the fluid is equal to the advectively transported energy. Due to the thermal mass of the fluid the temperature must lag the velocity by $\pi/2$.

2. Negligible thermal mass of the regenerator: $R \to \infty$
   In this limit no regeneration occurs because of the absence of packing material. Thus, this limit corresponds to oscillating flow in an empty pipe. The interfacial heat flux is, as in the adiabatic case, zero leaving us with the same condition $\theta_{f1} = -i$.

3. Negligible thermal mass of the regenerator and the fluid entrained in the pores:
   Also in this limit there is no regeneration effect. The difference to the previous case is that all temperatures are in phase with the velocity. This case is physically impossible because it would require infinite large thermal oscillation due the absence of thermal mass $\theta_{f1} \to \infty$

4. Infinite thermal mass of the regenerator:
   In this limit the temperature oscillations of the solid become vanishingly small such that $\theta_{s1} = 0$. With $(\rho c)_s \to \infty$ we also have $R \to 0$ and thus $\Delta\theta_1 = -\theta_{f1}$. Using (4.2), we are with the condition

$$\left\{ i + 4\frac{\mathrm{Nu}}{\mathrm{PrRe}_\omega} \right\} \theta_{f1} = 1 \tag{4.26}$$

The ratio $4\mathrm{Nu}/(\mathrm{PrRe}_\omega)$ is proportional to the Stanton number St and re-

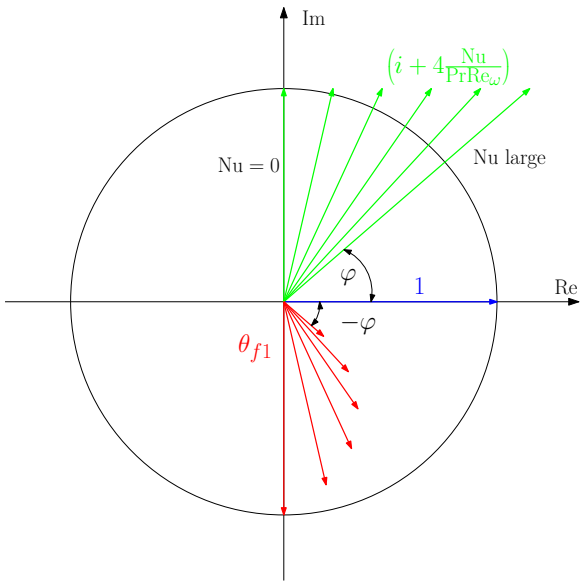

Figure 4.3: Temperature phase relation for infinite thermal regenerator mass

lates interfacial heat transfer rate to to thermal mass of the fluid. In the limit $\mathrm{Nu} \to 0$ the adiabatic operating condition is created. As Nu increases the phase difference and magnitude between velocity and temperature decreases. In the limit $\mathrm{Nu} \to \infty$ both the phase difference and the magnitude of the temperature is vanishingly small.

5. Isothermal limit $\mathrm{Re}_\omega \to 0$

   In this limit, the operation is quasi steady. The time needed for interfacial heat transfer to occur is smaller than the cycle time causing the solid and fluid temperatures to be equal $\Delta\theta_1 \to 0$. Setting equation (4.4) to zero and solving for fluid temperature gives

$$\lim_{\mathrm{Re}_\omega \to 0} \theta_{f1} = -i\frac{R}{R+1} \tag{4.27}$$

   We note that the temperature oscillations are purely imaginary and smaller than unity for any value of R.

The outcome of the above conditions (1-5) is that the phase of the temperature amplitude must be larger or equal than $-\pi/2$ and can not be larger than zero.

$$0 \geq \arg\left[\theta_{f1}\right] \geq -\pi/2 \tag{4.28}$$

4.4 Further Restrictions Due to Heat Transfer

In this section, condition (4.28) is further refined by discussing the interplay between heat transfer and thermal energy storage. Of special interest is the smallest possible phase angle between velocity and temperature (the case where velocity is in phase with temperature is physically not possible). This allows to draw an initial interpretation of a temperature measurement with respect to the model. This involves the discussion of the two different solutions for the Nusselt number from the solution of the governing equations directly (equation (4.8)) and from the instantaneous energy flux (equations (4.22)). Despite the qualitative assumption of a negligible imaginary part of the Nusselt number, equation (4.8) is discussed as a complex Nusselt number.

4.4.1 Restrictions in the Limit $R \to 0$

The minimum phase angle between velocity and fluid temperature can be determined using equation (4.8). Equation (4.8) simplifies for the case $R \to 0$ dramatically. In addition, the phase angle of the Nusselt number can be estimated without

the knowledge of operating frequency, i.e.

$$\lim_{R\to 0} \mathrm{Nu} \propto -\mathcal{E} = \frac{1}{\theta_{f1}} - i \tag{4.29}$$

The minimum phase angle can be recovered by considering the case $\mathrm{Im}\,[\mathrm{Nu}] = 0$.

$$\begin{aligned} \mathrm{Im}\left[-i + \frac{1}{|\theta_{f1}|}\exp\left(-i\arg\left[\theta_{f1}\right]\right)\right] &= 0 \\ \sin\left(\arg\left[\theta_{f1}\right]\right) &= -|\theta_{f1}| \end{aligned} \tag{4.30}$$

Using $\sin\left(\arg\left[\theta_{f1}\right]\right) = \mathrm{Im}\left[\theta_{f1}\right]/|\theta_{f1}|$, we have

$$\begin{aligned} \mathrm{Im}\left[\theta_{f1}\right] &= -|\theta_{f1}|^2 \\ \mathrm{Im}\left[\theta_{f1}\right] &= -\left[\mathrm{Re}\left[\theta_{f1}\right]^2 + \mathrm{Im}\left[\theta_{f1}\right]^2\right] \\ \mathrm{Re}\left[\theta_{f1}\right] &= \pm\sqrt{-\mathrm{Im}\left[\theta_{f1}\right] - \mathrm{Im}\left[\theta_{f1}\right]^2} \end{aligned} \tag{4.31}$$

Real solutions of this last equation, for $\mathrm{Im}\left[\theta_{f1}\right] < 0$ build a circle centred on $(0, i1/2)$. As shown in figure (4.4) the region enclosed with this circle and the curve $\arg\left[\theta_{f1}\right] = -\pi/2$ (adiabatic limit) forms the target region where possible measurements could be located whenever $R = 0$.

4.4.2 Extension to Arbitrary Value of R

In the previous section a target region for temperature amplitude measurements in the limit $R \to 0$ is constructed. This can also be done for arbitrary R by just mapping out Nu given any phase angle of Nu. This can be done by calculating the phase angle of (4.8) without taking any operating conditions into account, i.e.

$$\arg\left[\mathrm{Nu}\right] = \arg\left[\frac{\mathcal{E}}{iR\mathcal{E} - 1}\right] = \varphi \tag{4.32}$$

Hence, a contour line can be drawn for any possible value of φ. The region for which both imaginary and real part of the Nusselt number are positive is characterized by phase angles of Nu between 0 and 90°, i.e. $0 \leq \varphi \leq \pi/2$. Two sample plots are given below with $R = 0.25$ (figure (4.5)) and $R = 1$ (figure (4.6)). It can be seen that the target region for temperature amplitude measurements becomes smaller as R increases. This is indeed consistent since in the case $R \to \infty$, the target

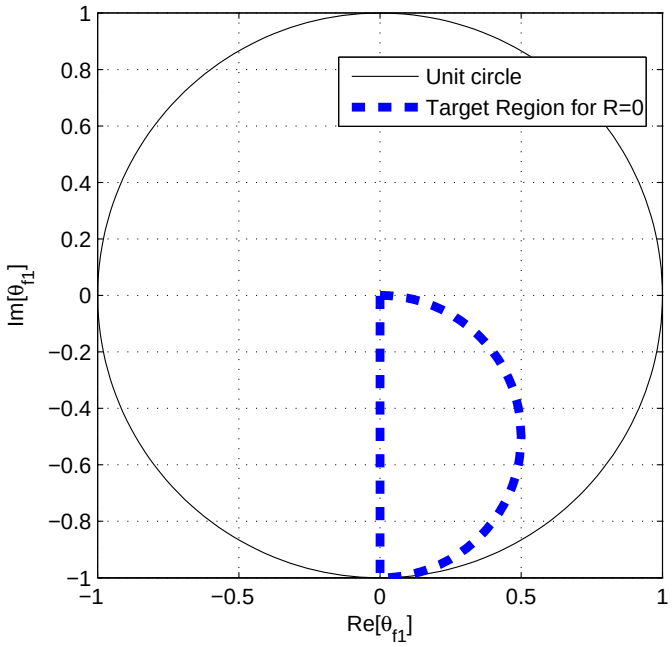

Figure 4.4: Region for possible temperature amplitude measurements

region will vanish, indicating that no measurements will be meaningful since the regenerator operates in a limit where no regeneration is possible.

4.4.3 Restrictions for Nusselt Number from Time Averaged Energy Flux

So far, only the Nusselt number obtained directly from the solution of the governing equations (4.8) has been discussed. Also the Nusselt numbers from the instantaneous energy flux can be used to derive restrictions.

The Nusselt number from time averaged energy flux (positive solution equation (4.22)) is from a mathematical point of view a complex number whenever

$$\mathrm{Re}\left[\theta_{f1}\right] > \frac{1}{2\left(1+R\right)} \tag{4.33}$$

On the other hand, Nu_R is purely real whenever

$$\mathrm{Re}\left[\theta_{f1}\right] \leq \frac{1}{2\left(1+R\right)} \tag{4.34}$$

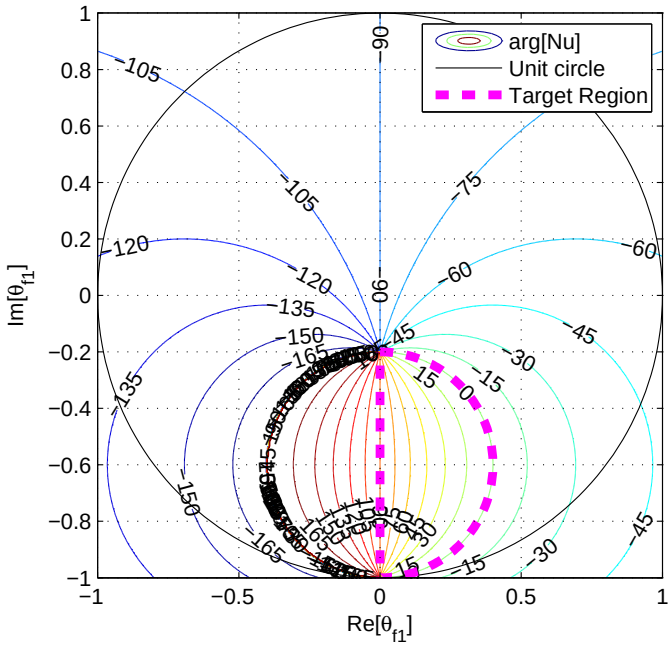

Figure 4.5: Target region for $R = 0.25$

It must be stressed that the Nusselt number is derived from the time averaged energy flux. Therefore, no quantitative conclusion can be made about the dynamics of the heat transfer. Put differently, it is not possible to calculate the thermal reactance of the interfacial heat transfer if only the time averaged energy flux is known. Mathematically, this means that the Nusselt number cannot be complex and the real part of temperature is restricted by condition (4.34). It is interesting to note, that the Nusselt number from the direct solution share the condition given by (4.34) as illustrated in figure (4.7). The derivation of the extreme values for temperature are discussed in Appendix (C). The half circle in figure (4.7) corresponds to the case where $\mathrm{Im}\,[\mathrm{Nu}] = \arg\,[\mathrm{Nu}] = 0$. The largest value of real part of temperature falls together with condition (4.34). All measured temperatures must coincide with the dashed half circle shown in figure (4.7) if the direct solution is used to extract the Nusselt number under the assumption of a vanishingly small imaginary part of the Nusselt number. The region where measured temperatures are meaningful is less restrictive if the Nusselt number based on time averaged heat transfer coefficient is used to extract the Nusselt number. The restriction is characterize by the red box in figure (4.7) indicating that all measurements must be located within this red box.

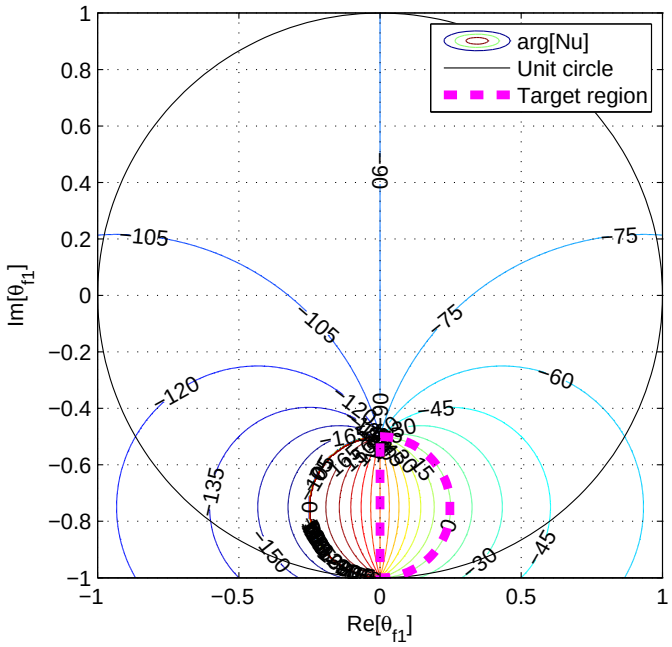

Figure 4.6: Target region for $R = 1$

This chapter determines the maximum and minimum phase angles of the temperature in the complex plane. An experimentally measured temperature θ_{f1} can be compared to the target region which allows to draw initial conclusion about the experiment with respect to the model assumptions. There are still two possible ways to calculate a Nusselt number from an experiment. These expressions (4.8) and (4.22) can be validated against pore scale simulations to explore conditions where the two expressions hold.

4.5 Restrictions for Nusselt Number from Time Averaged Energy Flux

The Nusselt number obtained from the time averaged energy flux (4.22) yields two solutions. From the discussion in section (4.3.2) it can be concluded that the temperature is purely imaginary in the isothermal limit $\mathrm{Re}_\omega \to 0$ and in the adiabatic limit $\mathrm{Re}_\omega \to \infty$. However, the latter assumes the Nusselt number to be a constant

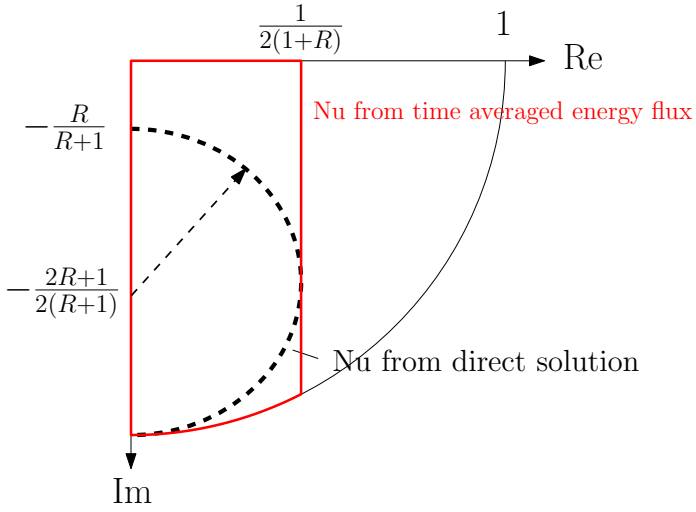

Figure 4.7: Target region using direct Nusselt number (4.8) compared to target region using time averaged energy flux formulation (4.22)

independent of Re_ω.

$$\lim_{\mathrm{Re}[\theta_{f1}]\to 0} \mathrm{Nu}_{R+} = \infty \tag{4.35}$$

$$\lim_{\mathrm{Re}[\theta_{f1}]\to 0} \mathrm{Nu}_{R-} = 0 \tag{4.36}$$

In the low frequency range the interfacial heat transfer will be large. Hence the positive solution Nu_{R+} must be the physically relevant in the low frequency limit. It can be expected that the Nusselt number is a function of Re_ω because it determines the thickness of momentum and thermal boundary layer. Therefore, no general assumption of the case $\mathrm{Re}_\omega \to \infty$ in the non-adiabatic limit can be made since the specific functional form of the Nusselt number is unknown and will depend on the geometry and operating condition.

Chapter 5

Microscopic Transport Equations and Virtual Experiments

5.1 Repetitive Elementary Volume

In previous sections macroscopic balance equations were used to find an expression for the Nusselt number for a given set of experimental data. In this section the balance equations are considered on the pore scale (i.e. microscopic scale) to calculate the Nusselt number. The computational domain is limited to a representative elementary volume (REV). The REV approach has been used by many researchers to calculate macroscopic transport quantities in porous media like effective thermal conductivity, interfacial heat transfer, friction factor etc. The benefit of this approach is that these transport quantities can be calculated on a theoretical basis. All these effective transport properties are obtained by post processing the numerical solution on a REV, i.e. they don't appear directly in the transport equations. The results obtained from the REV approach can be compared to the macroscopic theory and experimentally obtained Nusselt numbers.

A microchannel geometry is well suited to perform virtual experiments on a representative elementary volume (REV) as shown in figure (5.1). The picture on the left hand side shows the micro channel regenerator. The center picture represents a 3D REV with surrounding solid. The last picture is a 2D front face version of the previous 3D full REV. This approach also has a practical aspect: any potential regenerator geometry can be virtually tested before it is produced for experimental testing.

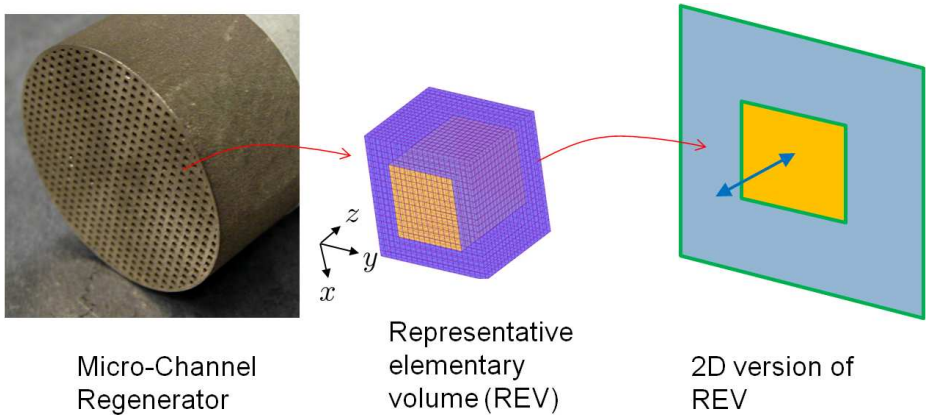

Figure 5.1: Extraction of a representative elementary volume (REV)

5.2 Governing Equations for Representative Elementary Volume

5.2.1 Momentum Balance

The microscopic models are given by equations (A.2) and (A.3). In order to resolve flow and temperature accurately a 3D representation of a single channel is needed as shown in figure (5.1). The momentum balance (A.2) in terms of dimensionless quantities is [17]

$$\mathrm{Re}_\omega \frac{\partial \hat{\boldsymbol{v}}}{\partial \hat{t}} + \mathrm{Re}_{dh} \hat{\boldsymbol{v}} \hat{\nabla} \hat{\boldsymbol{v}} = -\mathrm{Re}_{dh} \hat{\nabla} \hat{p} + \hat{\nabla}^2 \hat{\boldsymbol{v}} \tag{5.1}$$

where the same dimensionless numbers as presented in section (3.6) are used. Alternatively, the above equation can be written in terms of dimensionless displacement amplitude A_0 and dynamic Reynolds number Re_ω

$$\frac{\partial \hat{\boldsymbol{v}}}{\partial \hat{t}} + A_0 \hat{\boldsymbol{v}} \hat{\nabla} \hat{\boldsymbol{v}} = -A_0 \hat{\nabla} \hat{p} + \frac{1}{\mathrm{Re}_\omega} \hat{\nabla}^2 \hat{\boldsymbol{v}} \tag{5.2}$$

Since the flow is oscillating, the same harmonic approximation technique is applied as it was done for the macroscopic momentum energy balance. This has the advantage that the time integration can be dropped completely. However, using complex notation will double the number of unknowns (real and imaginary part of all intensive variables). The third dimension can also be dropped in every kind of channel flow (when entrance effects are ignored) such that there will be only a non-zero axial velocity component $\hat{\boldsymbol{v}} = (0, 0, \hat{v}_z)^T$ as shown in the right picture of

figure (5.1). The harmonic approximation of $\hat{v}_z$ is

$$\hat{v}_z = \hat{v}_{z1} \exp\left(i\hat{t}\right) \tag{5.3}$$

where $\hat{v}_{z1} = \hat{v}_{z1}(x, y) \in \mathbb{C}$ is a complex number indicating magnitude and phase in space. The momentum balance in the harmonic approximation and for axial flow is given by

$$i\hat{v}_{z1} = -A_0 \frac{\mathrm{d}\hat{p}}{\mathrm{d}\zeta} + \frac{1}{\mathrm{Re}_\omega} \hat{\nabla}^2 \hat{v}_{z1} \tag{5.4}$$

where ($\zeta = z/d_h$) is the nondimensional direction into the plane. The problem is now scalar for the flow which points out of the plane. In fact, (5.4) describes two equations, one for the real and one for the imaginary part. Equation (5.4) is completed with a no slip boundary condition for all times $\hat{t}$, i.e. $\hat{v}_{z1} = 0$ on $\partial\Omega_f$.

5.2.2 Thermal Energy Balance

The thermal energy balance is solved on Ω_r. The thermal balance equation at microscopic level is given by (A.3). This time the harmonic approximation is applied right away because the fluid temperature consists of mean value and first order oscillation

$$T = T_0 + T_1 \exp\left(i\omega t\right) \tag{5.5}$$

The time averaged energy balance reduces to

$$\nabla^2 T_0 = 0 \tag{5.6}$$

To ensure periodicity, the heat flux at the outside solid boundary is assumed to be zero, i.e. $\nabla T = 0$ on $\partial\Omega_s$. Hence the time averaged temperature must be equal to a constant because no energy is entering the domain on an averaged basis, i.e. T_0 =const.

For the first order temperature oscillations, equations (5.5) and (A.3) give

$$\left(\rho c\right)_f i\omega T_1 = -\left(\rho c\right)_f v_{z1} \frac{\mathrm{d}T_0}{\mathrm{d}z} + \kappa_f \nabla^2 T_1 \tag{5.7}$$

Note that $\mathrm{d}T_0/\mathrm{d}z$ =const. and can be chosen arbitrarily in form of external excitation of the system (just as the pressure gradient for the momentum balance). The

advective term is zero on Ω_s. Using the groupings $A_0, \mathrm{Re}_\omega, \mathrm{Pr}$ and dimensionless temperature θ_1, this can be rewritten as

$$i\theta_1 = \hat{v}_{z1} + \frac{1}{\mathrm{PrRe}_\omega}\hat{\nabla}^2\theta_1 \tag{5.8}$$

$$i\theta_1 = \mathrm{Fo}\left(\frac{l_c}{d_h}\right)^2\hat{\nabla}^2\theta_1 \tag{5.9}$$

Note that the two equations are structurally the same whenever $\hat{v}_{z1} = 0$. The second equation is written down because it is customary to use the Fourier number Fo for solid materials. Also this equation is completed with a symmetry boundary condition on the solid outside walls, i.e. $\nabla\theta_1 = 0$ on $\partial\Omega_r$.

5.3 Post Processing and Parameter Extraction

Once the solution is known, the Nusselt number can be calculated in a post processing step. The Nusselt number is given by $\mathrm{Nu} = h{\cdot}d_h/\kappa_f$ with $h = Q_{\mathrm{sf}}/A_{\mathrm{sf}}/(\langle T\rangle^f - \langle T\rangle^s)$. Where Q_{sf} is the interfacial heat flux

$$\begin{aligned}\frac{Q_{\mathrm{sf}}}{A_{\mathrm{sf}}} &= \frac{\int_{\partial\Omega_f} -\kappa_f\nabla T\mathrm{d}\boldsymbol{S}}{\int_{\partial\Omega_f}\mathrm{d}\boldsymbol{S}} \\ &= \frac{\kappa_f}{d_h}A_0\frac{\mathrm{d}T_0}{\mathrm{d}\zeta}\frac{\int_{\partial\Omega_f}\hat{\nabla}\theta_1\mathrm{d}\boldsymbol{S}}{\int_{\partial\Omega_f}\mathrm{d}\boldsymbol{S}}\end{aligned} \tag{5.10}$$

The temperature difference can be written as

$$\langle T\rangle^f - \langle T\rangle^s = T_0 + \langle T_1\rangle^f - (T_0 + \langle T_1\rangle^s) = -A_0\mathrm{d}T_0/\mathrm{d}\zeta\left(\langle\theta_1\rangle^f - \langle\theta_1\rangle^s\right) \tag{5.11}$$

where the local average of the temperature amplitude in the fluid is obtained by integrating the temperature amplitudes over the channel cross sectional area divided by the cross sectional area

$$\langle\theta_1\rangle^k = \frac{\int_{\Omega_k}\theta_1\mathrm{d}A}{\int_{\Omega_k}\mathrm{d}A} \qquad k = \{f, s\} \tag{5.12}$$

Table 5.1: Coefficient listing for momentum and thermal energy balance

Balance	$\psi \in \mathbb{C}$	K	M
Momentum	$\hat{\boldsymbol{v}} = (0, 0, \hat{v}_{z1})^T$	$A_0 \mathrm{Re}_\omega \mathrm{d}\hat{p}/\mathrm{d}\zeta$	Re_ω
Th. Energy	θ_1	$-\hat{v}_{z1}\mathrm{PrRe}_\omega$	PrRe_ω

Hence the Nusselt number can be calculated from

$$\mathrm{Nu} = -\frac{1}{\langle\theta\rangle^f - \langle\theta\rangle^s} \frac{\int_{\partial\Omega_f} \hat{\nabla}\theta_1 \mathrm{d}\boldsymbol{S}}{\int_{\partial\Omega_f} \mathrm{d}\boldsymbol{S}} = -\frac{\left\langle \hat{\nabla}\theta_1 \right\rangle_{\boldsymbol{S}}}{\langle\theta_1\rangle^f - \langle\theta_1\rangle^s} \tag{5.13}$$

Where $\langle\bullet\rangle_{\boldsymbol{S}}$ denotes an area average.

5.3.1 Similarity Between Momentum and Thermal Energy Balance

Both, momentum and thermal energy balance have the same mathematical structure which is referred to as Reynolds analogy. The equation that governs momentum and thermal energy transport in oscillating flow reads

$$\left[iM - \hat{\nabla}^2\right] \psi = -K \tag{5.14}$$

The coefficients are in general complex and take different values depending on what field we are aiming to solve for as shown table (5.1). Many commercial software products do not support harmonic versions of the momentum balance as represented by equation (5.14). However, the generic form (5.14) can also be understood as a special form of the Maxwell equations, whenever electromagnetic induction is present on 2D domains, $\nabla \times \boldsymbol{E} = -\partial_t \boldsymbol{B}$ with $\boldsymbol{B} = \nabla \times \boldsymbol{A}$ a scalar equation for the magnetic vector potential $\boldsymbol{A} = (0, 0, A_z)^T$ is obtained [27]

$$-\mu^{-1}\nabla^2 A_z + i\omega\sigma A_z = J_{0z} \tag{5.15}$$

This equation is often used for eddy current analysis. Given the similarity of this equation with (5.14), we can use the electrodynamics kernel to calculate oscillating flow in any channel by substituting A_z with v_{z1} or θ_1. It is well known that in alternating current, the harmonic magnetic field generates eddy currents opposing the driving current J_{0z}, causing the resulting current $J_z = J_{0z} - iw\sigma A_z$ to flow in

a thin layer at the surface of the wire. A similar phenomenon is observed with oscillating flow, as the frequency increases, the strong change in velocity (inertial effect) will induce pressure gradients opposing the driving pressure gradient applied from outside the system. As a result the flow will be peaking close to the wall if the frequency is very large. At the same time the temporal evolution of pressure gradient will not be in phase with the velocity. In the limit of a very high frequency, the global velocity will be lagging the pressure gradient by $\pi/2$. At low frequency, the flow can be approximated by Hagen-Poiseuille type parabolic distribution and the phase difference between velocity and pressure gradient will be minimal [8] (quasy steady flow).

In Appendix (B) the general balance equation (5.14) is considered on a circular tube geometry. For this geometry analytical solutions exists for flow field and Nusselt number. Numerical solutions can then be validated against the analytical solution for this circular tube geometry. It can be seen that analytical and numerical solution are in fair agreement (Appendix (B)). Based on the satisfactory results using the numerical solver, the microchannel geometry is numerically analyzed in the following section.

5.4 Boundary Layer Thickness and Nusselt Number Approximation

This section covers the sensitivity analysis of the Nusselt number in terms of the independent parameters Pr, Re_ω, Fo. A solution of equations (5.8) and (5.9) must be initialized using values of the parameters Pr, Re_ω and $\mathrm{Re}_\omega\mathrm{Fo}$. The ratio l_c/d_h is held constant with reference to a micro channel with ($l_c = 0.5$mm, $d_h = 0.7$mm) indicating constant porosity of $\epsilon = 0.346$. Given the above parameters, the Nusselt number can be discussed in terms of the thermal mass ratio and the thermal conductivity ratio using the identity (3.54)

$$\frac{R}{\gamma_k} = \left(\frac{l_c}{4d_h}\right)\mathrm{PrRe}_\omega\mathrm{Fo} \tag{5.16}$$

The right hand side of equation (5.16) represents the parameter used to initialize a simulation. The left hand side describes the ratio of the thermal diffusivities of the two domains. This ratio is split up in thermal mass ratio R and thermal

conductivity ratio γ_k to relate it to the macroscopic expressions for Nusselt number.

The parameters Pr, Re_ω, Fo can be used to estimate hydrodynamic and thermal boundary layers. The boundary layers in a porous media develop in each pore [20]. The flow is considered to be fully developed at the center region of the regenerator. The hydrodynamic boundary layer in oscillating flow is proportional to the expression [28]

$$\frac{\delta_{\mathrm{hyd}}}{d_h} \sim \frac{1}{\sqrt{\mathrm{Re}_\omega}} \tag{5.17}$$

The Prandtl number describes the ratio of hydrodynamic boundary layer and thermal boundary layer, therefore the thermal boundary layer is proportional of the inverse square root of Prandtl and Reynolds number product [28]

$$\frac{\delta^f_{\mathrm{th}}}{d_h} \sim \frac{1}{\sqrt{\mathrm{PrRe}_\omega}} \tag{5.18}$$

The thermal penetration depth into the solid is already introduced in chapter (4), equation (4.10). In terms of Fourier number, the relative penetration depth reads

$$\frac{\delta^s_{\mathrm{th}}}{l_c} \sim \sqrt{\mathrm{Fo}} \tag{5.19}$$

The ratio of the penetration depth and the fluid thermal boundary layer gives

$$\frac{\delta^s_{\mathrm{th}}}{\delta^f_{\mathrm{th}}} \sim \frac{l_c}{d_h}\sqrt{\mathrm{PrRe}_\omega \mathrm{Fo}} \tag{5.20}$$

$$\sim 2\sqrt{\frac{l_c}{d_h}\frac{R}{\gamma_k}} \tag{5.21}$$

$$\sim \sqrt{\frac{\alpha_s}{\alpha_f}} \tag{5.22}$$

It is concluded that the above ratio depends essentially on the thermal diffusivity ratio. It can be seen that the ratio $\delta^s_{\mathrm{th}}/\delta^f_{\mathrm{th}}$ increases with increasing thermal mass and decreasing conductivity ratio. For $R \to 0$, there are no temperature oscillations in the solid, indicating zero penetration depth as illustrated in figure (5.2). In addition, the temperature distribution at the interface is qualitatively shown in figure (5.2) for a finite value of R at fixed Pr and Re_ω (δ^f_{th} =const.). Temperature and heat flux must be continuous at the interface. In general the temperature oscillations damp out as the distance from the wall into the solid increases as shown for

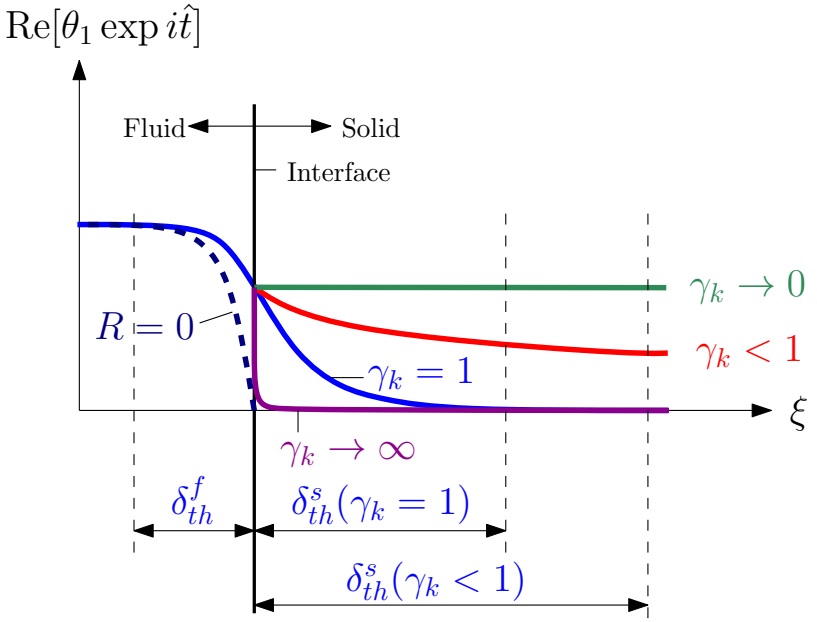

Figure 5.2: Temperature distribution at the fluid solid interface

the case $\gamma_k = 1$. If γ_k decreases, the penetration depth increases such that the solid temperature will oscillate with time. If the solid thermal conductivity is infinite (and $\gamma_k \to 0$) the penetration depth goes to infinity causing uniform temperature oscillations in the solid at a magnitude equal to the temperature at the interface. The solid acts as an insulator that damps out temperature oscillations as the solid thermal conductivity goes to zero ($\gamma_k \to \infty$).

The Nusselt number can be qualitatively discussed in terms of bulk temperature difference and boundary layer thickness. The Nusselt number can be approximated from (5.13) as

$$\mathrm{Nu} \;=\; -\frac{1}{\langle\theta_1\rangle^f - \langle\theta_1\rangle^s}\frac{\mathrm{d}\theta_1}{\mathrm{d}\xi}\bigg|_{\xi=\partial\Omega_{sf}} \tag{5.23}$$

The gradient at the interface can be approximated using the boundary layer thickness

$$\frac{\mathrm{d}\theta_1}{\mathrm{d}\xi}\bigg|_{\xi=\partial\Omega_{sf}} \approx \frac{\langle\theta_1\rangle^s - \langle\theta_1\rangle^f}{\delta^s_{\mathrm{th}}/d_h + \delta^f_{\mathrm{th}}/d_h} \tag{5.24}$$

Hence, the Nusselt number can be approximated as the inverse sum of boundary

layer thickness and penetration depth

$$\mathrm{Nu} \approx \frac{d_h}{\delta^s_{\mathrm{th}} + \delta^f_{\mathrm{th}}} \tag{5.25}$$

It can be concluded that both the thermal boundary layer thickness and the penetration depth need to be small in order to get a large Nusselt number. Thus it can be concluded that a high thermal mass of the solid $(R \to 0)$, or a small thermal conductivity of the solid $(\gamma_k \to \infty)$ will result in larger Nusselt numbers, compared to the case where R and γ_k are finite. The temperature of the solid will respond faster if the thermal conductivity of the material is high and the heat capacity low. As a result, the bulk mean temperature difference will be smaller as compared to the case where $R = 0$ and $\gamma_k \to \infty$. Therefore, the temperature gradient at the interface decreases, resulting in a smaller interfacial heat flux as in the case $R = 0$, and $\gamma_k \to \infty$.

5.5 Virtual Experiments

5.5.1 Sample Run

The general balance equation for momentum and thermal energy (5.14) is solved on a rectangular channel that presents a single channel of the entire regenerator geometry. The flow and temperature field is solved using parameters in the range that represent typical operating conditions of the regenerator, e.g. $\mathrm{Re}_\omega = 5,\ A_0 = 99,\ \mathrm{Pr} = 7, \mathrm{Fo} = 0.06,\ \mathrm{d}\hat{p}/\mathrm{d}\zeta = -0.25$. The solution has been calculated using $N_{\mathrm{FE}} = 25600$ finite elements and $N_{\mathrm{DOF}} = 51842$ degrees of freedom using linear shape functions. The number of elements is kept high in order to resolve the heat flux across the boundary $\partial\Omega_{sf}$ accurately. The almost doubled number of degrees of freedom results from the fact that one must solve real and imaginary part of either velocity or temperature field. The time needed to calculate one of the fields with above specifications is less than 3 seconds. A corresponding fully transient calculation brings not only the drawback of higher computation time but also an additional effort to extract and process transient data to calculate a time dependent Nusselt number.

Figures (5.3) and (5.4) show real and imaginary part of the dimensionless velocity. The real and imaginary part of dimensionless temperature are shown in

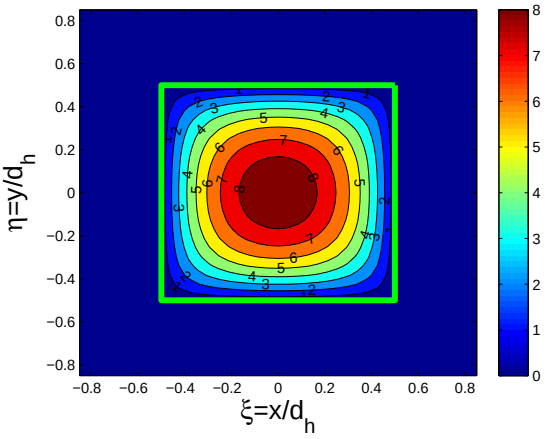

Figure 5.3: Re $[\hat{v}_{z1}]$

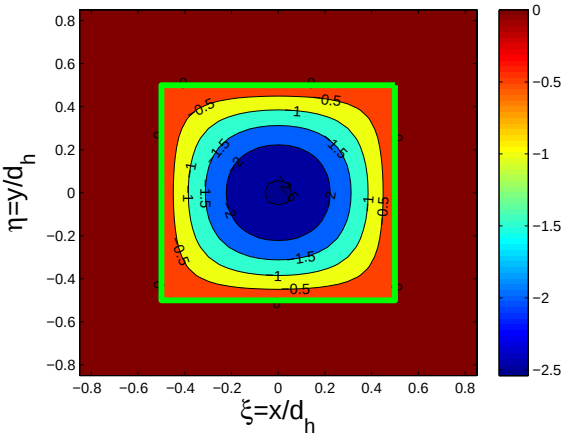

Figure 5.4: Im $[\hat{v}_{z1}]$

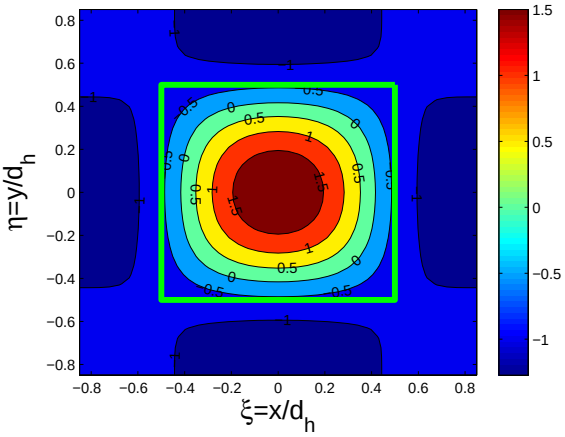

Figure 5.5: Re $[\theta]$

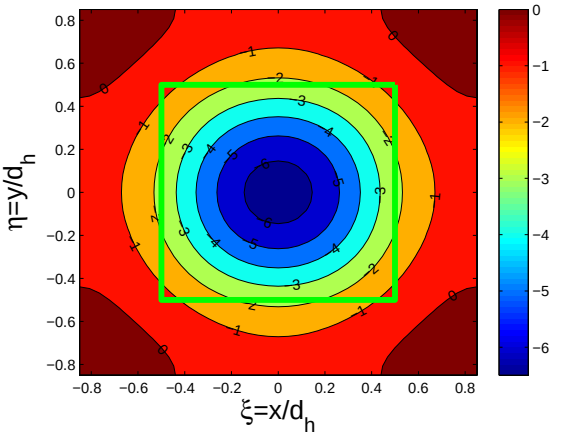

Figure 5.6: Im $[\theta]$

figures (5.5) and (5.6). A parabolic type velocity profile can be observed for both real and imaginary part of dimensionless velocity. This can be expected at low kinetic Reynolds numbers [29]. It can be seen that the imaginary part is negative and approximately one order of magnitude smaller than the real part. The imaginary part of the velocity is a direct indication of the magnitude of inertial forces in the system. Due to the negative imaginary part of dimensionless velocity, it can be concluded that the negative pressure gradient is leading the velocity by a small phase angle given by the ratio of imaginary and real part of the velocity. In turn, the temperature oscillations have larger imaginary parts than real parts. Since the imaginary parts are negative and the positive real parts are small on the fluid domain, it can be concluded that the fluid temperature oscillations lag behind the

velocity by a phase angle smaller than $\pi/2$. However, this is not the case for the solid temperature oscillations which show negative real part, indicating that the solid temperature lags behind the fluid temperature. In terms of magnitude, it can be concluded that the solid phase oscillations are damped compared to the fluid oscillations.

5.5.2 Sensitivity of Nusselt Number

The dependency of the Nusselt number on operating condition and material properties is of particular interest for the thermal design of a regenerator. The dependency of the Nusselt number as a function of Pr, Re_ω, R and γ_k is discussed qualitatively in section (5.4). In this section the Nusselt number is discussed on a quantitative basis using numerical analysis presented in the previous section for different operating conditions and material properties. The real and imaginary part of the Nusselt number are shown in figures (5.7) and (5.8), respectively.

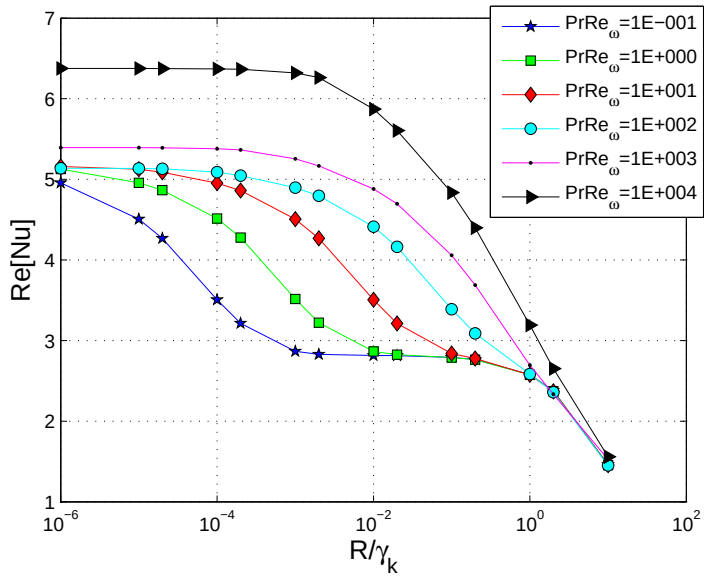

Figure 5.7: Real part of Nusselt number as a function of thermal diffusivity ratio R/γ_k

The different curve sets correspond to variations of the parameter PrRe_ω. First, the case $\gamma_k = 1$ is discussed in order to allow only variations in thermal mass ratio R. In general the Nusselt number increases with PrRe_ω because both bulk temperature difference and interfacial heat flux increase with this grouping. However,

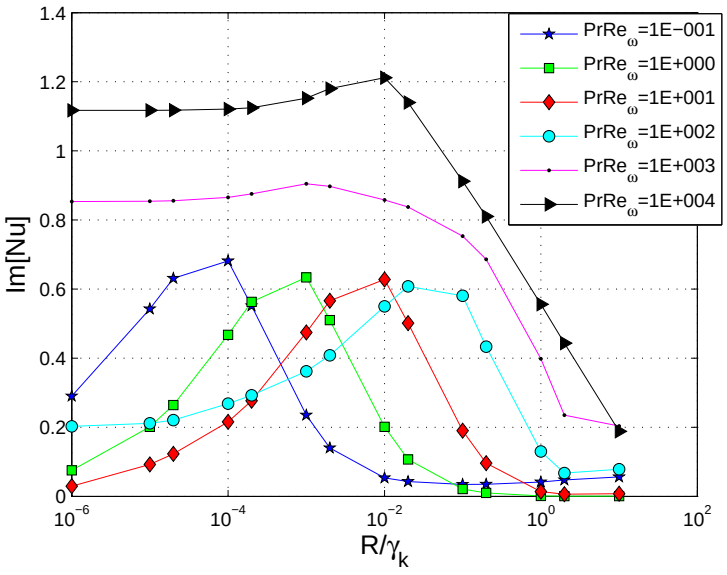

Figure 5.8: Imaginary part of Nusselt number as a function of thermal diffusivity ratio R/γ_k

the sensitivity to Re_ω is pronounced for $R \in [10^{-2}, 10^{0}]$ and less pronounced in the limit $R \to 0$. It is clear that the Nusselt number must go to zero as R increases because in the limit $R \to \infty$, all fluid temperature oscillations will vanish and no heat transfer can occur. For $R \to 0$ the temperature difference reaches its maximum value of $\langle \theta_{f1} \rangle^f = 1$ as Re_ω increases. The interfacial heat flux is less sensitive to increments of Re_ω (thermal boundary layer decreases with square root of PrRe_ω) whenever $R = 0$. The situation for $R \in [10^{-2}, 10^{0}]$ is more sensitive to incremental changes of PrRe_ω because the temperature difference $\langle \theta_{s1} \rangle^s - \langle \theta_{f1} \rangle^f$ will increase with Re_ω causing a larger heat flux at the interface increasing the Nusselt number with larger increments than in the case $R \to 0$. If the thermal conductivity ratio is smaller than unity $\gamma_k < 1$, the Nusselt number will decrease as it is discussed qualitatively in section (5.4) because the penetration depth increases, causing a reduced bulk temperature difference.

The imaginary part of the Nusselt number is shown as a function of the thermal diffusivity ratio R/γ_k in figure (5.8). At $R = 0.1$ the imaginary parts of the Nusselt number increase with frequency indicating that the solids larger thermal mass causes a temporally delayed absorption of the energy supplied at the interface. For $\mathrm{PrRe}_\omega \in [10^{-1}, 10^{1}]$, $\mathrm{Im}\,[\mathrm{Nu}]$ show maximum imaginary parts at different values for R and then drop as $R \to 0$. Interestingly, the imaginary parts for

$\mathrm{PrRe}_\omega = 10^2$ show large imaginary parts even if $R \to 0$. The presence of an imaginary part corresponds in general to the situation of non proportionality of heat flux and bulk mean temperature. This implies that there must be a situation where the bulk mean temperature difference is zero but with non zero interfacial heat flux. An increase in solid thermal conductivity γ_k causes a decrease in the imaginary part of the Nusselt number because the thermal penetration depth increased therefore decreasing the response time of solid material.

5.5.3 Comparison of Macroscopic and Microscopic Approach

The Nusselt number can be extracted experimentally by simply evaluating the two expressions for the Nusselt number given by equation (4.8), (4.22). In turn the Nusselt number obtained using the 2D model results by building the ratio of interfacial heat transfer rate and bulk mean temperature difference as shown in the last section. The temperature oscillations calculated by the 2D model can

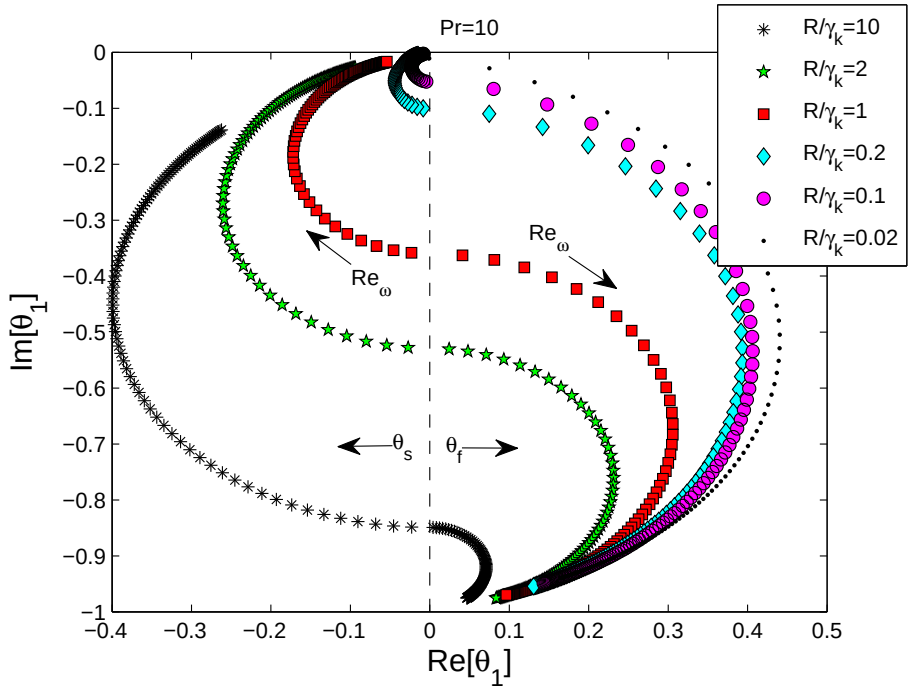

Figure 5.9: Temperature amplitudes obtained from 2D numerical model for $\mathrm{Pr} = 10$

be used to evaluate the macroscopic expressions for the Nusselt number (4.8) and (4.22). The Nusselt numbers obtained from macroscopic and microscopic theory

can then be compared to identify physical limits where the two models line up. Figure (5.9) shows the volume averaged temperature amplitudes calculated using the 2D model for $\mathrm{Pr} = 10$ (solid in third quadrant and fluid in fourth quadrant of the complex plane). The fluid temperature amplitude increases with Re_ω while the solid temperature amplitude decrease with Re_ω for fixed R/γ_k therefore maximizing the temperature difference as $\mathrm{Re}_\omega \to \infty$. The fluid amplitude range increases as $R/\gamma_k \to 0$ which has been already discussed using the macroscopic transport equations (see (4.7)).

The volume averaged temperature amplitudes shown in figure (5.9) are used to evaluate the macroscopic expression for the Nusselt number (4.8) and (4.22). The relative error between the macro and micro Nusselt number is defined as

$$\text{Error} = \frac{\mathrm{Nu}_{\text{micro}} - \mathrm{Nu}_{\text{macro}}}{\mathrm{Nu}_{\text{micro}}} \tag{5.26}$$

where $\mathrm{Nu}_{\text{micro}}$ and $\mathrm{Nu}_{\text{macro}}$ are the Nusselt number obtained from the 2D model directly and the evaluated expression (4.8) and (4.22), respectively. Figure (5.10)

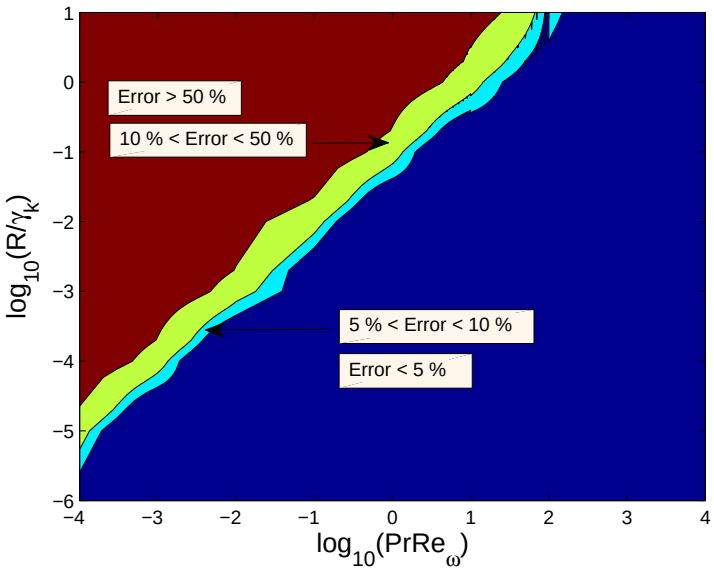

Figure 5.10: Error between microscopic and macroscopic calculation of the Nusselt number (from direct solution (4.8))

shows the relative error between microscopic and macroscopically evaluated Nusselt number from the direct solution (4.8). The error is less than 5% for all PrRe_ω combination if the thermal mass ratio goes to zero $R \to 0$. As the thermal mass

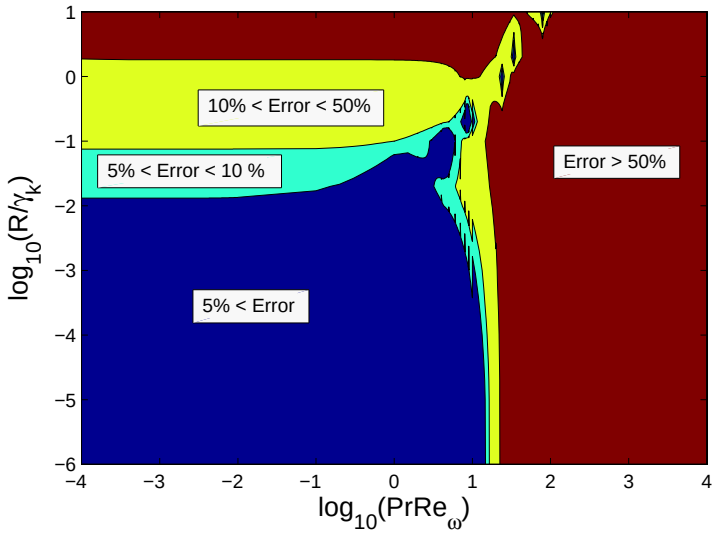

Figure 5.11: Error between microscopic and macroscopic calculation of the Nusselt number (from time averaged heat flux (4.22))

ratio increases, a high PrRe_ω is needed to keep the error low (i.e. for water, the frequency needs to be high). The reason for this lies in the fact that the macroscopic model does not take diffusion effects into account. In the limits of $R \to 0$ or $\mathrm{PrRe}_\omega \to \infty$ the solid temperature oscillation will be damped out completely and thus lining up with the macroscopic model. On the other hand, the temperature oscillations in the solid can be uniform at $R \neq 0$ if $\gamma_k \to \infty$. The penetration depth expands then to infinity such that temperature oscillations in the solid will be equal to the temperature oscillations at the interface. However, this state is independent of the thermal mass and can thus not line up with the macroscopic model.

Figure (5.11) shows the relative error between microscopic and macroscopically evaluated Nusselt number derived from the time averaged heat flux (4.22). For $R/\gamma_k < 0.1$ the errors are smaller than 10% if the PrRe_ω combination is small which implies that thermal conductivity of the fluid must be large in radial direction. If the solid thermal conductivity is equally large the thermal diffusivity ratio will approximate the thermal mass ratio $R/\gamma_k \approx R$. This represents essentially the condition under which the Schuman model is based on, that is, infinite radial thermal conductivity in the regenerator bed. The Nusselt number based on the direct solution (4.22) does not reflect this feature.

It can be concluded that the two models line up based on the interpretation of

the macroscopic balance equations. In figure (5.10) the macroscopic balance equation is understood to hold in radial direction, just as the 2D model. Thus the macroscopic model lines only up under conditions where the lateral diffusion terms are small (large Pr and small Fo). If the Nusselt number based on time averaged heat flux is used the macroscopic balance equation must be understood to hold in axial direction. Then the model lines up if lateral diffusion terms are large (small Pr and large Fo).

Chapter 6

Summary and Key Findings for Part I - Model Development and Validation

6.1 Macroscopic Balance Equations

The work reported in part 1 of this thesis describes a theoretical procedure to extract friction factor and Nusselt number from an experiment. The goal is to come up with a simple and clear procedure to estimate the Nusselt number. The expressions derived for the Nusselt number can be applied to experimental data if the spectral composition up to first order is known. The expressions for Nusselt number hold under the following assumptions

1. Simple harmonic representation of pressure, velocity and temperature.
2. Constant time averaged temperature gradient.
3. Infinite thermal conductivity in the radial bed direction.
4. Negligible thermal conductivity in the axial direction.
5. No ambient heat losses

Under these assumptions the Nusselt number (4.8) can be directly calculated from the solution for temperature of the thermal mass balance. It is observed, that the Nusselt number is in general a complex number. However, this stands in contradiction with the initial assumption of an infinite thermal conductivity, in radial direction causing a large penetration depth into the solid matrix. In the limit of

an infinitely large thermal conductivity the thermal energy supplied at the fluid-solid interface will penetrate instantaneously to any location in the solid matrix resulting in a negligible imaginary part of the Nusselt number.

To account for this, the Nusselt number is calculated from the time averaged energy flux (4.22). It is assumed that this expression can only return the real part of the Nusselt number because a time average energy flux can not contain information about the dynamics of the system. The Nusselt number obtained from the time averaged energy flux is due to two roots of a quadratic equation. It is shown that only the positive solution can be used to extract to Nusselt number by considering the low Re_ω limit.

6.2 Microscopic Balance Equations

A microscopic analysis is included in part 1 in order to study the sensitivity of the Nusselt number for a microchannel geometry and to validate the macroscopic expressions for the Nusselt number. The real part of the Nusselt number is influenced differently by operating conditions and material properties:

1. Thermal mass ratio R
   A small thermal mass ratio causes an increase in Nusselt number because it maximizes the temperature difference to first order.

2. Thermal conductivity ratio γ_k
   A small thermal conductivity ratio (e.g. large solid thermal conductivity) will result in smaller Nusselt number compared to a large γ_k.

3. Reynolds number Re_ω
   An increasing Reynolds number will cause the thermal boundary layer to shrink therewith increasing the interfacial heat flux and the Nusselt number. At realistic values of the thermal mass ratio $R \in [0.1; 1]$ the Nusselt number is more sensitive to Re_ω because the temperature difference between the tow phases changes with Re_ω.

The imaginary part of the Nusselt number is a complex function of regenerator operating parameters and properties and warrants further research. This includes the peaking behavior for different values of the thermal mass ratio. In general, the

imaginary part of the Nusselt number is negligibly small for small $\mathrm{Pr}\,\mathrm{Re}_\omega$ combinations and a thermal conductivity ratio of $\gamma_k \leq 1$ for realistic values of the thermal mass ratio $R \in [0.1; 1]$. This finding is compatible with the assumption of infinite thermal conductivity in radial direction made for the derivation of (4.22).

The macroscopic expressions for the Nusselt number are validated using the microscopic model based on the microchannel geometry. It is shown that the Nusselt number obtained directly from the solution (4.8) is equal to the Nusselt number from the microscopic model in the limit of negligible thermal mass of the solid or in the high PrRe_ω limit. Both limits yield negligible solid temperature oscillations.

The Nusselt number derived from the time averaged energy flux shows a smaller discrepancy between macroscopically and microscopically evaluated Nusselt number. The Error is small if the fluid thermal conductivities are large, which represents the assumptions under which the macroscopic energy balance is derived. For this reason, the positive root of (4.8) is used to extract the Nusselt number form experimental data.

Part II

Experimental

Chapter 7

Experimental Recovery of Friction Factor and Nusselt Number

7.1 Key Parameters

This chapter is devoted to the experimental aspects of the recovery of friction factor and Nusselt number. The theory presented in part I only includes the analysis of the test section (i.e. the regenerator) and leaves out processes and influences that take place in the other parts of the hydraulic circuit or even outside of the circuit. In addition the precision of a measurement is discussed and its influence on the Nusselt number as well as temperature dependent material laws.

A fundamental experiment needed for the extraction of friction factor and Nusselt number is schematically shown in figure (7.1). For both quantities the super-

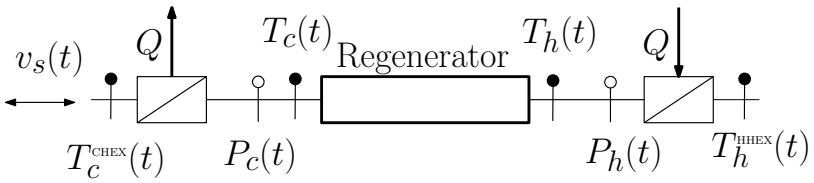

Figure 7.1: Schematic of fundamental experiment for extraction of friction factor and Nusselt number

ficial velocity, that is approximated as a first order Fourier series, must be known and is described by stroke and frequency f. Pressure and temperature must be measured at both ends of the regenerator. The ratio of first order temperature amplitude to time averaged temperature gradient is proportional to the dimensionless

Table 7.1: Experimental repertoire for the friction factor and Nusselt number recovery

Measured quantity	Symbol	Dimensionless symbol
Superficial velocity	v_{s1}	1
Pressure	$p_h,\ p_c$	$\hat{p},\ f_D$
Mean temperature	$T_{c0},\ T_{h0}$	$\mathrm{d}T_0/\mathrm{d}\xi$
temperature amplitude	$T_{c1},\ T_{h1}$	θ_{f1}

temperature to first order. For the extraction of the Nusselt number, the average temperature amplitudes of hot and cold side are taken to calculate the dimensionless temperature amplitude. The experimental data needed for the extraction of the Nusselt number is shown in table (7.1). The frequency can be estimated from all oscillating measurements. The friction factor and Nusselt number is then obtained by evaluating (4.23) and (4.22).

7.2 Dynamic Effects in Hydraulic Circuit

The hydraulic circuit as shown in figure (3.2) comprises three major hydraulic components: piping, heat exchangers and the regenerator. All of them have different hydraulic diameters resulting in different ranges of the kinetic Reynolds number. The different hydraulic diameters of the components are shown in table (7.2). As

Table 7.2: Hydraulic diameters of all major hydraulic components

Component	Hydraulic diameter d_h (mm)	Length L (mm)
Heat exchanger	1.7	250
Sphere regenerator	0.43	71
Microch. regenerator	0.7	71
Piping	6.6	$2.2 \cdot 10^3$

the kinetic Reynolds number increases with increasing hydraulic diameter, inertial effects (as shown by equation (5.4)) become pronounced. As the kinetic Reynolds number increases, friction will become less important. As $\mathrm{Re}_\omega \to \infty$ the entire pressure gradient will be converted into acceleration and the velocity will lead the pressure gradient by $\pi/2$. At small frequencies, acceleration is insignificant leading to a phase difference of π between pressure gradient and velocity. The phase

lag between pressure gradient and velocity (phase angle of piston velocity is normalized to zero) in the different hydraulic components is shown over a range of frequencies in figure (7.2). The phase angle is calculated using the analytical so-

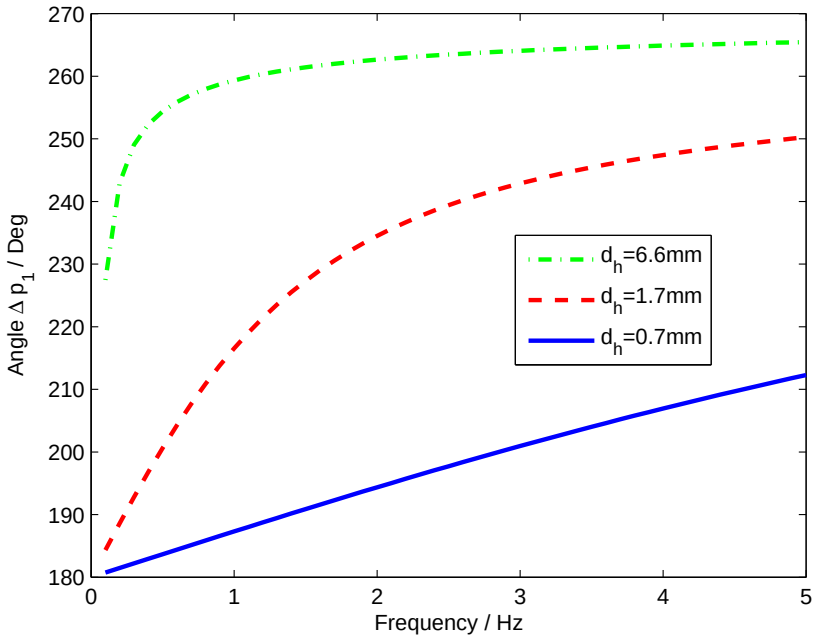

Figure 7.2: Phase angle of pressure in circular tube with different hydraulic diameter

lution for a pipe as presented in Appendix (B). Figure (7.2) shows clearly that the phase difference between pressure gradient and velocity increases as the frequency increases. The larger the hydraulic diameter, the larger the phases difference. In the limit of $f \to \infty$ the phase angle approaches -270°.

If the pressure difference across a component is measured and normalized with respect to measured piston velocity, a real and an imaginary part of the pressure drop is encountered as shown in figure (7.3). The imaginary part of the pressure drop represents the inertial pressure drop. As schematically illustrated in figure (7.3), the piping shows largest inertial pressure loss due to its large hydraulic diameter.

A thermodynamic analysis involves usually the consideration of the conservation laws for mass, momentum and energy. Due to the incompressible flow assumption, the mass balance must not be considered. The momentum balance contains the pressure gradient as driving force for the velocity. The velocity is then

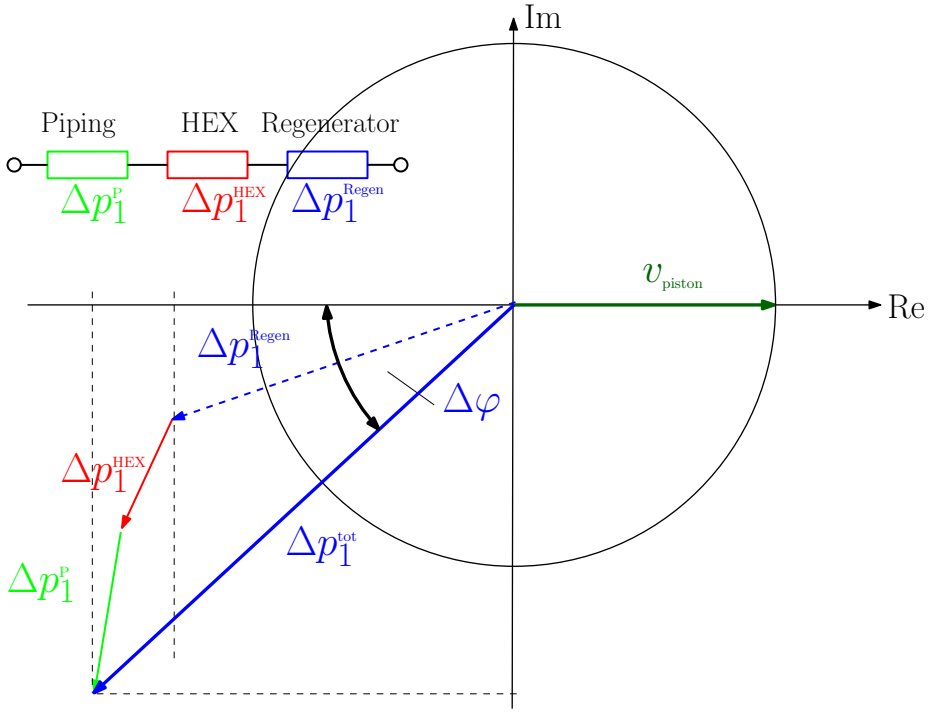

Figure 7.3: Serial addition of pressure drops of the hydraulic components

calculated given a pressure gradient. Once the velocity is known it can be used to initialize a solution of the thermal energy balance for temperature. In this sense, it is clear that the phase of experimental data should be normalized with respect to pressure gradient phase angle and not with respect to the piston velocity phase angle as done in the derivation of the macroscopic momentum balance presented by equations (3.59) and (3.60).

The phase angle of the velocity must be equal at any point of the hydraulic circuit due to mass conservation. If the pressure drop of each component would be measured separately, all measurements would show different phase angles of pressure drop when normalized with respect to the piston velocity as illustrated in figure (7.3). Therefore the total pressure drop in the hydraulic circuit must correspond to the piston velocity as shown in figure (7.3).

The normalization process is summarized in figure (7.4). The left schematic in figure (7.4) shows the situation of how experimental data is presented, that is, normalized with respect to measured piston velocity. In this situation the phase difference between piston velocity and temperature is misinterpreted, because the data has been blindly normalized with respect to piston motion. The center pic-

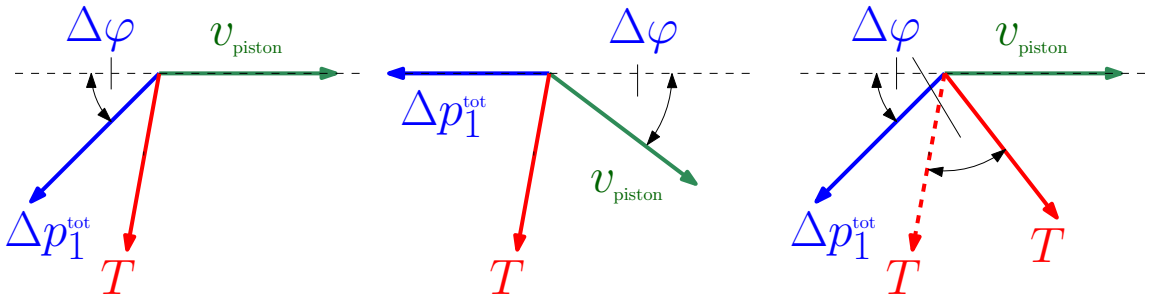

Phase of pressure drop and temperature normalized with respect to piston velocity

Phase of piston velocity normalized with respect to pressure drop

All experimental data rotated to obtain piston velocity with zero phase angle

Figure 7.4: Normalization process of experimental data

ture shows the piston velocity normalized with respect to pressure gradient. In this situation the velocity and a temperature measurement show correct phase difference. It must be stressed that in the center picture the pressure drop shows no imaginary part, and is reflected in the piston velocity. The macroscopic thermal energy balance is not derived by accounting for this phase angle in piston velocity and must be renormalized as shown in the right hand side schematic. The right picture shows the same situation as the center picture just rotated in order to obtain a zero phase angle of the velocity applicable to the macroscopic thermal energy balances (3.59) and (3.60).

The same procedure has been already applied to the microscopic balance equations. The solution of the velocity field from the momentum balance (5.4) is in general complex (depends on the value of the pressure gradient in equation (5.4)) and is used to initialize a solution of the thermal energy balances (5.8) and (5.9). The temperature oscillations are then normalized with respect to phase angle of mean velocity in order to apply it to the macroscopic thermal energy balance for validation purposes.

7.3 Uncertainty and Error Propagation

Extracting the Nusselt number based on temperature oscillations requires accurate amplitude and fast response. A thermocouple can measure temperature within a certain error bound that depends on fabrication and size of the thermocouple as

well as the temperature range to be measured. As the data is processed, this error will propagate and eventually magnify. In this section error bounds for the Nusselt number are discussed.

The uncertainty for a temperature reading is expressed as

$$T = \bar{T} \pm \delta T \tag{7.1}$$

where δT is the uncertainty in the temperature measurement. The uncertainty in a measurement must be determined statistically and is usually declared by the supplier of a thermocouple. Type E thermocouples have a uncertainty of $\delta T = 1.5$ K [30][1] . According to the Gaussian law of error propagation [31], the relative error of the Nusselt number is

$$\frac{\mathrm{dNu}}{\mathrm{Nu}} = \frac{\partial \mathrm{Nu}}{\partial \theta_{f1}} \frac{\mathrm{d}\theta_{f1}}{\mathrm{Nu}} \tag{7.2}$$

With reference to equation (4.22), the differential is given by

$$\frac{1}{\mathrm{Nu}} \frac{\partial \mathrm{Nu}}{\partial \theta_{f1}} = -\frac{1}{\mathrm{Re}\left[\theta_{f1}\right] \sqrt{1 - 4\left(1+R\right)^2 \mathrm{Re}\left[\theta_{f1}\right]^2}} \tag{7.3}$$

The temperature differential is substituted using

$$\mathrm{d}\theta_{f1} = \frac{\partial \theta_{f1}}{\partial \Delta T_0} \delta\left(\Delta T_0\right) \tag{7.4}$$

The uncertainty in temperature difference $\Delta T_0 = T_c - T_h$ is also given by Gauss law of error propagation

$$\delta\left(\Delta T_0\right) = \sqrt{\delta T^2 + \delta T^2} = \sqrt{2} \cdot \delta T \tag{7.5}$$

Collecting the above results and substituting in equation (7.2) gives

$$\frac{\mathrm{dNu}}{\mathrm{Nu}} = \frac{1}{\sqrt{1 - 4\left(1+R\right)^2 \mathrm{Re}\left[\theta_{f1}\right]^2}} \frac{\sqrt{2} \cdot \delta T}{\Delta T_0} \tag{7.6}$$

The relative error (7.6) is shown in figure (7.5). In general the statistical deviations in Nusselt number can be minimized using large temperature spans as shown in figure (7.5). Figure (7.5) shows the uncertainty for different nondimensional tem-

[1] According to IEC EN 60584-2 thermocouple tolerance

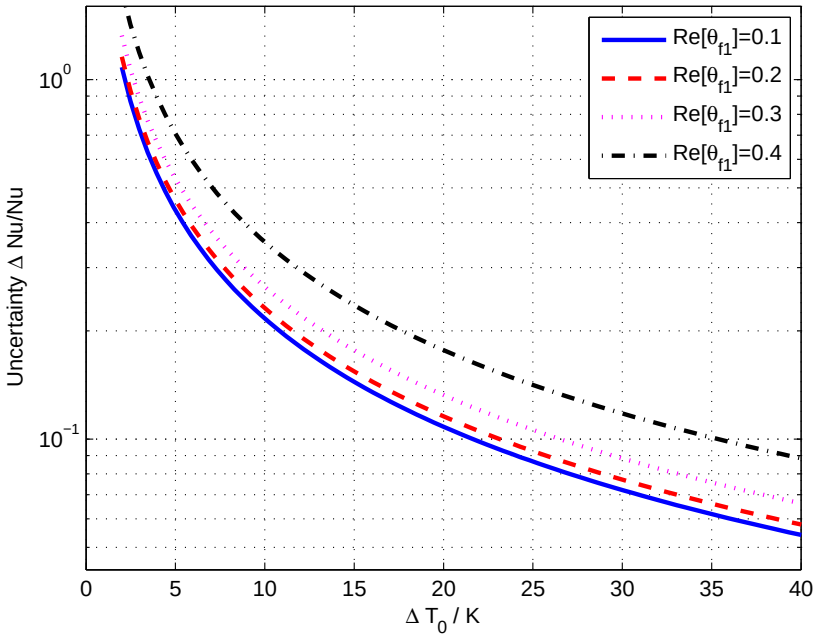

Figure 7.5: Relative error of the Nusselt number due to uncertainty in temperature measurement

perature amplitudes. It can be concluded that large dimensionless amplitudes also require large temperature spans between hot and cold sides of the regenerator in order to maintain a small error.

7.4 Temperature Dependent Material Laws

Material properties depend on temperature. For experiments using water as the heat transfer fluid, the dynamic viscosity μ is the property that shows the largest variation with temperature within the context of the present analysis. Figure (7.6) shows the viscosity as a function of temperature. The viscosity decreases with increasing temperature. Thus the pressure drop is smaller if a hydraulic component is operated at high temperatures. However, regenerators are operated under non isothermal conditions. The incorporation of non-linear material laws requires more modeling effort and has not been considered for the present work. Instead, fluid properties are assumed to be constant and determined by the average mean temperature.

It is pointed out that large temperature spans minimize the statistical error.

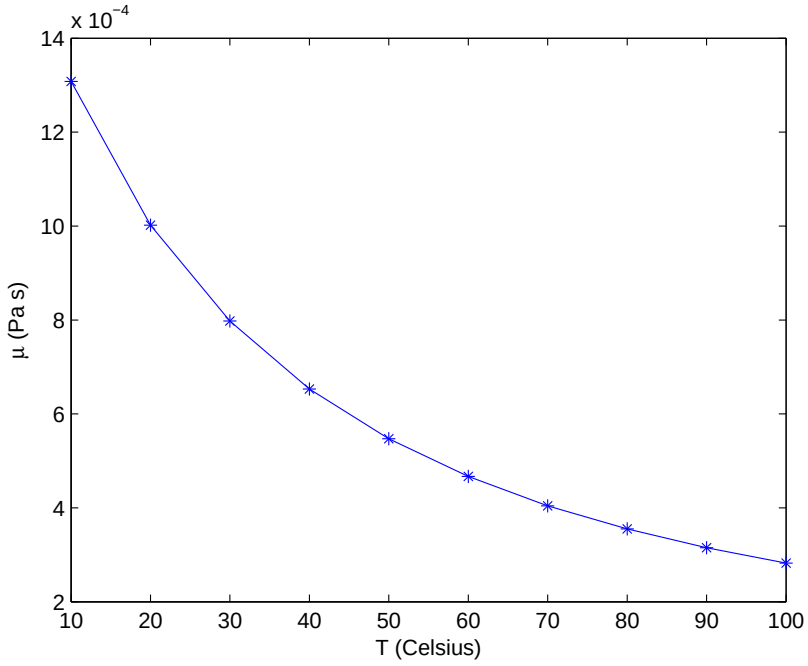

Figure 7.6: Dynamic viscosity of water as a function of temperature [26]

However, the large temperature range under which a regenerator is operated shows significant dependence on the dynamic viscosity.

Chapter 8

Test Apparatus and Experimental Results

8.1 Test Apparatus

This chapter gives an overview of the experimental setup of the Passive Regenerator Test Apparatus (PRTA). All components are discussed in detail. Test results are presented at the end of this chapter.

The design of the Passive Regenerator Test Apparatus (PRTA) aims for reliable control of the volumetric fluid flow and temperature span across the regenerator test section. A simple method for achieving this is chosen: a piston-cylinder type fluid displacer, driven by a variable speed DC motor, forces a controlled volume of fluid back and forth through a closed loop circuit. A crank arm mechanism converts the rotational motion produced by the DC motor into a linear piston motion. This assures sinusoidal waveform over time at a given rotational speed of the motor.

The regenerator is situated between two shell and tube heat exchangers (HEX) as shown in figure (8.1). The heat exchangers are made up of straight aluminium tubes of diameter 1.7 mm and a length of 240 mm. The housing inner diameter of the HEX is 31 mm which is equal to the diameter of the regenerator housing. The porosity of the HEX is $\epsilon_{\text{HEX}} = 0.25$. The heat exchangers are hooked up to a chiller and heater unit, respectively. The specifications of the two devices are summarized in table (8.1). The chiller unit has a cooling capacity of 1.2 kW with an operating range between -25 ^{o}C and 80 ^{o}C. The maximum flow rate of the chiller unit is 28

Table 8.1: Chiller and Heater specifications

Unit	Power (kW)	Operating temp. range (^{o}C)	Flow rate (Liters/min)
Chiller	1.2	[-25,80]	28
Heater	0.8	[-40,200]	15

Liters/min. The heater unit as a maximal heating power of 0.8 kW and maximal operating range between -40 °C and 200 °C. The maximum flow rate of this unit is 15 Liters/min. Both units are operated using distilled water and can thus not operate bellow the freezing point.

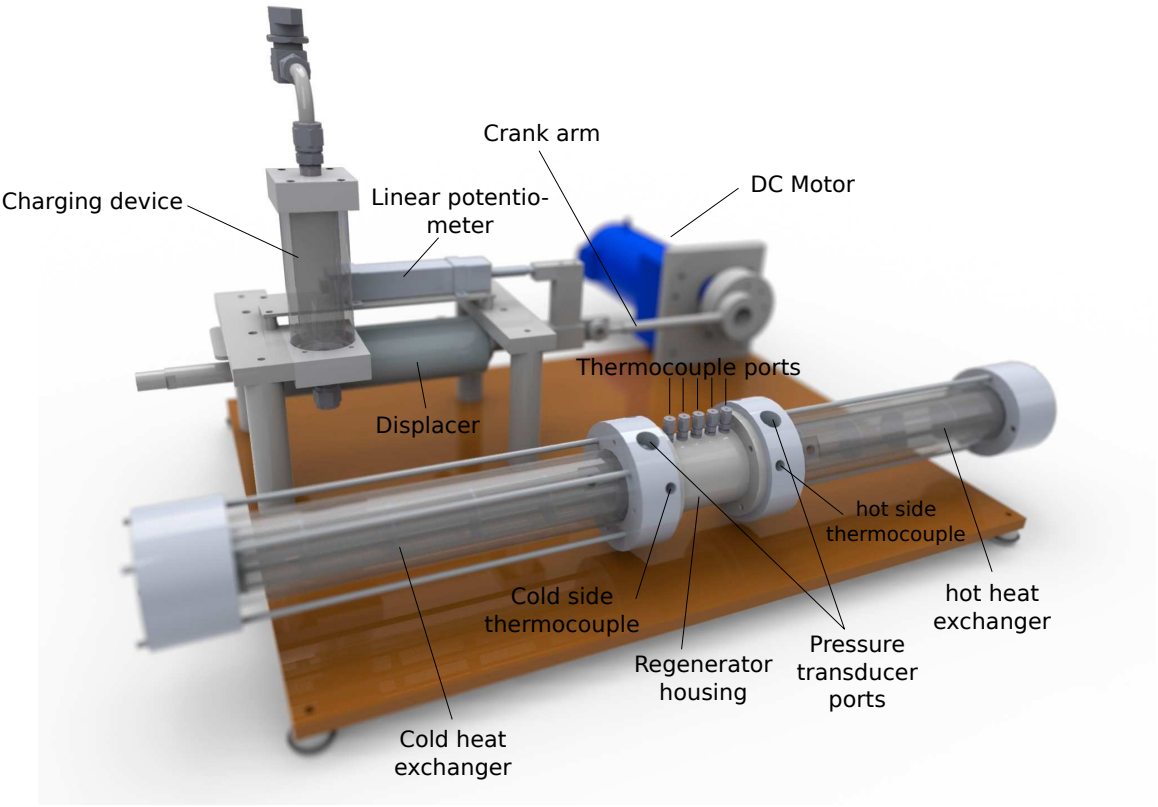

Figure 8.1: Experimental setup

A circular tube with diameter $d_r = 31.7$ mm and length $L_r = 71.2$ mm made of plastic (Polyixymethylene) is used as regenerator housing and situated between hot and cold HEX as shown in figure (8.1). The shell can accommodate different regenerator geometries such as wire meshing, packed particles, perforated plates, parallel channels, plates or tubes. At each ends of the regenerator two fine tip,

type-E thermocouples (diameter 0.5 mm) are used to measure temperature. The response time of these thermocouples is on the order of 10 ms and much smaller than the actual physical cycle time. Five additional thermocouples can be placed at equidistant axial positions inside the regenerator. Their radial position depends on the regenerator geometry to be tested. An additional two thermocouples can be placed between the two heat exchangers and the displacer to measure temperature difference across the heat exchangers.

A potentiometer is placed on top of the displacer to resolve displacer position as a function of time.

The pressure drop across the regenerator can be measured with the two pressure transducers at each end of the regenerator. In addition, another pressure transducer is placed between the HHEX and the displacer to measure pressure drop across the HHEX. A schematic representation of the PRTA is shown in figure (8.2). All measured quantities (in total 11 temperature, 3 pressure and 1 potentiometer readings) are shown in figure (8.2).

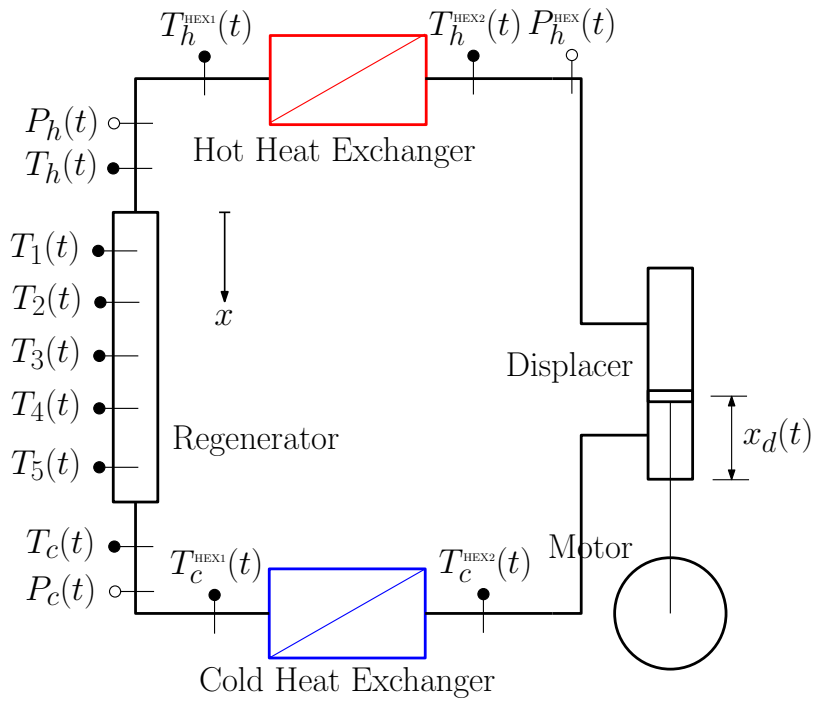

Figure 8.2: Schematic of PRTA

8.2 Test Section

The present work deals with two regenerator geometries: a microchannel regenerator and a packed particle bed regenerator made of spherical particles. The

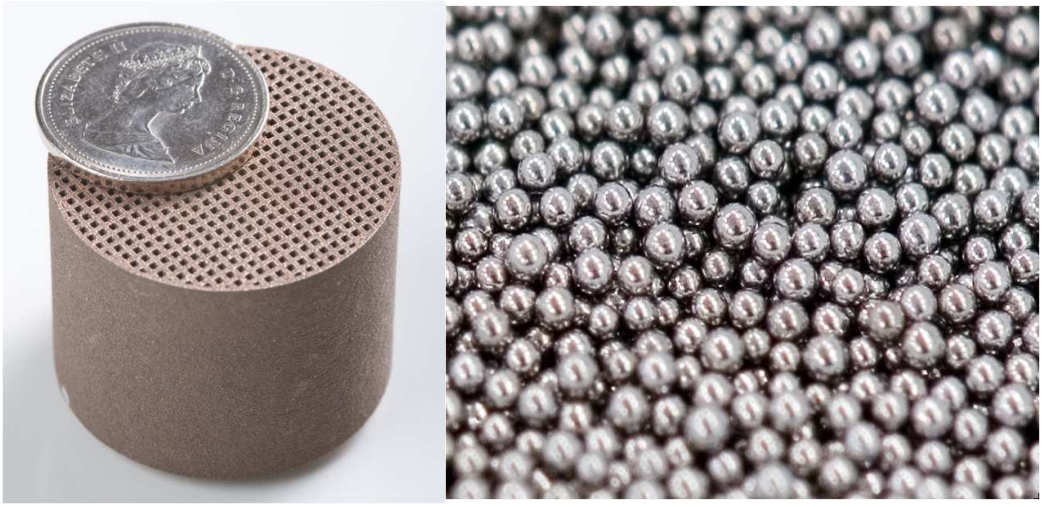

Figure 8.3: Photograph of a sintered micro channel puck and spheres

microchannel regenerator is made up of three bronze pucks (see figure (8.3)) and was produced using laser sintering technology at the University of Salerno in Italy. The channel height is $h_c = 0.7$ mm and the wall thickness $h_w = 0.5$ mm resulting in a hydraulic diameter equal to the channel height $d_h = h_c$. The surface finish is fairly rough and is estimated to be one order of magnitude smaller than the hydraulic diameter. The porosity is $\epsilon = 0.32$.

Table 8.2: Geometrical properties of microchannel and spheres regenerator

Geometry	Porosity ϵ	Hydraulic diameter d_h (mm)	Specific surface area a_{sf} (m^2/m^3)
Microchannels	0.32	0.7	1829
Spheres	0.39	0.43	5490

The stainless steel spheres have a diameter of $d_p = 1$mm. The porosity of the spheres is determined by measuring the mass of the spheres after it is packed in the regenerator. The porosity, hydraulic diameter and the specific interfacial surface area are compared in table (8.2). It can be seen that the porosity of the two regenerators is slightly different. The hydraulic diameters are in the same order of

magnitude. However, the specific surface area of the spheres is about three times as large compared to the microchannels.

The regenerators also differ in terms of thermal properties. They are summarized in table (8.3).

Table 8.3: Thermal properties of microchannel and spheres regenerator

Geometry	Heat capacity c_s (J/(kg K))	Th. conductivity κ_s (W/(m K))
Microchannels	435	30
Spheres	500	16

The heat capacities of the two regenerators are similar. This is not the case for the thermal conductivity. Bronze shows a larger thermal conductivity (by a factor of two) than stainless steel. It must be noted that these are intrinsic values and not effective values. Due to the sporadic contact of the spheres it can be expected that the geometrically effective thermal conductivity of the spheres is even smaller than its intrinsic value.

The microchannel geometry can only be tested using the outside thermocouples. The inside thermocouples (T_1-T_5) only measure the outside wall temperature of the regenerator. The particle bed can be tested using the inside thermocouples. They are radially centered. In order to get a direct comparison of the two regenerators, only the outside thermocouples are used for the analysis.

The microchannel geometry is well suited for both experimental and theoretical determination of heat transfer and pressure drop characteristics. The homogeneity in the axial direction and the rectangular front face makes this type of regenerator a well suited candidate for numerical simulation of heat transfer and pressure drop characteristics that can be validated against experimental results.

8.3 Experimental Procedure

There are three degrees of freedom that can be controlled by the experimentalist:

1. The stroke, L_s, controls the amount of fluid that is displaced during one cycle. The stroke can be adjusted by changing the length of the crank arm or the size of the displacer.

2. The frequency determines the duration of the cycle and can be controlled by the voltage supplied to the DC Motor.

3. The time averaged temperature span $\Delta T = T_{c0} - T_{h0}$ can be imposed by changing the chiller settings.

In general each experiment is characterized by stroke, frequency and time averaged temperature span. Once the system is in cyclic steady state a number of cycles are recorded. Each signal (temperatures, pressure and displacement from potentiometer) is written in form of a discrete time series to a file. The experiment is repeated using an incremental change in frequency. It is not necessary to maintain the temperature span at a constant value; however, a large temperature span is desirable since it increases the accuracy to measure temperature oscillations (large temperature spans will result in larger temperature oscillations). The thermal oscillations are of particular interest for the extraction of heat transfer data. This procedure is repeated for different stroke values.

Table 8.4: Operating range of PRTA

Stroke L_s (mm)	Displaced Vol. V_{disp} (ml)	A_0 Spheres	A_0 Microch.	f (Hz) Spheres	f (Hz) Microch.
18	17	63	47	[0.15,2.4]	[0.2,2.9]
36	34	131	99	[0.2,1.2]	[0.5,1.4]
54	51	185	139	[0.15,0.8]	[0.2,0.9]

Table (8.4) shows the operating range of the PRTA. The maximum operating frequency decreases with increasing stroke because the friction of the piston against the cylinder wall increases. In addition the increased pressure drop of the spheres at higher frequency also limits the maximum frequency.

8.4 Data Processing

The data is processed using a discrete Fourier transform (DFT). Rectangular windows are applied matching beginning and end of the signal to assure sharp spectral resolution. The spectral breakdown of the displacement signal and the reconstructed signal from the spectra is shown in figure (8.4). It is clearly observable

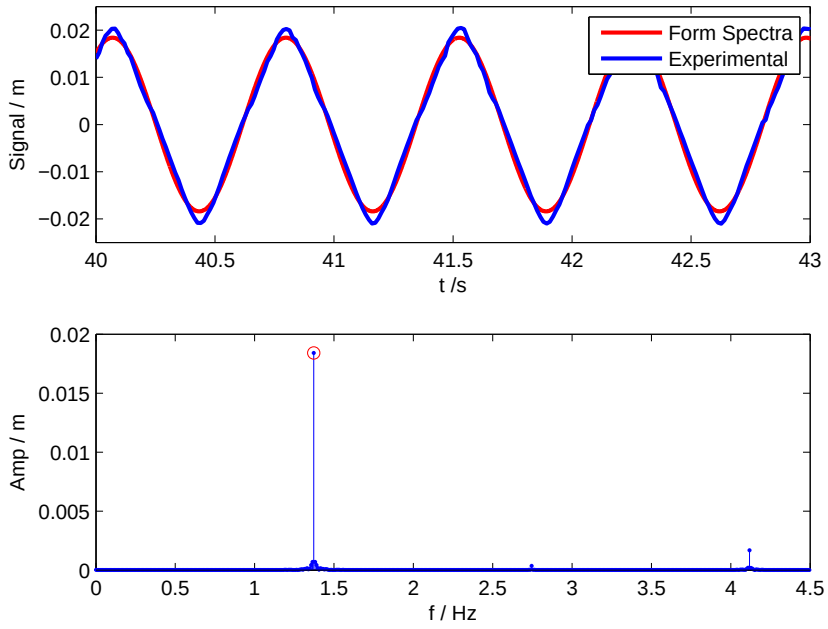

Figure 8.4: Spectra of displacement signal

that the the piston motion is well approximated by a pure sinusoid with frequency $f = 1.4$ Hz and negligible higher harmonic content.

The spectra for the hot side temperature for microchannels and spheres are shown in figures (8.5) and (8.6), respectively . Throughout an experiment, the dominant frequencies of all signals are equal as can be observed in figures (8.5) (figure (8.6) corresponds to an experiment with lower frequency). The temperature reading in the microchannel experiment is well approximated by a pure sinusoid. The temperature reading using the spheres geometry shows significant higher harmonic content. The observation of multiple frequencies is a consequence of the time dependency of transport properties (such as dispersion) or general nonlinearities (temperature dependency of viscosity). This follows from the fact that the higher order frequencies are a multiple of the dominant frequency. The spectra

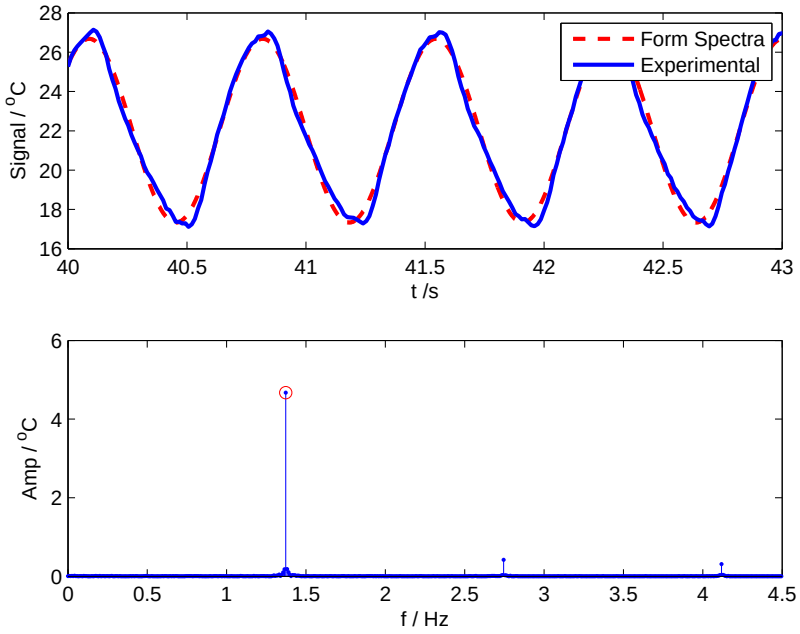

Figure 8.5: Spectra of hot side temperature signal using microchannels

of the hot side reading in figure (8.6) has a dominant frequency of $f_1 \approx 0.8$ Hz, the second frequency $f_2 \approx 1.6$ Hz and the third $f_3 \approx 2.4$ Hz, indicating time variance or nonlinearities of macroscopic transport properties.

The spectra of the pressure drop signal $\Delta p = p_c(t) - p_h(t)$ is shown in figure (8.7). The pressure drop through the microchannel regenerator is expected to be small, resulting in a rather noisy measurement of the pressure drop signal. Also this signal shows higher harmonic content.

It must be emphasized that the theory presented in earlier chapters only applies to the dominant oscillations of all signals; therefore, in what follows, higher order harmonics are neglected.

Each experiment consists of 15 time series (temperature, pressure and linear pot signals) resulting in roughly 700 time series for all experiments conducted. The analysis through a DFT is favourable because only the complex amplitudes must be considered instead of the entire time series. The spectral analysis of a signal is in general applied after all time series of an experiment are recorded. This can in general also be done at real time using DFT.

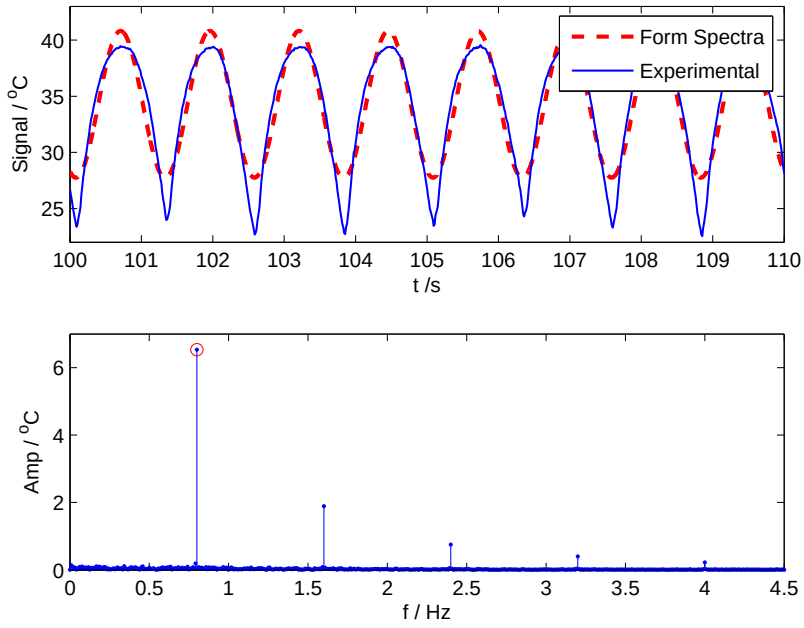

Figure 8.6: Spectra of hot side temperature signal using spheres

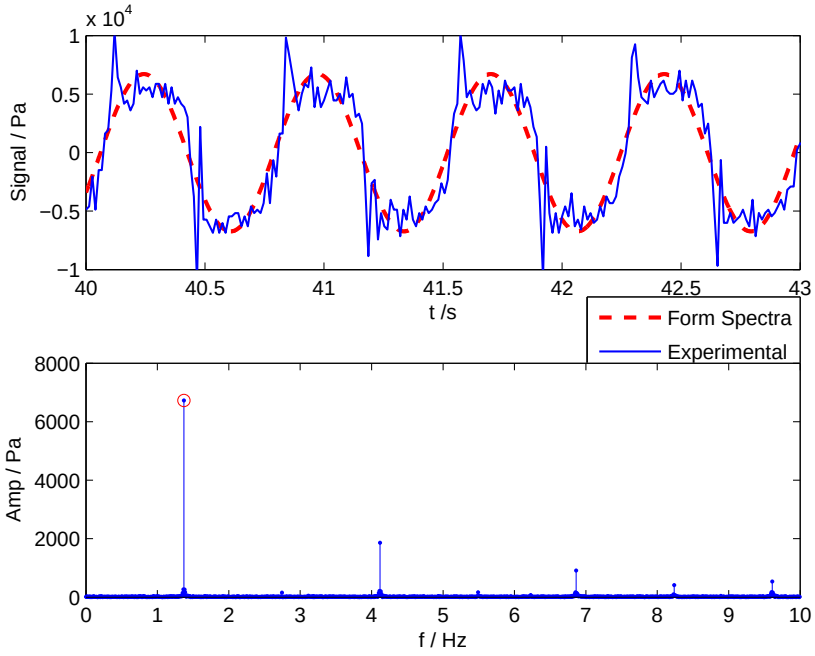

Figure 8.7: Spectra of pressure drop for a microchannel experiment

8.5 Experimental Results

The experimental results of temperature and pressure readings are presented over the entire frequency and stroke range that is covered experimentally. First, the time averaged temperature span for both geometries is considered. Figure (8.8)

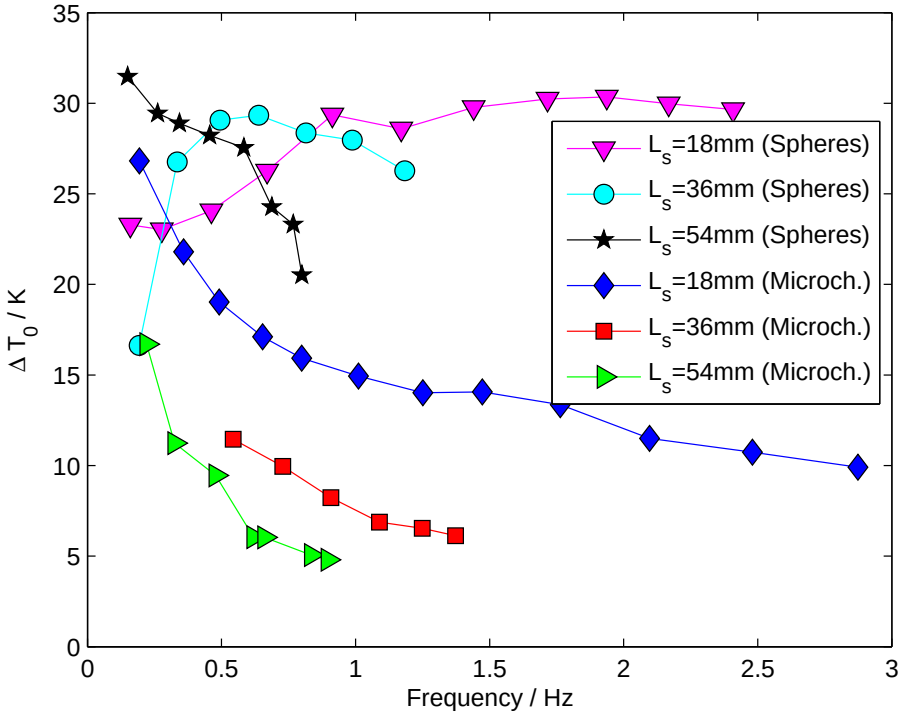

Figure 8.8: Time averaged temperature difference between hot and cold side for both geometries

shows the mean temperature difference between hot and cold side for all strokes and frequencies recorded.

The microchannels show reduced temperature spans as the frequency is increased mainly due to heat transfer limitations in both heat exchanger and regenerator as the frequency increases. The temperature span also consistently drops as the stroke is increased. A higher stroke will increase the velocity in the regenerator and thus limit the heat transfer.

The situation for the corresponding experiment using spheres shows the reverse effect at small frequencies. For strokes $L_s = \{18, 36\}$mm the temperature span increases first with frequency until it reaches a maximum value and drops

again. At the highest stroke the temperature span is maximal in the low frequency limit and decreases monotonically with frequency.

It is suspected that at low frequency other heat transfer effects lower the regeneration process. Dispersion is known to be significant at low frequency for a packed particle bed geometry [7] and might be responsible for significant diffusion in the regenerator. As the frequency increases and stroke increases advection is expected to be amplified such that diffusion effects become negligible. This would explain the monotonically dropping temperature span for the largest stroke $L_s = 54$mm.

In general the temperature spans using spheres are larger than corresponding spans for the microchannels at the same chiller sink and heater source temperature. This indicates that the regeneration process is amplified using the sphere geometry.

The temperature amplitudes and their phase angles (normalized with respect to velocity, i.e. $\arg[v_{s1}] \doteq 0$) for the micro channel and sphere geometry are shown in figures (8.9) and (8.10), respectively. In general the cold side amplitudes are slightly larger than the hot side amplitudes. The amplitudes at stroke $L_s = 18$ mm remain fairly constant over frequency but are largest at intermediate frequencies. Again, this might be an indicator for transport modes like dispersion that are pronounced at low frequencies. At higher strokes, amplitudes drop with increasing frequency. The amplitudes are a function of both the heat transfer quality and the temperature span (because there can not be thermal oscillation without the presence of a temperature difference between hot and cold end). Therefore the decreasing amplitudes at higher frequencies can be understood as an indicator for increased heat transfer. It is interesting to note that the intermediate stroke value shows higher amplitudes (in the corresponding frequency range) than the highest stroke amplitudes.

The phase response on both sides of the regenerator show similar trends. However, the cold side thermocouple responds quicker than the hot side with respect to the mass flow in the system. The phase lags exceed the -90° mark completely on the hot side and partially on the cold side. This violates the model stated in equation (4.28), phase angles must be between -90° and 0°.

A similar behavior can be observed for the sphere experiment. The difference is that the amplitudes are in general smaller at higher frequencies compared to the microchannel experiment. In addition, the entire hot side and partially the

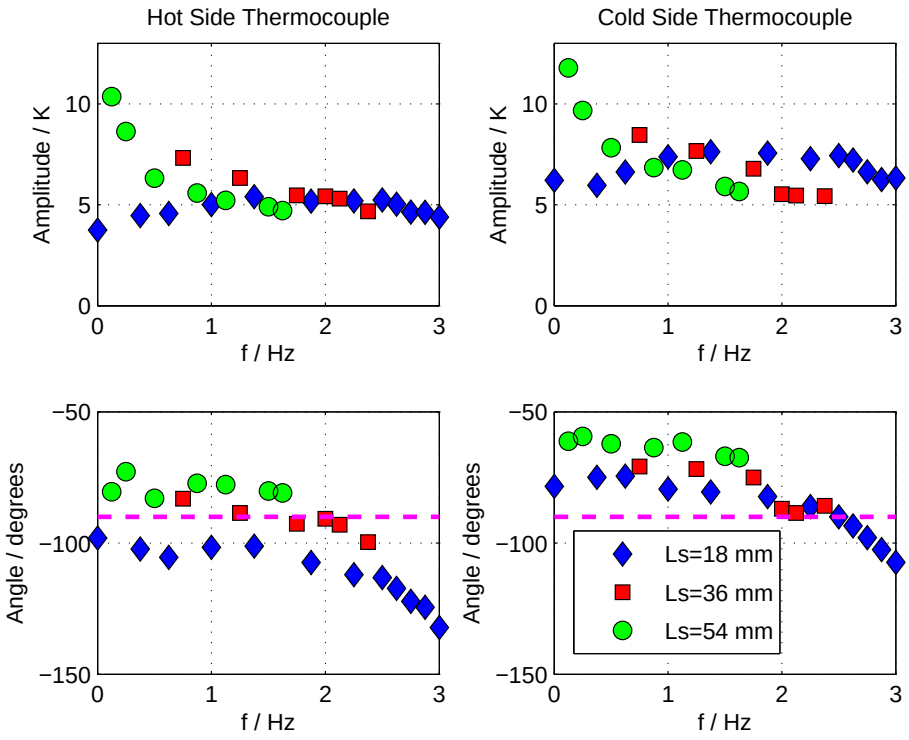

Figure 8.9: Temperature amplitude and phase response for microchannel experiments

cold side phase are smaller than -90°. This is problematic since the real parts of the temperature amplitudes are needed for the evaluation of the Nusselt number (4.22). According to the model, the real parts of the temperature amplitude are assumed to be larger than zero. In figure (8.10) most real parts of the temperature amplitudes are negative. The pressure drops across the heat exchanger, the microchannel regenerator and the spheres regenerator are shown in figure (8.11).

All pressure drop magnitudes increase with frequency and stroke (as a result of increased fluid velocities). As expected, the spheres show the largest pressure drop. The heat exchangers show the lowest pressure drop because of the low porosity.

The phase angle of the pressure drop can increase with frequency due to inertial contributions to the total pressure drop. In the high frequency limit the phase of the pressure drop can not exceed 270° and in the low frequency limit the phase angle must be 180° as shown in equation (3.58). Both the heat exchanger and microchannel geometry are within those limits and they show increasing phase

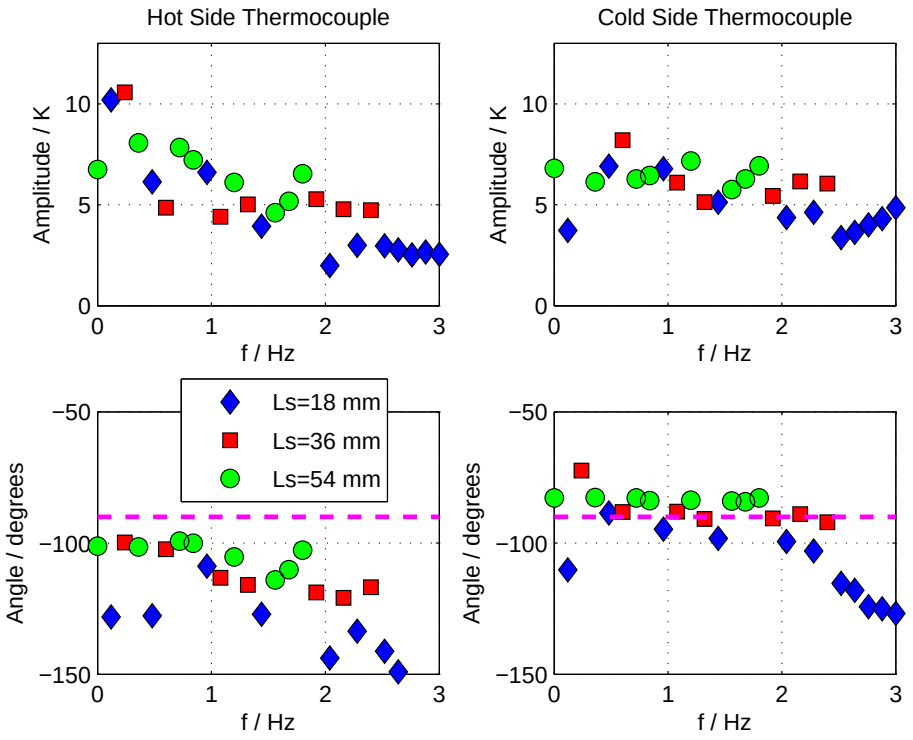

Figure 8.10: Temperature amplitude and phase response for packed particle bed experiments

angle as the frequency increases. As a result the heat exchangers show larger phase angles than the microchannels. According to this theory, the spheres should show phase angles around 180^o. In reality they significantly deviate from this value as shown in figure (8.11). In addition the phase angles decrease with increasing frequency which contradicts model predictions.

In order to understand this phenomena, figure (8.12) compares the pressure drop with a temperature gradient to pressure drop measurements under isothermal conditions at $T = 20^o$C.

The magnitude of the pressure drop in the isothermal case is in general lower than in the non isothermal case. It must be noted that the viscosity of water decreases with increasing temperature. Therefore, the mean viscosity in the non-isothermal case might be higher than the reference viscosity at $T = 20^o$C. Interestingly the phase angle in the isothermal case remains constant at 180^o. The non-isothermal measurements drop with increasing frequency as already shown in (8.11).

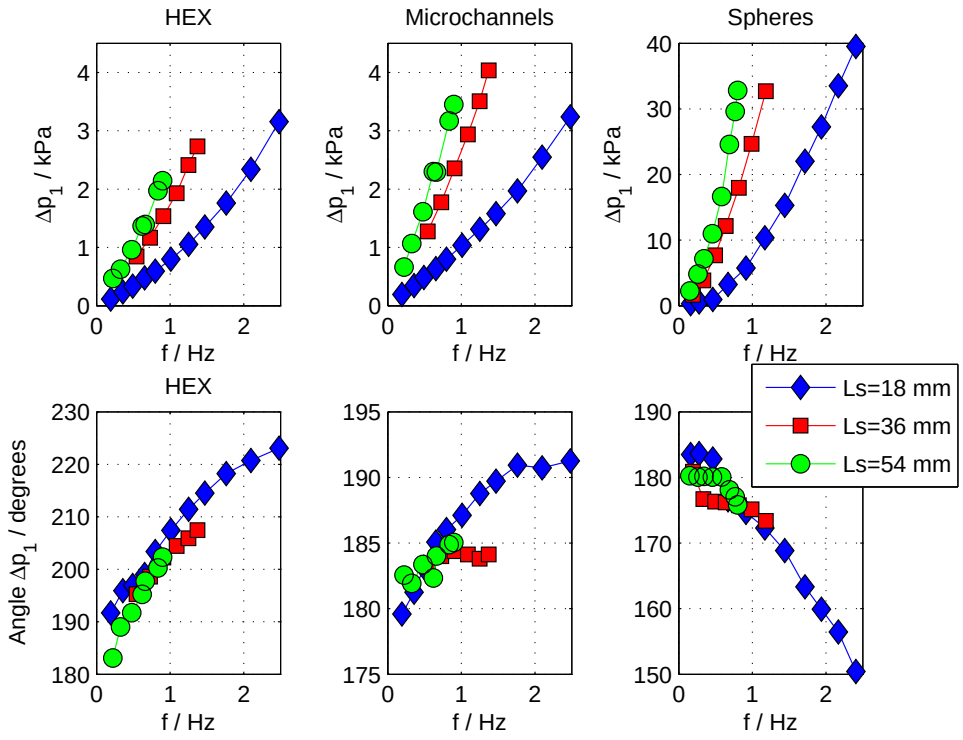

Figure 8.11: Pressure drop of heat exchanger, microchannels and spheres geometry

Conversely, the microchannel tests do not show this apparent drop in the phase angle with frequency. It is possible that the smaller temperature spans of the microchannel regenerator does not allow the same effect as in the spheres. Hence, the drop in phase angle must be a function of both temperature difference and geometry. Further investigation is needed to understand this temperature dependency of the phase angle of the pressure drop.

In this chapter, the experimental setup and raw experimental data is presented. In the next chapter further data manipulation is applied in order to evaluate the Nusselt number from experimental data.

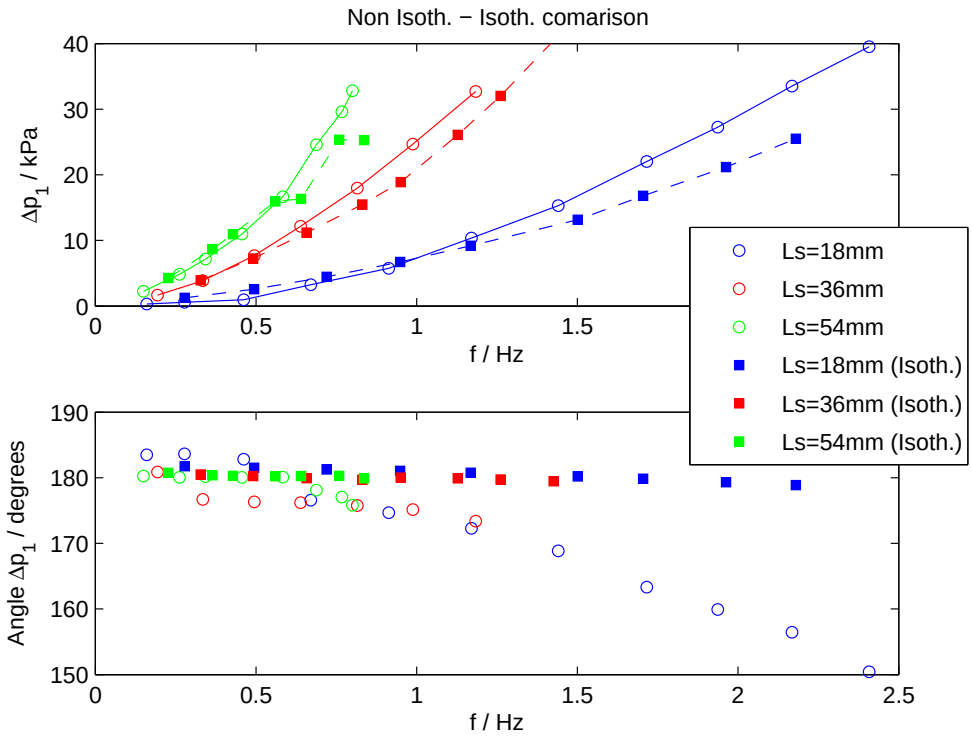

Figure 8.12: Comparison of pressure drop at isothermal and non isothermal conditions

Chapter 9

Phase Correction

9.1 Accounting for Dynamic Effects

In the previous section it is concluded that the temperature measurements are located outside of the suspected domain. In fact, some of the temperature measurements show phase angles smaller than -90°.

This is problematic, because the experimental evaluation of the Nusselt number (4.22) will result in negative Nusselt numbers.

The reason for this is that the temperature data has been normalized with respect to piston velocity and not with respect to total pressure drop of the entire hydraulic circuit as it is discussed in section (7.2). As a result the data points that have phase angles smaller than -90° and will include the phase lag due to inertial losses of the other hydraulic components in the circuit. To account for this, the phase angle data is corrected using a correction angle $\Delta\varphi$ as illustrated in figure (7.2) that removes the phase lag due to inertial losses from the temperature amplitudes.

In order to calculate $\Delta\varphi$ the total pressure drop of the hydraulic circuit is needed. The total pressure drop can not be entirely reproduced from experimental data since there is pressure transducer placed between displacer and heat exchanger as shown in figure (8.2). The missing contribution to the total pressure drop is the pressure drop in the piping that has significant inertial pressure losses. The pressure drop in the piping is calculated using the analytical solution for the flow in a circular tube presented in Appendix (B). The total pressure drop can be recovered by superimposing the model results for pressure loss in the piping with the

pressure drop measurements across heat exchanger and regenerator.

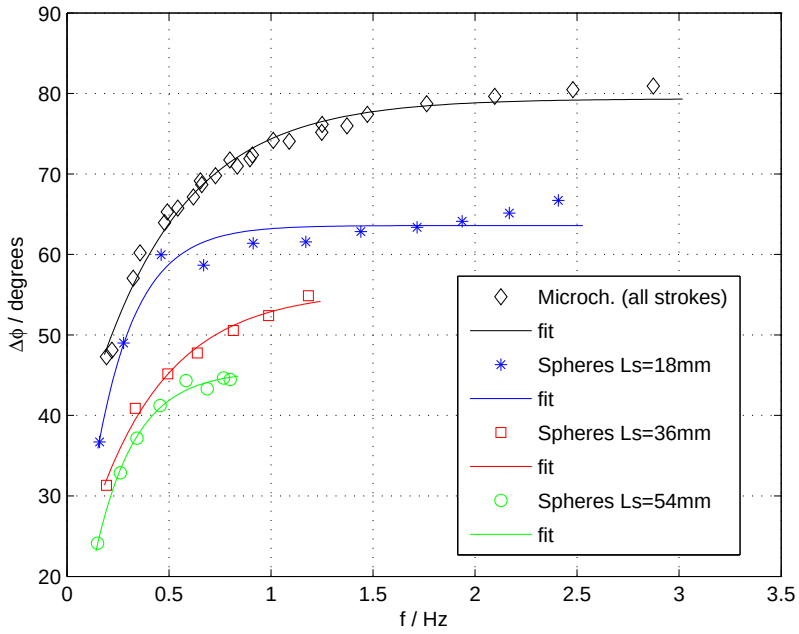

Figure 9.1: Phase correction $\Delta\varphi$ for microchannels and spheres geometry

Figure (9.1) shows the phase correction $\Delta\varphi$ for different geometries and operating conditions. It can be seen that the microchannels show largest phase correction due to their large hydraulic diameter. The phase angle as a function of frequency is parametrized using an exponential function

$$\Delta\varphi = c - a \cdot \exp\left(-b \cdot f\right) \tag{9.1}$$

A standard least square parameter estimation is applied to find the coefficients $\{a, b, c\}$. Their values are summarized in table (9.1)

Regenerator	a	b	c
Microch. (all strokes)	0.84	2.27	1.39
Spheres ($L_s = 18$mm)	1.04	5.04	1.11
Spheres ($L_s = 36$mm)	0.69	2.71	0.97
Spheres ($L_s = 54$mm)	0.80	5.05	0.79

Table 9.1: Parameter values for different geometries and operating conditions

9.2 Phase corrected temperature measurements

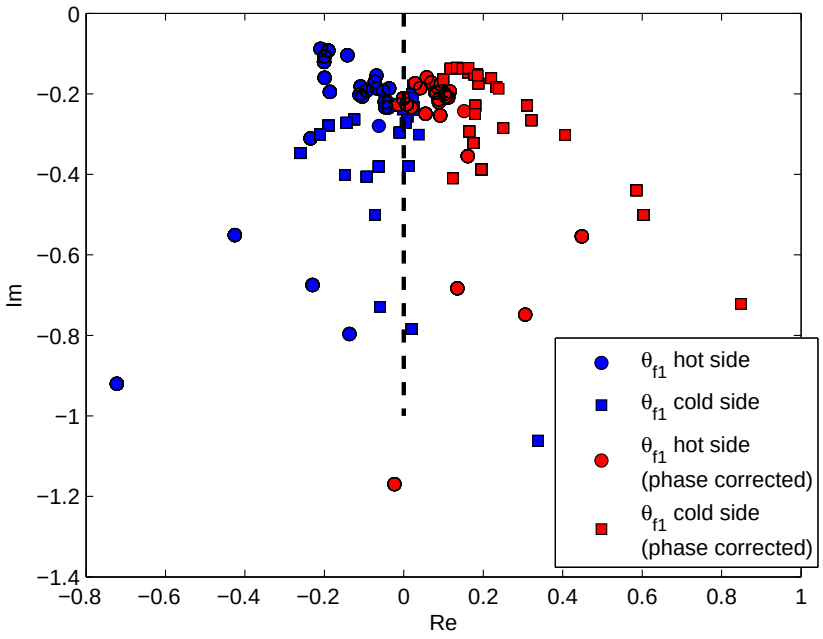

Figure 9.2: Phase corrected data for spheres regenerator

The originally measured temperature amplitudes presented in section (8.5) are corrected by rotating the original measurements by the angle $\Delta\varphi$. In complex notation this can be expressed as

$$\theta_{f1}^{\text{corr}} = \theta_{f1} \cdot \exp\left(i\Delta\varphi(f)\right) \tag{9.2}$$

Figure (9.2) shows the angle of the phase corrected temperature measurements for the sphere regenerator. The red symbols represent the phase corrected data $\theta_{f1}^{\text{corr}}$ while the blue symbols that data that is normalized with respect to piston velocity. The same plot is shown for the microchannel regenerator in figure (9.3).

It can be be seen that all corrected measurments have a phase angle larger than -90°. The microchannels temperture measurements are partially corrected to a phase angle slightly larger than zero. It must be emphasized that temperatures are corrected using the analytical solution for the oscillating flow in a circular pipe. How well this solution approximates the actual pressure drop in the pipe is unknown and can easily be overestimated resulting in slightly positive phase angles.

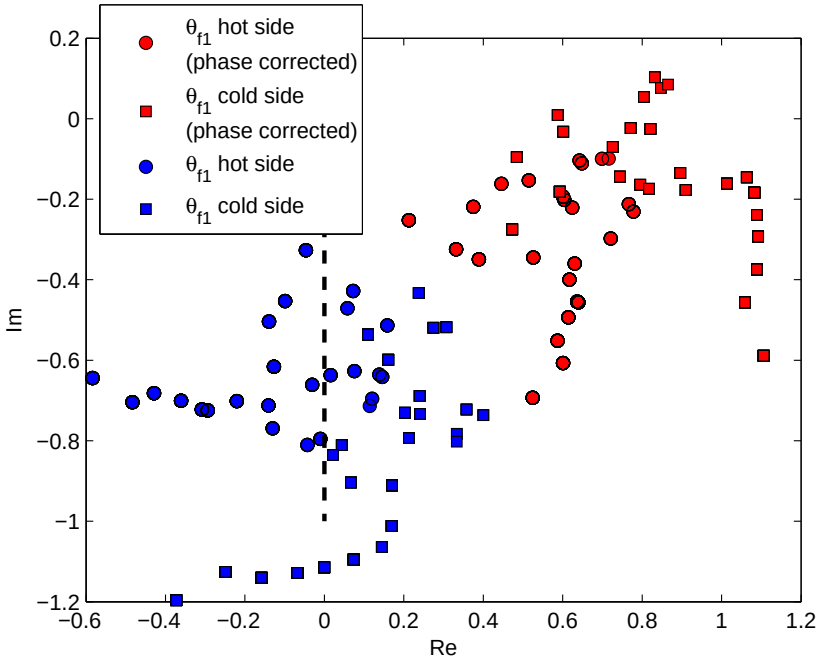

Figure 9.3: Phase corrected data for microchannel regenerator

In the remainder, the phase corrected temperature amplitudes are used to extract the Nusselt number.

Chapter 10

Experimental Evaluation

10.1 Friction Factor

In this chapter friction factor and Nusselt numbers are evaluated from experimental data. Both quantities are compared against model predictions. The friction factor for the microchannel regenerator is shown in figure (10.1). The top figure

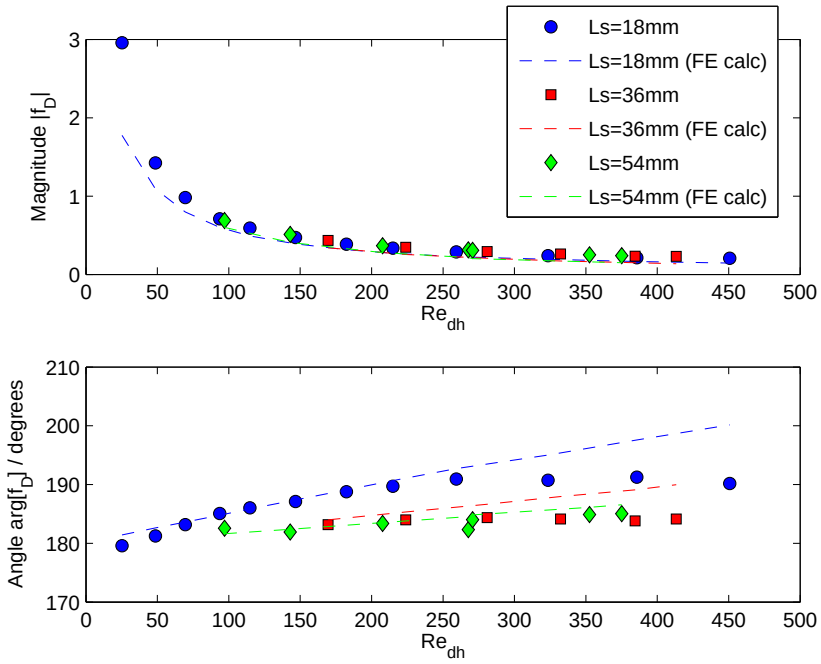

Figure 10.1: Microchannel friction factor

shows the magnitude of the friction factor and the bottom figure the phase an-

gle with respect to piston motion. In general, the 2D FE calculation overestimates the pressure drop and phase angle of the microchannel regenerator. However, the FE calculation captures the general trend with an acceptable error with respect to experimental data.

The friction factor of the spheres geometry at $T = 20^{o}$C is shown in figure (10.2). The experimental data is compared against the Ergun correlation [32] who tested

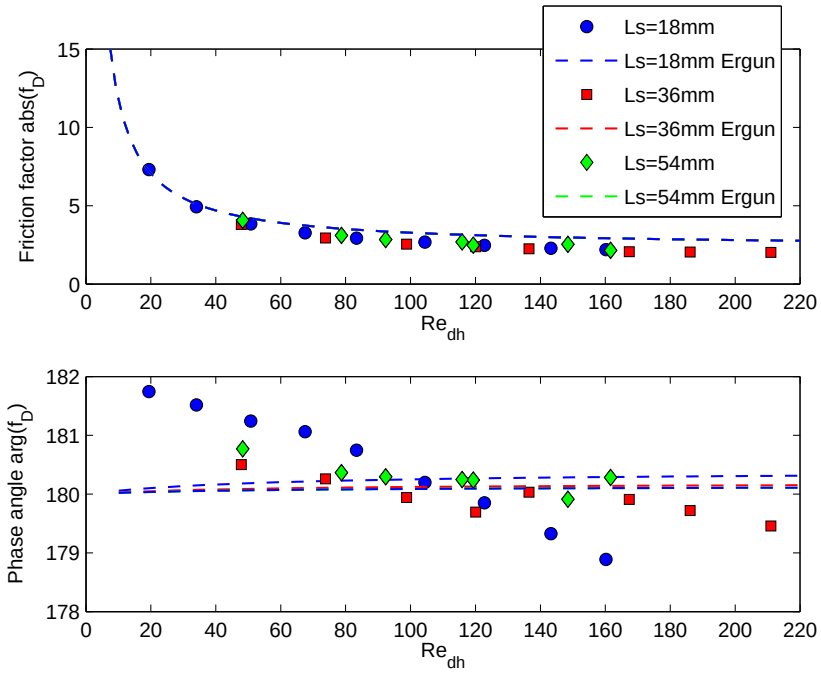

Figure 10.2: Friction factor of sphere geometry

packed beds over a wide range of Reynolds numbers. Ergun proposed $c_1 = 133.3$ and $c_2 = 2.3$ in (3.58). However, the term $-i/A_0$ has not been proposed by Ergun. It must be noted that the RMS value of the Ergun correlation is shown in figure (10.2) because Ergun tested spheres only in steady flow experiments. The Ergun correlation matches the experimental data well in the low Reynolds number regime. At higher Reynolds numbers the Ergun correlation over estimates the experimental data. The small hydraulic diameter has only small effects on the phase angle of the friction factor. However, the measured data shows a small decreasing trend of the phase angle. As mentioned in the previous chapters an increasing trend of the phase angle is expected that accounts for inertial losses. This and the influence of a non-isothermal condition on the friction factor must be further investigated.

The friction factor for the heat exchanger is shown in figure (10.3). The experimental results are compared to the friction factor obtained from the analytical solution of oscillating flow in a circular tube (i.e. one tube in the HEX).

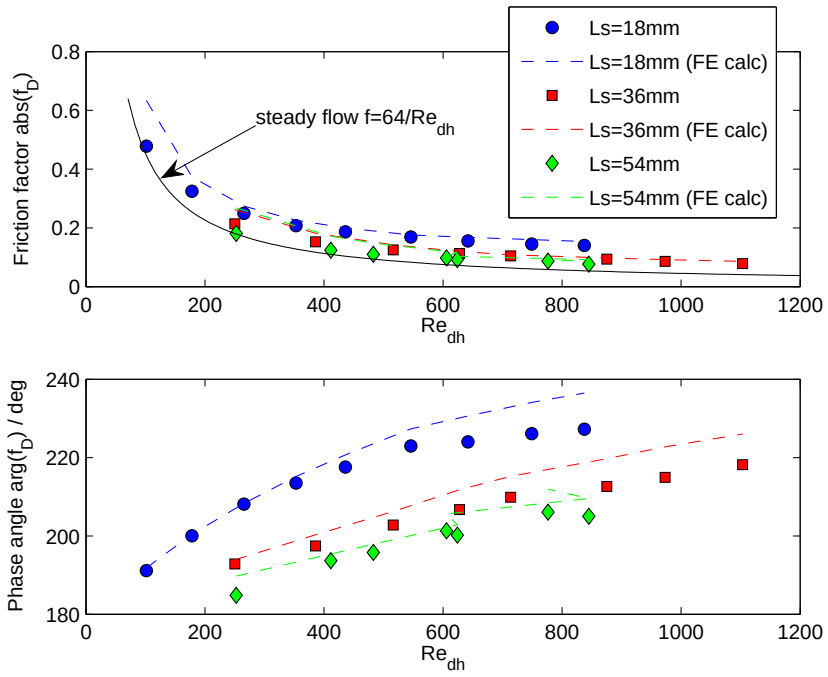

Figure 10.3: Friction factor of the heat exchanger

In general the pressure drop is underestimated at low Reynolds numbers but matches the calculation at higher Reynolds numbers. Conversely the phase angles are reproduced with higher accuracy at low Reynolds numbers than at higher Reynolds numbers. Additionally, the friction factor for steady flow in a pipe $f_D = 64/\mathrm{Re}_{dh}$ is shown and represents the smallest friction factor because it does not include any inertial pressure losses.

It must be noted that the pressure signals are very noisy especially when components with small pressure drops are measured. Still, the friction factors agree with the experimental data within an acceptable limit. However, the goal of this section is not to find a perfect model that accurately reproduces the experimental data. The models are used to check whether the experimental data is sufficiently close to widely used correlations and models based on first principles and indicates that the test apparatus qualitatively operates as expected.

10.2 Nusselt Number

The Nusselt number for both geometries is calculated by evaluating (4.22). The Nusselt number for the microchannel geometry is shown in figure (10.4). The ex-

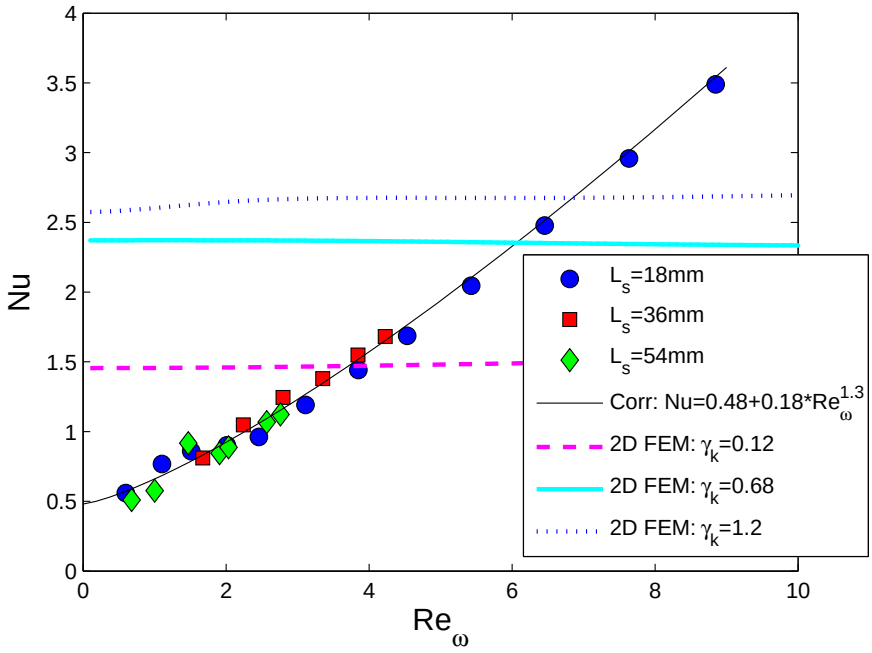

Figure 10.4: Experimentally and theoretically obtained Nusselt numbers for microchannel geometry

perimentally obtained Nusselt numbers show an increasing trend with frequency. The 2D finite element calculation is shown for different thermal diffusivity ratios γ_k. The case with $\gamma_k = 0.12$ approximates the experimental data on an average basis. However, the Nusselt number obtained form the 2D FEM model does not show the same sensitivity as the experimental data. The reason for this is mainly that the microscopic model resolves the radial direction only where the macroscopic model is formulated by retaining axial dependencies only and neglecting diffusion completely. However, the differences between theoretical Nusselt number and experimental Nusselt number are smaller than one order of magnitude. This gives a certain level of confidence in the experimentally obtained Nusselt numbers.

The Nusselt number for the spheres geometry is shown in figure (10.5) It can be seen that the Nusselt number increases faster with frequency than the Nusselt number of the microchannels does. However, large scattering of the data is observ-

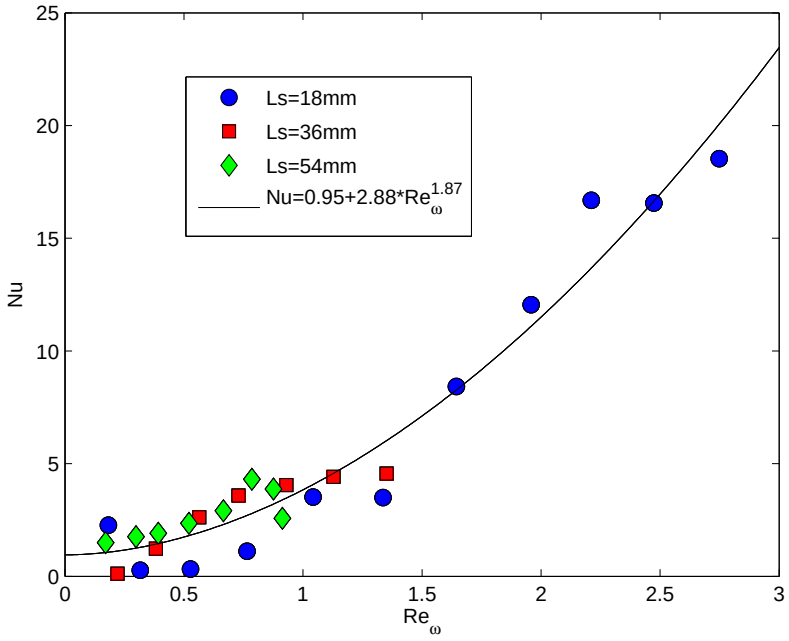

Figure 10.5: Experimentally and theoretically obtained Nusselt numbers for sphere geometry

able in the low frequency limit where the data density is high. It is well known that the Nusselt number scatters in the low frequency limit because other effects than advection are pronounced that are not modelled.

Recently, Engelbrecht [10] proposed a correlation function for the Nusselt number of a packed bed. The correlation results from a single blow type experiment using water as working fluid. However, the size of the test section is very similar to the experimental setup presented in this work. The correlation is given by

$$\mathrm{Nu} = 0.7\mathrm{Pr}^{0.23}\mathrm{Re}^{0.6} \tag{10.1}$$

where the Reynolds number is based on hydraulic diameter and the superficial velocity, i.e. $\mathrm{Re} = \epsilon \cdot \mathrm{Re}_{dh}$.

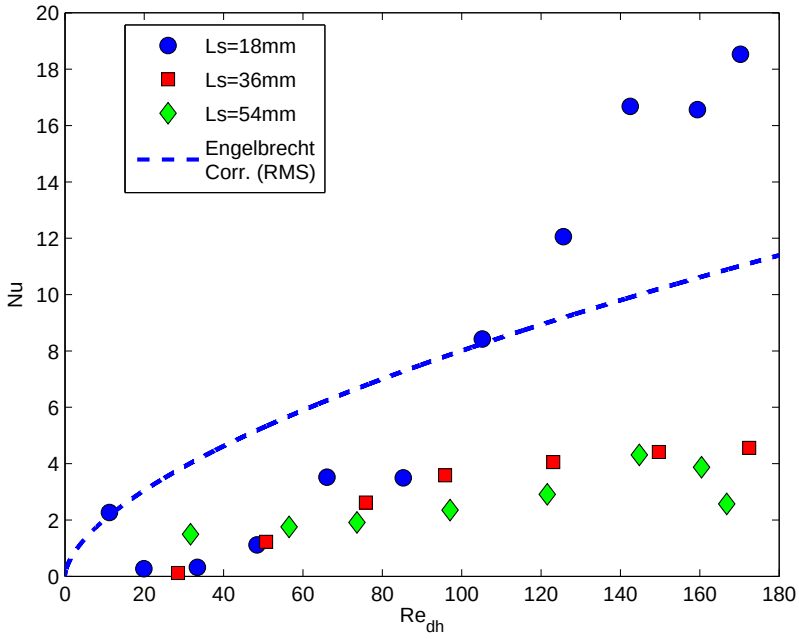

Figure 10.6: Experimental Nusselt numbers versus Engelbrechts correlation for spheres

Figure (10.6) shows Engelbrechts correlation and the experimentally obtained Nusselt numbers as a function of Re_{dh}. The Nusselt numbers obtained at high strokes are lower than predicted by Engelbrechts correlation. At low stroke and high frequency the experimentally obtained Nusselt numbers are higher than predicted by Englebrechts correlation. Since Engelbrechts correlation corresponds to a single blow type experiment, only the RMS value is shown in figure (10.6). More data needs to be taken in the low frequency range and processed with extended models to understand low to medium frequency behavior. It must be noted that the tests include low frequency data sets that are rather not relevant for the operation of a regenerator in an actual device. Finally the Nusselt numbers of the two geometries are shown in figure (10.7). It can be seen that over the entire frequency range the sphere geometry shows generally a higher Nusselt number than the microchannel geometry. This can be expected due to the large specific surface area of the particle bed geometry.

The Nusselt number is usually parametrized using a generic form given by

$$\mathrm{Nu} = \alpha + \beta \mathrm{Re}_{\omega}^{\gamma} \tag{10.2}$$

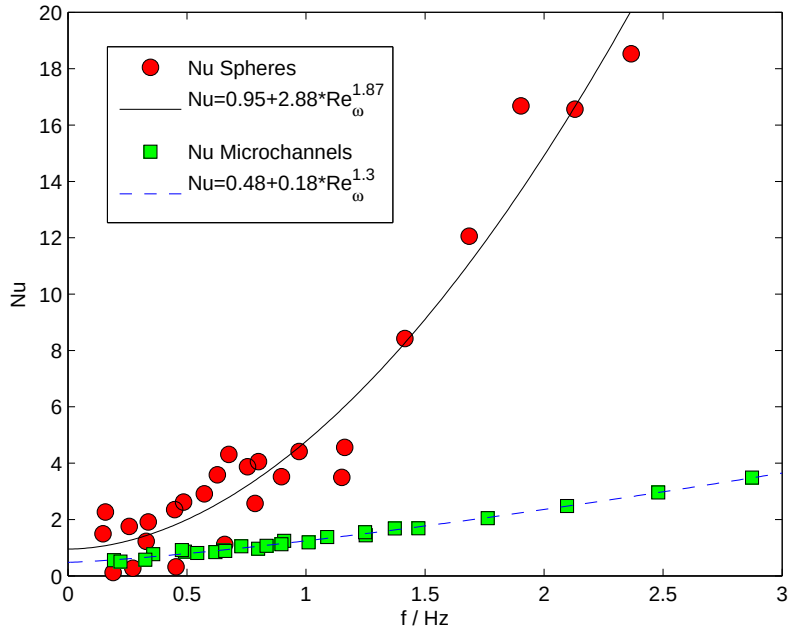

Figure 10.7: Comparions of Nusselt numbers of the two geometries

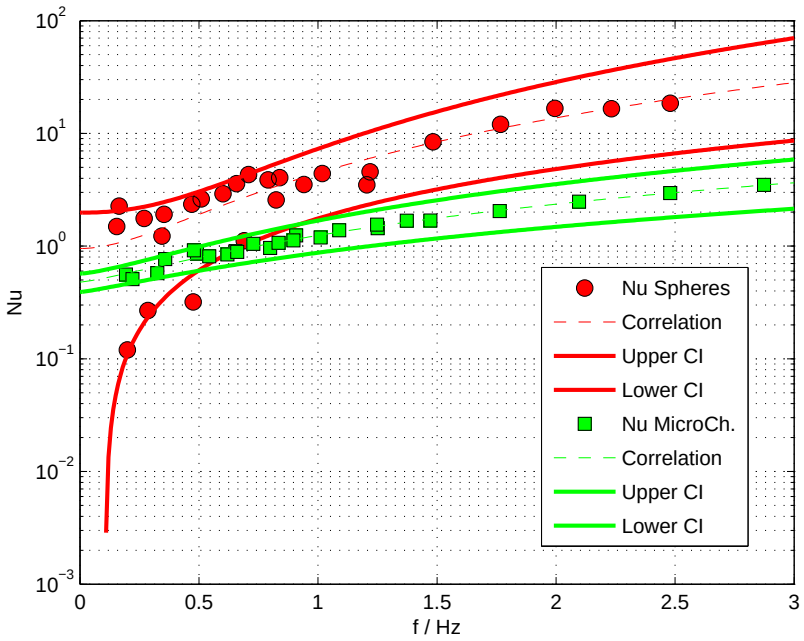

Figure 10.8: Nusselt number with 95% confidence bounds

The parameters are estimated using a least square routine as summarized in table (10.1) It can be seen that the confidence intervals are large for the sphere

Table 10.1: Parameters for Nusselt number correlation with 95% confidence intervall

Geometry	$\alpha \pm$ CI	$\beta \pm$ CI	$\gamma \pm$ CI
Microchannel	0.48 ± 0.090	0.18 ± 0.05	1.3 ± 0.12
Spheres	0.95 ± 1.03	2.88 ± 1.30	1.87 ± 0.45

geometry. However, this confidence interval does not directly reflect scatter at low frequency that results from the very simple model used to calculate the Nusselt numbers. However, there is a high statistical uncertainty in the high frequency limit because there is less data points than in the low frequency limit as indicated in figure (10.8). The confidence bounds of the sphere correlation function are larger than the bounds for the microchannels. The reason for this lies in the small degree of scatter of the microchannel Nusselt numbers. More data and extended models must be used to minimize this uncertainty.

Chapter 11

Summary and Key Findings for Part II - Experimental

The work reported in part II of this thesis describes an experimental apparatus and method to generate data that serves as a basis to extract friction factor and Nusselt number. The apparatus comprises two heat exchangers a regenerator and a fluid displacer. Frequency, stroke and temperature span can be controlled by the experimentalist. The data is processed using DFT.

The temperature readings are corrected in order to remove phase lags due to inertial pressure losses from the temperature data. The increasing phase angle with frequency with a non zero temperature gradient stands in contradiction with model predictions. The model predicts a decreasing phase angle with frequency.

Over a range of experimental conditions, the friction factors agree well with model predictions. Both magnitude and phase angle of the friction factor are well approximated by model predictions.

The Nusselt number for the sphere regenerator shows strong sensitivity to frequency. In the low frequency limit the Nusselt numbers underestimate Engelbrechts correlation for steady flow conditions. The Nusselt numbers for the microchannel regenerator are lower and show less sensitivity with respect to frequency. The 2D model predictions for the microchannel regenerator approximate the Nusselt number in an average sense but do not show any sensitivity to frequency.

Chapter 12

Conclusions and Recommendations

12.1 Conclusion

This thesis focuses on the thermohydraulic properties of oscillating flow in porous media. A theoretical method is presented to extract friction factor and Nusselt number. Results are compared to virtual experiments using a 2D validation procedure. A test apparatus is presented to test various regenerator geometries. The goal of this research is to develop a clear theoretical and experimental procedure that determines friction factor and Nusselt number for various types of regenerators.

In the first part of this thesis, models for momentum and energy conservation are presented that hold on a macroscopic and a microscopic scale using an harmonic approximation technique. A two dimensional numerical model is presented based on a microchannel geometry that allows for a purely theoretical calculation of the friction factor and Nusselt number. This model is used to determine the functional sensitivity of the Nusselt number and to validate the macroscopic models. It is shown that the Nusselt number is sensitive to operating frequency, thermal mass ratio and thermal conductivity ratio. As a result the macroscopic model only agrees with the microscopic model at operating contritions and material properties where diffusion effects are small.

In the second part of this thesis an experimental device is described and raw experimental data is presented. A phase referencing method is discussed that accounts for inertial pressure drops outside of the test section in order to apply the macroscopic expression for the Nusselt number derived in part I of this thesis.

The friction factors obtained from experiments show fair agreement with model predictions. The Nusselt number for the spheres geometry is compared against a correlation obtained from a steady flow experiment and shows a discrepancy at low frequency. The Nusselt numbers for the microchannel geometry are compared against the 2D model presented in part I. Under a thermal conductivity ratio smaller than unity the 2D model can approximate the experimentally obtained Nusselt number on a frequency averaged basis. It can be seen that the spheres regenerator show larger pressure drop and Nusselt number than the microchannel regenerator.

12.2 Recommendations and Future Work

There are a number of areas for future investigation relating to the theory and experimental methods. These are listed in the follow sections.

12.2.1 Part I - Model Development and Validation

Macroscopic Modeling

There are various options to extend the macroscopic models. However, the model extension make only sense if they can be validated experimentally or using the microscopic model. The assumption of a constant time averaged temperature gradient should be validated and if necessary extended as a first option because it will influence model prediction for first order temperature. The model to first order will structurally change if the temperature gradient will become a local quantity. This is the case when the effective thermal conductivity of the solid phase becomes small.

The inclusion of diffusion terms to first order can be of theoretical use in order to validate the influence of solid thermal conductivity on the Nusselt number.

Microscopic Modeling

Further analysis on the sensitivity of Nusselt number to geometrical aspects such as sensitivity to porosity and geometrical variations is recommended.

Geometries that cannot easily represented in 2D computational domains (e.g. spheres) should first be studied using the 2D implementation of this model. The

extension to 3D is desirable in order resolve a REV in the axial direction. However, a 3D extension is numerically and physically delicate. For 3D eddy current calculations, the assembled linear system becomes singular and must be solved using iterative solvers [27]. In addition, the boundary conditions imposed on the 3D model must be consistent with the macroscopic model for validation purposes which requires further modeling effort [33].

12.2.2 Part II - Experimental

1. Hydraulic characterization of pressure drop in the piping:
   This is an important aspect of this work because it greatly affects the magnitude of the Nusselt number. Therefore, it is vital that the pressure loss (magnitude and phase) in the piping is characterized accurately. This must be done experimentally and compared to model predictions (circular tube model in appendix (B)).

2. Spheres pressure drop:
   The pressure drop for the spheres regenerator needs to be studied separately under different isothermal temperatures to better quantify under which situations the pressure drop agrees with model predictions.

3. Time averaged temperature gradient and higher order contributions:
   The validity of a constant time averaged temperature gradient (as assumed in part I) needs to be confirmed. This can be done for the spheres regenerator, but most likely not with the microchannel regenerator. Physical limits should be identified that lead to higher order temperature contributions. Whether higher order effects contribute to the Nusselt number is not clear at this point.

4. Uncertainty analysis:
   The uncertainty in temperature reading causes large uncertainty for the experimentally obtained Nusselt number if the temperature span is too small. The temperature span can not be controlled directly. A poor regenerator will not show the same temperature span because it stores less thermal energy in a blow period. Thus, it is recommended to study regenerators with a large surface area to ensure large temperature spans and eliminate the aspect of uncertainty at this stage of research. If regenerators are tested that show small temperature spans the Nusselt number should be evaluated over each

cycle for a given experiment (fixed frequency and stroke). This will allow to come up with a probability distribution for the Nusselt number that can be used to establish confidence intervals.

5. Experimental evaluation of time averaged energy flux:
   The time averaged energy flux can be estimated using temperature readings at the heat exchangers. Instead of just matching real parts of temperatures, the model predictions can be compared to the time averaged energy flux using the Nusselt number as degree of freedom. This will also help to estimate ambient losses if the time averaged energy flux is calculated on both heat exchangers.

6. Benchmarking:
   The knowledge of friction factor and Nusselt number by itself does not allow to draw general conclusions about the performance of a regenerator. Since the pressure drop and the interfacial heat transfer are both irreversible processes that counteract each other, it is recommended to benchmark regenerators in terms energy dissipation by unit regenerator volume. This will help to identify optimized regenerator geometries.

Bibliography

[1] R.K. SHAH, D.P. SEKULIC, *Fundamentals of Heat Exchanger Design*, John Wiley & Sons, 2003.

[2] A. TURA, A. ROWE, *Progress in the Characterization and Optimization of a Permanent Magnet Magnetic Refrigerator*, Proc. International Conference of Magnetic Refrigeration at Room Temperature 2009 (Des Moines, IW USA), IIF/IIR.

[3] J.A. BARCLAY, *Active and passive magnetic regenerators in gas/magnetic refrigerators*, Journal of Alloys and Compounds, 207/208 (1994) 355-361.

[4] F.W SCHMIDT, A.J. WILMOTT, *Thermal energy storage and regeneration*, Hemisphere Washington DC, 1981.

[5] W.M. KAYS, A.L. LONDON , *Compact Heat Exchangers*, Krieger Pub. Co., 3rd Sub-Eddition 2003.

[6] N. WAKAO, S. KAGUEI, *Heat and Mass Transfer in Packed beds*, Gordon and Breach Science Publishers, 1982.

[7] E. ACHENBACH, *Heat and Flow Characteristics of Packed beds*, Experimental Thermal and Fluid Science Vol.10-Nr.1, 1995.

[8] C.T. HSU, *Dynamic modeling of convective heat transfer in porous media*, Handbook of porous media, CRC Press 2005.

[9] H. HAUSEN, *Berechnung der Waermeuebertragung in Regeneratoren bei temperaturabhaengigen Stoffwerten und Waermeuebergangszahlen*, International Journal of Heat and Mass Transfer, Vol.7, 1964.

[10] H. K. ENGELBRECHT, *A Numerical Model of an Active Magnetic Refrigerator with Experimental Validation*, PhD Report University of Wisconsin, Madison, 2008.

[11] MACIAS-MACHIN, A., OUFER, L. N. WANNENMACHER, *Heat Transfer between an Immersed Wire and a Liquid Fluidized Bed*, Powder Technology 66:281-284, 1991.

[12] A. SARLAH, A.POREDOS, *Dimensionless Numerical Model for Simulation of Active Magnetic Regenerator Refrigerator*, International Journal of Refrigeration , 2010, doi:10.1016/j.ijrefrig.2010.04.003.

[13] W.M KAYS, A.L. LONDON, *Compact Heat Exchangers 2nd ed.*, McGraw-Hill USA, 1964.

[14] G.T. LEE, B.H. KANG, J.H. LEE, *Effectiveness Enhancement of a Thermal Regenerator in Oscillating Flow*, Applied Thermal Engineering Vol. 18 No.8, 1997.

[15] D.E. DANEY, *Regenerator Performance with Sinusoidal Flow*, Cryogenics, Vol. 3, 1991.

[16] Y. CHEN, E. LUO, W. DAI, *Heat Transfer Characteristics of Oscillating Flow Regenerator Filled with Circular Tubes or Parallel Plates*, Cryogenics, Vol. 47, 2007.

[17] T.W. SIMON J.R. SEUME, *A Survey of Oscillating Flow in Stirling Heat Exchangers*, NASA Contractor Report 182108, 1988.

[18] T. ZHAO, P. CHENG, *Oscillatory Heat Transfer in a Pipe Subjected to a Laminar Reciprocating Flow*, ASME Journal of Heat Transfer, Vol. 118, 1996.

[19] M. ROOS, E. BATAWI, U. HARNISCH, TH. HOCKER, *Efficient simulation of fuel cell stacks with the volume averaging method*, Journal of Power Sources, Vol. 118, 2003.

[20] M. KAVIANY, *Principles of Heat Transfer in Porous Media*, Springer 1995.

[21] S. ERGUN, *Fluid Flow through packed Columns* , Chem. Eng. Prog., 48:89-94, 1952.

[22] H.U. FUCHS, *The Dynamics of Heat*, Springer 1996.

[23] G.W. SWIFT, W.C. WARD, *Simple Harmonic Approximation of Regenerators*, Journal of Thermophysics and Heat Transfer; Vol.10 No. 4, Oct-Dec 1996.

[24] A.T.A.M DE WAELE, H.W.G. HOOIJKAAS,P.P STEIJAERT AND A.A.J. BENSCHOP, *Regenerator Dynamics in the Harmonic Approximation*, Cryogenics; Vol.38 No. 10, 1998.

[25] P. NIKA, Y. BAILLY, F. GUERMEUR, *Thermoacoustics and related oscillatory heat and fluid flows in micro heat exchangers*, International Journal of Heat and Mass Transfer 48 (2005) 37773-3792.

[26] F. INCROPERA ET. AL., *Fundamentals of Heat and Mass Transfer*, John Wiley and Sons, 2003.

[27] G.SARTORIS, ET AL, *NM Seses, Multiphysics Software Tutorial*, NM Numerical Modeling GmbH, Thalwil, Switzerland.

[28] H. OERTEL JR., *Prandtl-Fhrer durch die Strmungslehre*, Vieweg 2002.

[29] J.R. WOMERSLEY, *Method for the Calculation of Velocity, Rate of Flow and viscous Drag in Arteries when the Pressure Gradient is known*, Journal of Physiol. 127, 553-563 (1955).

[30] OMEGA ENGINEERING ,http://www.omega.co.uk/temperature/pdf/Thermocouple_Tolerance.pdf.

[31] L. PAPULA, *Mathematik fuer Ingenieure und Naturwissenschaftler Band 3*, Vieweg 2001.

[32] D.A. NIELD, A. BEJAN, *Convection in porous media*, Springer-Verlag 1992.

[33] A. NAKAYAMA AND F. KUWAHARA, *Numerical Modeling of Convective Heat Transfer in Porous Media Using Microscopic Structures*, Handbook of porous media, CRC Press 2005.

Appendix A

Macroscopic Balance Equation

A.1 Microscopic Balance Equations

We make the important assumption that mass-, momentum- and thermal energy balance hold exactly on the microscopic scale (pore scale). Using standard material laws (i.e. Newtonian fluid, Fourier heat flux) these balance equations read

$$\nabla \cdot \boldsymbol{v} = 0 \tag{A.1}$$

$$\rho \frac{D\boldsymbol{v}}{Dt} = -\nabla p + \mu \nabla^2 \boldsymbol{v} \tag{A.2}$$

$$\rho c_p \frac{DT}{Dt} = \kappa \nabla^2 T \tag{A.3}$$

In general these equations hold on Ω_r. However, on Ω_s the velocity is equal to zero $\boldsymbol{v} = \boldsymbol{0}$. These equations assume incompressible flow and negligible viscous dissipation in the thermal energy balance. However, the latter assumption might be invalid due to high velocity gradients close to the solid wall but will keep the governing equations as simple as possible.

A.2 Macroscopic Balance Equations

The macroscopic balance equations are averaged by applying equation (3.7) to (A.1), (A.2) and (A.3). This has been discussed by many researchers and evolved as a standard technique to obtain macroscopic balance equations. In fact any extensive quantity ψ is expressed as superposition of its mean value $\langle \psi \rangle$ and a deviation

about the mean ψ' within Γ

$$\psi = \langle\psi\rangle + \psi' \tag{A.4}$$

As a consequence, one faces a closure problem for ψ' in order to obtain meaningful macroscopic balance equations applicable to experiments. Hsu [8] presents in his review a set of macroscopic balance equations to describe superficial flow and heat transfer in porous media. The macroscopic transport equation for momentum reads

$$\rho\left[\frac{\partial \boldsymbol{v}_s}{\partial t} + \nabla\cdot\frac{1}{\epsilon}\boldsymbol{v}_s\boldsymbol{v}_s\right] = -\nabla\left(\epsilon\langle p\rangle^f\right) + \mu\nabla^2\boldsymbol{v}_s + \boldsymbol{b}_{\text{fs}} \tag{A.5}$$

The additional term (resulting from closure modeling) is called the volumetric interfacial force as exerted by the solids (pressure and shear stress acting on the solid surface). The interfacial force is a complex expression [8], the linear and quadratic terms are

$$\frac{\boldsymbol{b}_{\text{sf}}}{\epsilon} = -\frac{\mu\boldsymbol{v}_s}{K} - F\rho\frac{|\boldsymbol{v}_s|\boldsymbol{v}_s}{\sqrt{K}} \tag{A.6}$$

where K and F are the hydraulic permeability and F the Forchheimer factor, respectively.

The microscopic energy balance must be averaged twice (for fluid and solid domain), hence two coupled balance equations are obtained

$$\begin{aligned}(\rho c)_f\frac{\partial\epsilon\langle T\rangle^f}{\partial t} + (\rho c)_f\boldsymbol{v}_s\nabla\langle T\rangle^f &= \kappa_f\nabla^2\left(\epsilon\langle T\rangle^f\right) \\ &\quad + (\rho c)_f\nabla\cdot\left(\boldsymbol{A}_D\cdot\nabla\langle T\rangle^f\right) \\ &\quad + \kappa_f\nabla\cdot\left[G\left(\nabla\langle T\rangle^f - \frac{\kappa_s}{\kappa_f}\nabla\langle T\rangle^s\right)\right] \\ &\quad + ha_{\text{sf}}\left(\langle T\rangle^s - \langle T\rangle^f\right)\end{aligned} \tag{A.7}$$

$$\begin{aligned}(\rho c)_s\frac{\partial\epsilon_s\langle T\rangle^s}{\partial t} &= \kappa_s\nabla^2\left(\epsilon_s\langle T\rangle^s\right) \\ &\quad - \kappa_s\nabla\cdot\left[G\left(\nabla\langle T\rangle^f - \frac{\kappa_s}{\kappa_f}\nabla\langle T\rangle^s\right)\right] \\ &\quad - ha_{\text{sf}}\left(\langle T\rangle^s - \langle T\rangle^f\right)\end{aligned} \tag{A.8}$$

with G the thermal turtuosity coefficient, $\epsilon_s = 1-\epsilon$, $\boldsymbol{A}_D$ the dispersion tensor, and h the interfacial heat transfer coefficient. All these coefficients arise from closure modeling, and their associated transport process holds only on the device length

scale (macroscopic length scale). The above coefficients must be determined experimentally.

Appendix B

Oscillating Flow and Heat Transfer in Circular Tube

In this section the governing microscopic balance equations of form (5.14) are solved on a circular tube geometry. Analytical solutions and correlations available in literature are compared to numerically calculated solutions and correlations.

A circular tube regenerator is first considered because it provides analytical solutions for the flow field in an oscillatory flow environment and will give us a chance to validate the results provided by FE simulator NM Seses. However, the temperature field must be calculated numerically for $\mathrm{Pr} \neq 1$. The numerical result for the Nusselt number can be compared with Chen et al [16] who calculated the Nusselt number in oscillatory flow for $\mathrm{Re}_\omega \leq 10$ by semi-analytical methods.
We consider a tube with diameter equal to the hydraulic diameter d_h. Equation (5.14) in cylindrical coordinates balance for momentum and thermal energy becomes Bessel's equation

$$\frac{\mathrm{d}^2\psi}{\mathrm{d}\hat{r}^2} + \frac{1}{\hat{r}}\frac{\mathrm{d}\psi}{\mathrm{d}\hat{r}} - iM\psi = K \tag{B.1}$$

$$\psi(\hat{r} = 1/2) = 0 \tag{B.2}$$

$$\mathrm{d}\psi(\hat{r} = 0)/\mathrm{d}\hat{r} = 0 \tag{B.3}$$

The solution to this equation is a linear combination of Bessel functions of first and second kind to order zero and a particular solution proportional to excitation K

$$\psi = C_1 J_0(\alpha\hat{r}) + C_2 Y_0(\alpha\hat{r}) + i\frac{K}{M}$$

where J_0 and Y_0 are Bessel functions of first and second kind, respectively. The coefficients are due to the boundary conditions $C_1 = -iK/M \cdot J_0(\alpha/2)$ and $C_2 = 0$. The final solution is thus

$$\psi = i\frac{K}{M}\left(1 - \frac{J_0(\alpha\hat{r})}{J_0(\alpha/2)}\right) \tag{B.4}$$

The eigenvalue is given by $\alpha = i^{3/2}\sqrt{M}$. For the momentum balance the solution can be written as

$$\hat{v}_{z1}(\hat{r}) = iA_0\frac{\mathrm{d}\hat{p}}{\mathrm{d}\zeta}\left(1 - \frac{J_0\left(i^{3/2}\sqrt{\mathrm{Re}_\omega}\hat{r}\right)}{J_0\left(i^{3/2}\sqrt{\mathrm{Re}_\omega}/2\right)}\right) \tag{B.5}$$

The eigenvalue is proportional to the Womersley number $\mathrm{Wo} = \sqrt{\mathrm{Re}_\omega}$ who himself proposed the above solution [29] for the oscillating flow in arteries. He also pointed out the similarity with charge transport in electrical conductors.
The solution to the thermal energy balance is not as straight forward as for the momentum balance since $K = K(\hat{r})$ and $\mathrm{Pr} \neq 1$. For this reason, the entire problem has been calculated numerically with FE solver NM Seses. To appreciate the complexity of the solution the velocity and temperature profile is shown in figure (B.1).

The first row in figure (B.1) shows the pressure gradient $\mathrm{d}\hat{p}/\mathrm{d}\zeta = -1$ and can thus be represented as a negative cosine. The pressure gradient is assumed to be constant in radial direction. The second row shows velocity profiles at different phase angels. At $\omega t = 0$ we observe highest velocity, also at phase angle $\omega t = 45^{\mathrm{o}}$. Even at $\omega t = 90^{\mathrm{o}}$, where the pressure gradient is zero, we can still observe a net flow significantly different from zero. This is evidence for the existence of a phase lag between pressure gradient and velocity due to transient inertial forces as the the frequency increases [8].
As expected, the temperature will lag the velocity since a finite time is needed to advectiveley transport the thermal energy to any axial location. For the configuration shown in figure (B.1) the phase lag between velocity and temperature is approximately 45^{o}.
As a final step, the Nusselt number can be calculated by applying equation (5.13). Since the temperature gradient is the same at all positions, equation (5.13) can be simplified to

$$\mathrm{Nu} = -\frac{1}{\langle\theta\rangle}\frac{\mathrm{d}\theta}{\mathrm{d}\hat{r}}\bigg|_{\hat{r}=0.5} \tag{B.6}$$

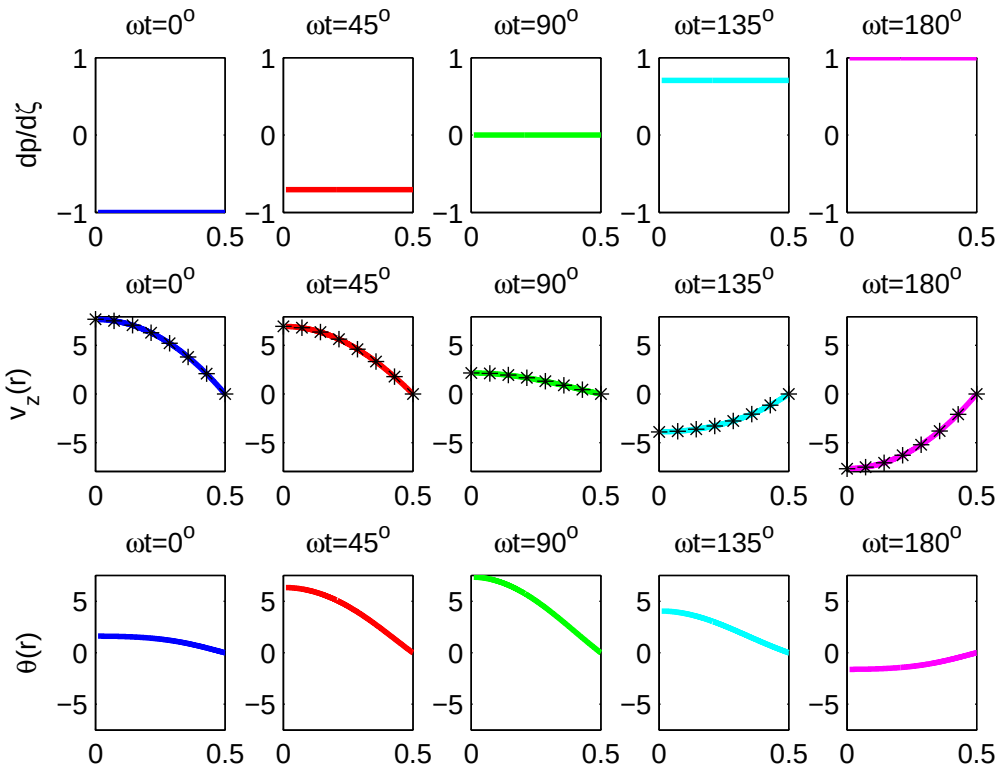

Figure B.1: Velocity and temperature profile in cylindrical tube subjected to oscillating flow $\mathrm{Re}_\omega = 6$, $A_0 = 22$, $\mathrm{Pr} = 7$, $\mathrm{d}\hat{p}/\mathrm{d}\zeta = -1$. The black stars indicate the analytical solutions (B.5) and the solid lines are numerical calculations by NM Seses

The Nusselt number predictions produced by FE simulator are shown in figure (B.2). Chen et al. [16] calculated the Nusselt number using semi analytical methods for compressible and incompressible flow. The incompressible part of the Nusselt number for $\mathrm{Re}_\omega \leq 10$ is

$$\mathrm{Nu} = 6 + \frac{i}{128}\left(\mathrm{Pr}+1\right)\mathrm{Re}_\omega \qquad \text{for } \mathrm{Re}_\omega \leq 10 \tag{B.7}$$

A fair agreement between the prediction of Chen et al. and the present work can be observed in figure (B.2). The real part of Nu is slightly larger than the reference correlation. It must be pointed out that gradients are difficult to post process from FE solutions, such that the reason for the small deviation might be due to numerical imperfection. On the other hand, the imaginary part of Nu agrees well with the

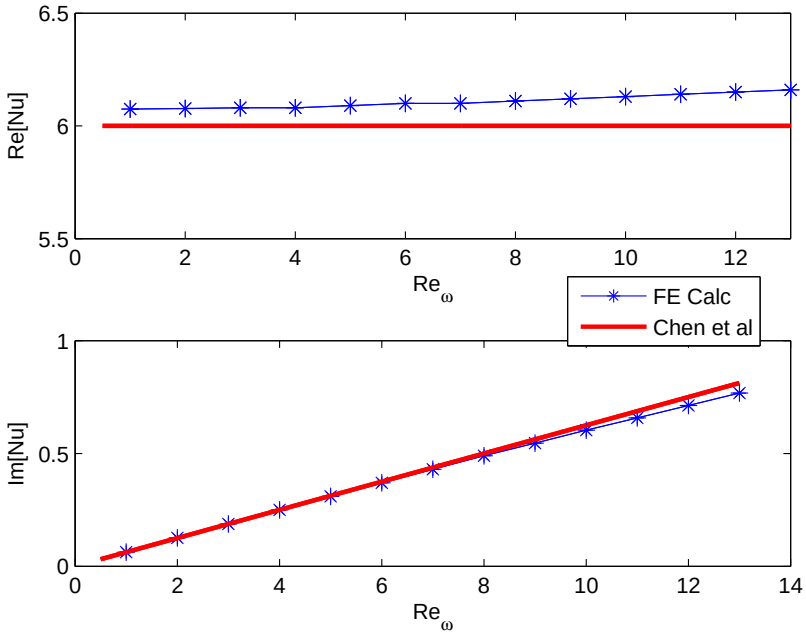

Figure B.2: Nusselt number predictions for circular tube geometry compared to predictions made by Chen et al. [16]

reference correlation.

In this section we have validated the 2D FE simulation for a circular tube with the correlation provided by Chen et al. Having showed that this method provides acceptable results for Nu we can apply the same procedure to other channel like geometries such as the square channel geometry which has been tested experimentally.

Appendix C

Derivation of Temperature Limits

In this appendix, temperature limits are derived based on (4.8).

- Limits for imaginary part of temperature
  The real part of the temperature vanishes in the non isothermal limit and in the isothermal limit. The temperature oscillations for $\mathrm{Re}_\omega \to 0$ is given by (4.27). For the empty pipe solution (or $\mathrm{Re}_\omega \to \infty$ and finite Nu) the temperature oscillations are maximal. Mathematically this is given by

$$\theta_{f1} \in \left[-i, -i\frac{R}{R+1}\right] \tag{C.1}$$

  or

$$\mathrm{Im}\left[\theta_{f1}\right] \in \left[-1, -\frac{R}{R+1}\right] \tag{C.2}$$

- Limits for real part of temperature
  The maximum possible are expected whenever $\mathrm{Im}\left[\mathrm{Nu}\right] = 0$. This can be graphically observed in figures (4.5) and (4.6). The Nusselt number (4.8) separated into real and imaginary part is

$$\mathrm{Re}\left[\mathrm{Nu}\right] = \frac{\mathrm{PrRe}_\omega}{4} \frac{\mathrm{Re}\left[\theta_{f1}\right]}{\left(R + \mathrm{Im}\left[\theta_{f1}\right] + R\mathrm{Im}\left[\theta_{f1}\right]\right)^2 + \left((1+R)\mathrm{Re}\left[\theta_{f1}\right]\right)^2} \tag{C.3}$$

$$\mathrm{Im}\left[\mathrm{Nu}\right] = -\frac{\mathrm{PrRe}_\omega}{4} \cdot \frac{(1+R)\,\mathrm{Re}\left[\theta_{f1}\right] + \left(1 + \mathrm{Im}\left[\theta_{f1}\right]\right)\left(R + \mathrm{Im}\left[\theta_{f1}\right] + R\mathrm{Im}\left[\theta_{f1}\right]\right)}{\left(R + \mathrm{Im}\left[\theta_{f1}\right] + R\mathrm{Im}\left[\theta_{f1}\right]\right)^2 + \left((1+R)\mathrm{Re}\left[\theta_{f1}\right]\right)^2} \tag{C.4}$$

Setting $\mathrm{Im}\left[\mathrm{Nu}\right] = 0$ in equation (C.5) and solving for $\mathrm{Re}\left[\theta_{f1}\right]$ gives

$$\mathrm{Re}\left[\theta_{f1}\right] = \pm\sqrt{-\frac{1+\mathrm{Im}\left[\theta_{f1}\right]}{1+R}\left(R+\mathrm{Im}\left[\theta_{f1}\right]+R\mathrm{Im}\left[\theta_{f1}\right]\right)} \tag{C.5}$$

Equation (C.5) represents the value of the real part of temperature if $\mathrm{Im}\left[\mathrm{Nu}\right] = 0$, i.e. where the Nusselt number is real but has arbitrary magnitude. For the case $R \to 0$ the case discussed in equation (4.31) is recovered. The maximum possible real part of temperature is obtained by setting the derivative of the real part of temperature with respect to the imaginary part of temperature to zero. The calculation simplifies by noting that the expression under the root is equal to its derivative with respect to the imaginary part of temperature

$$\frac{\mathrm{d}(\mathrm{Re}\left[\theta_{f1}\right])^2}{\mathrm{dIm}\left[\theta_{f1}\right]} = \left(\mathrm{Re}\left[\theta_{f1}\right]\right)^2 \tag{C.6}$$

Setting the derivative of real part of temperature with respect to imaginary part of temperature zero gives

$$0 = \frac{\mathrm{dRe}\left[\theta_{f1}\right]}{\mathrm{dIm}\left[\theta_{f1}\right]} = \frac{1}{2\mathrm{Re}\left[\theta_{f1}\right]}\frac{\mathrm{d}(\mathrm{Re}\left[\theta_{f1}\right])^2}{\mathrm{dIm}\left[\theta_{f1}\right]} = \frac{1}{2}\mathrm{Re}\left[\theta_{f1}\right] \tag{C.7}$$

The real part of the temperature is zero when the expression under the root of (C.5) is zero. Solving for the imaginary part of temperature gives

$$\mathrm{Im}\left[\theta_{f1}\right] = -\frac{1+2R}{2(R+1)} \tag{C.8}$$

This value is equal to the center position of the circle on the imaginary axis

$$-\frac{R}{1+R} - \frac{1}{2}\left(1-\frac{R}{1+R}\right) = -\frac{2R+1}{2(1+R)} \tag{C.9}$$

The maximum possible value of the real part of temperature for the case $\mathrm{Im}\left[\mathrm{Nu}\right] = 0$ is obtained by re evaluating equation (C.5) at (C.8)

$$\mathrm{Re}\left[\theta_{f1}\right] = \frac{1}{2\left(1+R\right)} \tag{C.10}$$